DISSERTATION

MEASUREMENT OF AMMONIA EMISSION FROM AGRICULTURAL SITES USING OPEN-PATH CAVITY RING-DOWN SPECTROSCOPY AND WAVELENGTH MODULATION SPECTROSCOPY BASED ANALYZERS

Submitted by

Soran Shadman

Department of Mechanical Engineering

In Partial Fulfillment of the Requirements

For the Degree of Doctor of Philosophy

Colorado State University

Fort Collins, Colorado

Summer 2018

Doctoral Committee:

Advisor: Azer P. Yalin

Anthony J. Marchese
Daniel B. Olsen
Jay Ham

ABSTRACT

MEASUREMENT OF AMMONIA EMISSION FROM AGRICULTURAL SITES USING OPEN-PATH CAVITY RING-DOWN SPECTROSCOPY AND WAVELENGTH MODULATION SPECTROSCOPY BASED ANALYZERS

Agricultural activities and animal feedlot operations are the primary sources of emitted ammonia into the atmosphere. In the US, 4 Tg of ammonia is emitted every year into the atmosphere which ~%75 of that is due to these major sources. Ammonia is the third most abundant nitrogen containing species in the atmosphere and it has important impacts on atmospheric chemistry, health, and the environment. It is a precursor to the formation of aerosols and its deposition in pristine and aquatic systems leads to changes in ecosystem properties. Quantifying the dry deposition rate of ammonia in the first few kilometers of feedlots is crucial for better understanding the impacts of livestock and agricultural operations on environment. Therefore, fast, precise, and portable sensors are needed to quantify ammonia emission from its major sources. Absorption spectroscopy is a reliable technique by which compact and sensitive sensors can be developed for ammonia (and other gaseous species) detection. An open-path absorption spectroscopy based sensor allows ambient air to flow directly through its measurement region which leads to high-sensitivity and fast-response measurements. In this study, two open-path absorption based ammonia sensors using two techniques are developed: cavity ring-down spectroscopy (CRDS) and wavelength modulation spectroscopy (WMS). The CRDS and WMS based sensors show the sensitivity of ~1.5 ppb (at 1 second) and ~4 ppb (at 1 second), respectively. In both sensors, a quantum cascade laser (QCL) is utilized as the light source to cover the strongest absorption feature

of ammonia in the mid-infrared (MIR) spectral region. It is the first demonstration of an open-path CRDS based sensor working in mid-infrared MIR, to our knowledge. The WMS based sensor developed in this study is low power (~25 W) and relatively lightweight (~4 kg). The low power consumption and compact size enables the sensor to be deployed on a commercialized unmanned aerial system (UAS) for aerial measurements. The combination of this sensor and another compact CRDS based methane sensor is used for simultaneous measurements of ammonia and methane (ground based and aerial). Methane is another important species emitted from the feedlots with a long lifetime (~10 years). It is nonreactive and thus not lost by dry deposition. Therefore, methane concentration is only influenced by dispersion while the ammonia concentration is affected by both deposition and dispersion. The dry deposition of ammonia nearby the concentrated animal feeding operations (CAFOs), as one of the major sources of ammonia, can be determined by measuring the decrease in the $[NH_3]/[CH_4]$ ratio downwind.

ACKNOWLEDGMENTS

It is my great pleasure to thank who have supported me to make this study possible.

First, I owe my deepest gratitude to my advisor Professor Azer Yalin for his mentoring, continuous support, and valuable guidance. His guidance helped me in all the time of research and writing the thesis. I very appreciate him for the opportunity he gave me to be part of his group.

I also want to thank Professor Jay Ham for his cooperation and guidance during the field measurements. Thank the rest of my committee, Professor Anthony Marchese and Professor Daniel Olsen. I am very grateful for their time and valuable feedback to my research.

My colleagues at the Center for Laser Sensing and Diagnostics deserve great thanks for making the lab a great environment to work in: Laurie McHale, Adam Friss, Ciprian Dumitrache, Charles Rose, Sean Walsh, Betsy Farris, and Ben Martinez. I appreciate the valuable support from the former lab members, Dr. Brian Lee and Dr. Lei Tao. I wish to thank Thomas Miller for designing, building, and guidance on the compact DAQ system utilized in this research. I also want to thank William Lassman for his contribution and guidance on atmospheric modelling and his generosity of sharing his knowledge and results of his analysis. I would like to thank the UAS team who made our aerial measurements possible: Dr. Fred Smith, Charles Rose, Megan Reimann, Collin VanTinburg, and Jared Ham.

Last but not least, I wish to express my gratitude to my wonderful wife, Elaheh Alizadeh. I firmly believe that my research would not have been as successful without her continuous support. I thank her for her support, love, and endless patience.

TABLE OF CONTENTS

Chapter 1: Introduction

This chapter first describes the importance of ammonia detection and the objectives of this research. Next, different techniques used for ammonia measurements will be discussed. The final section describes the process of optical absorption which occurs in the developed optical sensors in this research.

1.1. Ammonia in atmosphere: roles and impacts

Natural Nitrogen (N_2) constitutes ~78% of the troposphere (the lowest layer of atmosphere, with the height of ~10 km). However, extra nitrogen (N) compounds which are generated mostly by anthropogenic activities are one of the major air pollutants which have significant effects on human health and environment. The most abundant nitrogen containing species are ammonia (NH_3), nitric oxide (NO), nitrogen dioxide (NO_2), and nitrous oxide (N_2O). These species constitute 55% (NH_3), 40% (NO_x), and 5% (N_2O) of the total anthropogenic nitrogen emissions in to the atmosphere. Among the several human-made sources of ammonia, agricultural activities and feedlot operations (synthetic fertilizer and animal waste) are the largest sources. Therefore, ammonia is considered as the major nitrogen emission from agricultural sites[1,2].

The process of ammonia emission from agricultural lands is based on ammonification: a series of metabolic activities performed by bacteria or fungi to convert organic nitrogen (e.g. from animal expel) to ammonium[3]. To ensure that the animal's nutritional requirements are met, livestock diets consist of high-protein feed which contains surplus nitrogen. However, cattle for example, only retain ~20% of the nitrogen they are fed, thus ~80% is excreted (via urine and feces) onto the space where they are confined. Over than 50% of the nitrogen fed to cattle in feedlots and dairies is

converted to ammonia in the air[4] and thus ammonia concentrations in the areas nearby animal feeding operations are often between 500 and 1200 ppb which is 100 to 200 times larger than background conditions. Nevertheless, the volatilization process is a function of environmental parameters (e.g. temperature and pH) and design and management of the livestock facilities (e.g. diet and feed supplementation) which make ammonia emission a very complex process. Due to the potential adverse effects of ammonia on ecosystem and air-quality, there has been recent attention to best-management practices for reducing atmospheric ammonia[5]. Stopping or postponing certain activities when some conditions are expected to transport ammonia can avoid or minimize the ammonia transportation (e.g. reducing the amount of lagoon water used for irrigation). The manager could also make improved manure management decisions when the ammonia concentration is above a certain threshold. However, making all these decisions require appropriate technologies with the capability of real time and *in-situ* measurements.

The atmospheric lifetime of ammonia is relatively short (1 to 5 days) and it typically deposits to the ground close to its source[1,6]. This deposition to ecosystems causes eutrophication and acidification of soils which lead to forest extinction and decline in biological diversity[7,8]. Ammonia also readily reacts with atmospheric species such as sulfuric acid (H_2SO_4), nitric acid (HNO_3), nitrous acid (HNO_2) and hydrochloric acid (HCl) to form fine particulate matter ($PM_{2.5}$) which can have harmful effects on human health[9]. The particles also cause haze which lead to visibility reduction, effects on global radiation budgets, and uncertain climate effects[10,11].

It is estimated in the US, 4Tg (4×10^{12} gr) of ammonia is emitted every year into the atmosphere via human related activities which two-thirds of it is due to agricultural operations. However, this number increases to 75% in Colorado[13]. Figure 1.2 shows the contribution of different ammonia sources in the Colorado region.

Figure1.1: a) Interaction of ammonia with atmospheric species forms particular matter $PM_{2.5}$ which causes decreased visibility b) Ammonia deposition on water bodies favors certain weedy species over others, and is likely to cause severe reductions in water quality[12].

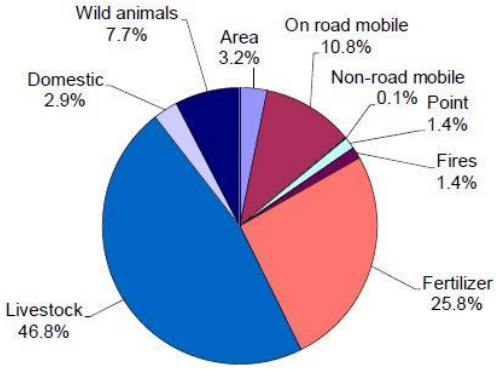

Figure 1.2: The contribution of different ammonia sources in Colorado[14].

It can be seen, after agricultural operations, the second largest source is on-road vehicles which accounts only for 11%[14]. In this region, the highest emissions occur in the northeastern part which is because of large number of concentrated animal feeding operations (CAFOs) in this area. Figure 1.3 shows the locations of large cattle feedlots at northern and north-eastern part of Colorado. Rocky Mountain National Park (RMNP), depicted on the left side of the figure, is ~100 miles away from the eastern feedlots.

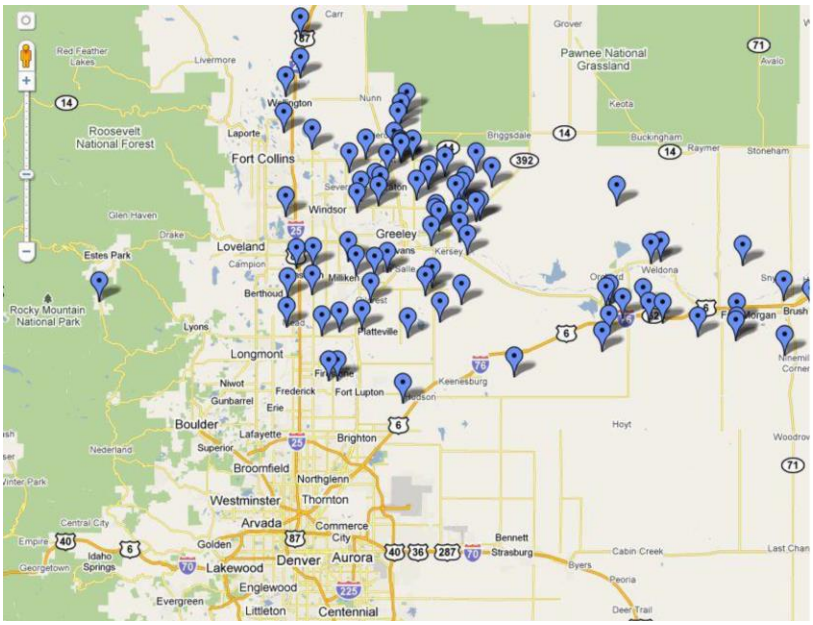

Figure 1.3: Locations of large dairies and cattle feedlots at northern Colorado. Rocky Mountain National Park (RMNP) is depicted on the left side. A feeding capacity of 600,000 cattle is located with 110 miles (176 km) of the park.

Studies[15] have shown RMNP ecosystem has been affected by nitrogen deposition to the park. Ammonia and ammonium (as the nitrogen containing species) are removed from the atmosphere through wet and dry deposition by which nitrogen is added to ecosystem (soils, plants, lakes, and rivers) of the park. The surplus added nitrogen enhances the growth of nitrogen-limited plants, at the expense of other species, and then dominates the vegetation. Undesirable growth of certain plants changes the balance of species[16]. A large study, Rocky Mountain Atmospheric Nitrogen & Sulfur Study (RoMANS)[14], has been conducted to understand the potential sources of nitrogen. In this study atmospheric modelling, field observation, and back-trajectory modelling were combined to estimate the origins of nitrogen deposited in the park[17]. The results of this study show the agriculture and CAFOs as the significant sources of nitrogen. However, there is a considerable uncertainty in the fraction of volatized ammonia that returns to the surface by dry deposition. By measuring the dry deposition of ammonia in the first few kilometers of CAFOs and decreasing the

uncertainty in these areas, the deposition in the park (calculated based on atmospheric models) can be determined more accurately. If a large fraction of emitted ammonia returns to the ground in the first few kilometers of the sources, the impact of CAFOs on RMNP could be overestimated.

In general, understanding how fugitive nitrogen from livestock impacts the environment is a crucial question. Such an impact can be understood by quantifying the fraction of volatilized ammonia from CAFOs that is returned to the surface by dry deposition. In addition, understanding this process could lead to management practices at dairies and feedlots to reduce the ammonia emission.

1.2 Thesis objectives

Significant influences of ammonia on atmosphere and ecosystem, demands fast, precise, and portable sensors to quantify ammonia emission. The main purpose of the work presented in this thesis is to develop open-path laser based sensors for measurement of ammonia emitted from agricultural sites and CAFOs. To pursue this aim, two optical absorption based sensors have been developed using two different techniques: cavity ring-down spectroscopy (CRDS) and wavelength modulation spectroscopy (WMS). The open-path configuration provides high-sensitivity and fast-response measurements in a compact sensor volume.

The work in this thesis first illustrates the application of open-path CRDS sensor in mid-infrared (MIR) spectral region for measurement of atmospheric ammonia (as one of the trace atmospheric species). CRDS is an ultrasensitive technique which relies on the enhanced optical path length provided by a high-finesse optical cavity. The cavity is constructed with two high reflective multilayer dielectric coating concave mirrors. The small needed central area of the mirrors (~mm^2)

makes the measurement region of the CRDS sensor suitable for applications where high spatial resolution is needed.

One of the goals of this study is the aerial ammonia measurements nearby the CAFOs. The aerial measurements are performed using an unmanned aerial system (UAS) because it is more nimble, more cost effective, and safer to operate than manned aircraft. However, the currently available instruments needed for a CRDS system in the MIR region are bulky and power hungry which make CRDS challenging to be deployed on an UAS.

To do the aerial measurements, another sensor based on WMS is developed. The electro-optical setup of the WMS is simple such that the sensor can be compacted (~25 L and ~4 kg) and deployed on the UAS. Measuring ammonia levels with the UAS loaded sensor can provide more information for flux modeling to infer sources and fluxes. Integrating a methane sensor to ammonia sensor provides simultaneous measurements of methane and ammonia. Opposed to ammonia which is affected by both deposition and dispersion, methane concentration is only influenced by dispersion. Therefore, the observed change in the ratio of ammonia to methane downwind (vertically and horizontally) of CAFOs can provide an estimation of the rates of ammonia dry deposition back to the surface within the first few kilometers of these sources.

In brief, the objectives of this study can be expressed as the following:

- Develop open-path CRDS and WMS based sensors for atmospheric ammonia detection and evaluate their performance.
- Miniaturize the WMS sensor (optics, electronics, and data acquisition system).
- Fly miniaturized sensor on an UAS and acquire aerial measurements.

- Demonstrate the feasibility of simultaneous aerial ammonia-methane measurements using a UAS

1.3- Ammonia detection techniques

A number of techniques, including both chemical and optical methods have been used to measure ambient ammonia levels. Chemical ionization mass spectrometry (CIMS) is one of the modern chemical techniques with high time resolution (few seconds). Benson et al have reported ammonia measurement of ~60 ppt in one minute integration time[18]. In another study, CIMS has been compared to another chemical approaches: molybdenum-oxide converter-difference (MoO_x-CD) and citric acid denuder (CAD). The precision of 100 ppt (in 10 seconds), 200 ppt (in 1 hour), and 25 ppt (in 2 hours) have been obtained for CIMS, MoOx-CD, and CAD respectively[19]. Although some of chemical analyzers have sufficient sensitivity and time resolution for most applications, they have some drawbacks which make them too complicated for field measurements. These instrumentations are relatively complex. They are bulky and heavy which introduce challenges for field deployment (e.g. agricultural farms, remote areas). Also, their operation is quite labor intensive. Also, they consume high amount of chemicals.

In addition to chemical methods, optical techniques are useful for ammonia and other gaseous species detection. The optical approaches are attractive since instrumentation can be relatively compact and lightweight (~3 kg) and can provide highly sensitive measurements free from interferences. These techniques, especially laser-based absorption ones, have a great potential for quantitative detection of gas phase absorbers (atoms or molecules). In optical absorption spectroscopy, light wavelength acts like a “fingerprint” of species as each species absorbs light in certain wavelengths. This “fingerprint” effect is used to distinguish the target molecule from

others. Figure 1.4 shows the approximate wavelengths (in mid infrared region) at which different molecules absorb light. A history of application optical techniques for ammonia detection is provided in section 2.3.

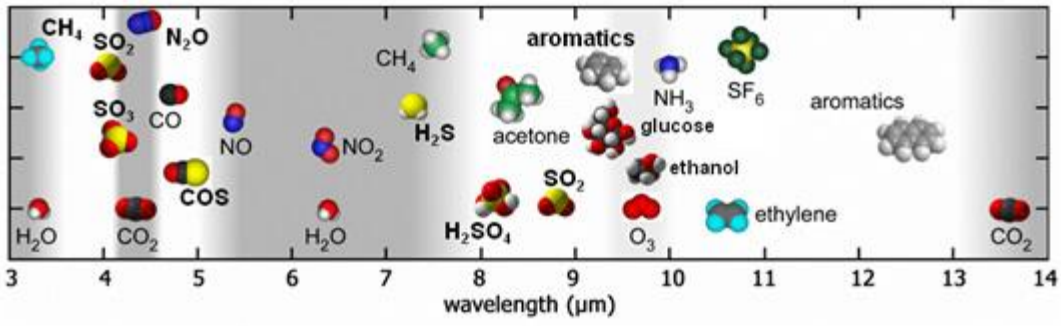

Figure 1.4: Schematic of fingerprints of different molecules at MIR region20.

1.4 The mechanism of optical absorption

The light absorption during molecule-radiation interaction is a complicated process. Understanding of such a phenomenon needs some background knowledge in quantum mechanics and Schrodinger equation. In this section, the physical concepts behind absorption process is provided.

1.4.1 Dipole moment and interaction of light with molecules

The electric dipole moment is a measure of the separation of positive and negative electrical charges within a system. Even though the total charge on a molecule is zero, the nature of chemical bonds is such that in some molecules the positive and negative charges do not completely overlap. Such molecules are said to be polar since they possess a dipole moment (because of the asymmetry in charge distribution which is a result of covalent bonding). Some examples of nonpolar molecules (without dipole moment) are those with mirror symmetry such as O_2. Since the distribution of the electron clouds is symmetrical, the overall dipole moment of the molecule

vanishes and thus they are not active absorbers. On the other hand, an example of polar molecule is water (H_2O) in which electron density of around oxygen atom is higher than hydrogen atoms. H_2O is a "bent" molecule (and not linear like O_2), which means that the individual dipole moments of the O-H bonds are at an angle to each other. They add up to give a net dipole moment.

The vibration of a polar molecule changes its dipole moment and the variation of dipole moment induces an electrical field inside the molecule. When an electromagnetic wave hits a molecule, the interaction of the electrical field of the light beam and the induced electrical field (due to dipole moment) may lead to absorption of the photons[21].

1.4.2 Energy levels of molecules

Quantum mechanics shows the energy levels of atoms and molecules are discrete. When a light wave interacts with a molecule, this interaction can increase the molecule energy levels and thus based on the energy conversation law, the photons of the external light source must be vanished. However, after a very short period of time (~1 ns) the energy of molecule returns to equilibrium and therefore, new photons with the same energy/frequency (but in different directions) are emitted.

The energy levels of a molecule can be classified into three categories: electronic, vibrational, and rotational. Each of these transitions differs by an order of magnitude. The rotational transitions happen at the lowest energies (longer wavelengths) while electronic transitions need photons with higher energies to occur. In general, electronic levels can be excited by ultraviolet (UV) or visible light while vibrational and rotational levels are excited by near-infrared (NIR) or mid-infrared (MIR) light sources. However, changes in vibrational energy are often accompanied by changes in rotational energy, and changes in electronic energy are often accompanied by changes in

vibrational and rotational energy. Figure 1.5 shows a schematic of diatomic molecule energy levels. For a certain electronic energy level, the vibrational curve shows the potential energy (Morse energy) of the molecule system. It is obvious that when the distance between atoms is infinity the potential energy tends to a constant number which means the atoms are not tied together anymore and they are free (zero of potential energy is arbitrary). Also, a strong repulsive force is applied when the atoms get very close together. There is an equilibrium bond distance at which the potential energy of the system of atoms (molecule) is minimum and the atoms vibrate around it.

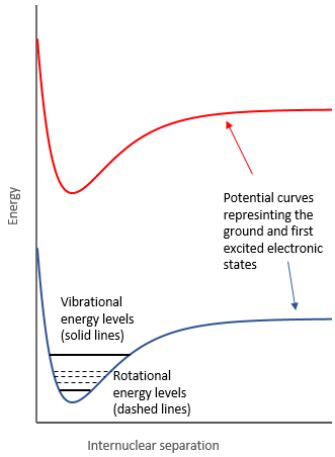

Figure 1.5: Energy levels of a diatomic molecule.

Diatomic molecules such as hydrogen bromide (HBr) are the simplest cases to analyze their vibrations and rotational energy levels. For such a simple case, the internuclear forces (which cause vibrations) can be simulated by a spring (which obeys Hooke's law) that two atoms have been attached to its ends. If one atom is much heavier than the other one, we can assume the center of mass of the system (molecule) is located on the heavier atom and then the lighter atom bounces back and forth while the heavier one is assumed stable (in fact, it moves a little, though much smaller than the hydrogen). As an example, HBr is a molecule in which the atomic weight of

Bromine is ~80 times bigger than Hydrogen. Under this assumption, the hydrogen atom vibrates around the equilibrium internuclear distance. For such a diatomic molecule, instead of complex Morse energy function, a simple harmonic oscillator (SHO) model can be applied to simplify the calculations of vibrational energy levels. By applying linear force spring from Hooke's law (SHO), the fundamental vibration frequency of diatomic system can be obtained as equation 1.3:

$$f_{vib} = \frac{1}{2\pi}\sqrt{\frac{k}{m}} \tag{1.1}$$

In this equation *k* is the stiffness of the bond (i.e. the spring constant) and *m* is the hydrogen atom weight (in a case that the weights of two atoms are comparable, *m* should be replaced by the reduced mass). By solving Schrodinger equation and determining the energy levels of the harmonic system we can show that the energy levels of SHO is discrete and depend on vibrational quantum number *v*:

$$E_n = hf_{vib}\left(v + \frac{1}{2}\right) \quad , \quad v = 0,1,2,3, \ldots \tag{1.2}$$

In this equation *h* is Planck's constant ($h = 6.62 \times 10^{-34}$ $\mathrm{m^2 kg/s}$).

The transition in vibrational energy levels occur when the molecular energy increases from a lower *v* to a higher value. However, the quantum mechanics solution leads to a simple selection rule, namely that the during a transition vibrational quantum number can change only by 1 and otherwise the probability of transition is zero.

$$\Delta v = v_2 - v_1 = 1 \tag{1.3}$$

Nevertheless, as it was mentioned above, SHO is only an approximation of the real potential energy of the molecule. In a more realistic case, anharmonic terms should be counted. Equation

1.4 (total energy for an oscillating diatomic system) can be improved after adding anharmonic terms:

$$E_v = hf_{vib}\left(v+\frac{1}{2}\right) + hf_{vib}X_e\left(v+\frac{1}{2}\right)^2 + higher\ order\ terms \tag{1.4}$$

In this equation X_e is the first anharmonicity constant.

In addition, the improved model of vibrational potential modifies the selection rule for allowed changes in vibrational quantum number and this permits the additional possibility of transitions other than $\Delta v = 1$. In the modified version of the selection rule, the vibrational quantum number changes are permitted to be other than 1 and $\Delta v = 1,2,3,$ .... (the transitions with $\Delta v \neq 1$ are called overtone bands). However, the transitions with $\Delta v = 1$ are much stronger than overtone bands and the transition probabilities diminish rapidly with increasing magnitude of Δv[21].

In addition to vibration, molecules rotate too. For instance, in the simplified example of HBr molecule, the hydrogen atom can rotate around the center of mass, which is very close to the bromine atom. Quantum mechanics shows that the rotational energies of the system is discrete. For the simplified example of diatomic molecule, the rotational energy levels can be obtained by solving the Schrodinger equation.

$$E_J = \frac{h^2}{8\pi^2 I}J(J+1) \qquad J = 0,1,2,3,\ldots \tag{1.5}$$

In this equation J is the total angular momentum vector (rotational quantum number), I is the moment of inertia, and h is the Planck's number (note that a linear molecule such as HBr has only one moment of inertia, $I_1 = I_2 = I\ ,\ I_3 = 0$). Equation 1.7 is true for a rigid rotator in which the distance between the atoms is constant, however during the rotation, vibration occurs too in the

molecules. The effect of vibrational stretching and non-rigidities lead to a modified rotational energy form as:

$$E_{J,v} = B_v J(J+1) - D_v J^2 (J+1)^2 \quad (1.6)$$

The subscript v of B_v and D_v denotes the rotational energy dependence on vibrational energy. The quantum mechanical solution to Schrodinger's equation also yields selection rules for rotational transitions, namely that the change in rotational quantum number (J_2-J_1), for diatomic molecules can only be +1, -1, and 0 (for diatomic molecules $\Delta J = 0$ is forbidden). The transitions with $\Delta J = +1$, $\Delta J = -1$, and $\Delta J = 0$ are named as R, P, and Q branches, respectively.

For polyatomic molecules, such as ammonia (NH_3), the equations and math behind the transitions and energy levels are more complicated. Ammonia is a pyramidal symmetric top molecule with a bond angle of 107.8°. It has four pairs of electrons (five from nitrogen atom and three from hydrogen atoms). Three of these electron pairs bond the central nitrogen to the hydrogen atoms. The one pair left alone repels the N-H bonds and this makes the bond angle ~2° smaller than expected for a regular tetrahedral arrangement. Such a configuration makes ammonia a permanent dipole molecule which can interact with IR and MIR radiation.

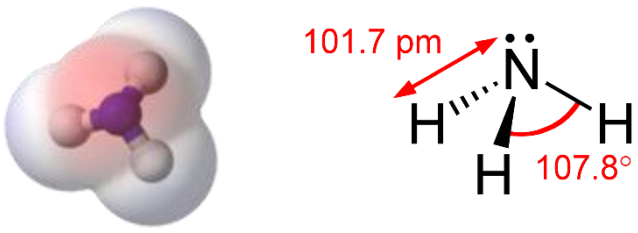

Figure 1.6: Ammonia is a permanent top symmetric pyramidal molecule[22].

In spherical molecules, such as CH_4, the three moments of inertias (corresponding to principal axes) are the same I. For such molecules, the rotational energy levels obtained by Schrodinger's

equation are the same as for linear molecules (equation 1.7). However, the ammonia is a "semi-symmetrical" molecule and its moments of inertias are such that $I_1 = I_2 < I_3$. Thus, the energy levels are governed by a different equation which is expressed as below (at the first approximation)[23,24]:

$$E_J = \frac{\hbar^2}{2I_3} J(J+1) + \hbar^2 \left(\frac{1}{2I_3} - \frac{1}{2I_1}\right) K^2 \quad , \quad J = 0,1,2,3,\dots \quad , \quad K = 1,2,\dots,J \tag{1.7}$$

Again, *J* is the total angular momentum vector and *K* (with the selection rules: $\Delta K = 0, \pm 1$) is the projection of J on molecular axis.

Similar to multiple rotational energy levels in polyatomic molecules, there are different vibrational modes too. Depending on the net change of the dipole moment, each mode can be IR active or inactive. The number of vibrational modes of a nonlinear polyatomic molecule with *N* atoms is 3*N*-6. Therefore, the ammonia molecule can vibrate in six different ways. Figure 1.7 shows these 6 vibration modes. The blue and white spheres represent nitrogen and hydrogen atoms and their movement is shown by yellow arrows. Each vibrational mode consists of several absorption lines. The strongest absorptions correspond to the symmetric bending mode (v_2 band), the motion of nitrogen through the plane of three hydrogen atoms and vice versa. This motion is shown in second picture of figure 1.7.

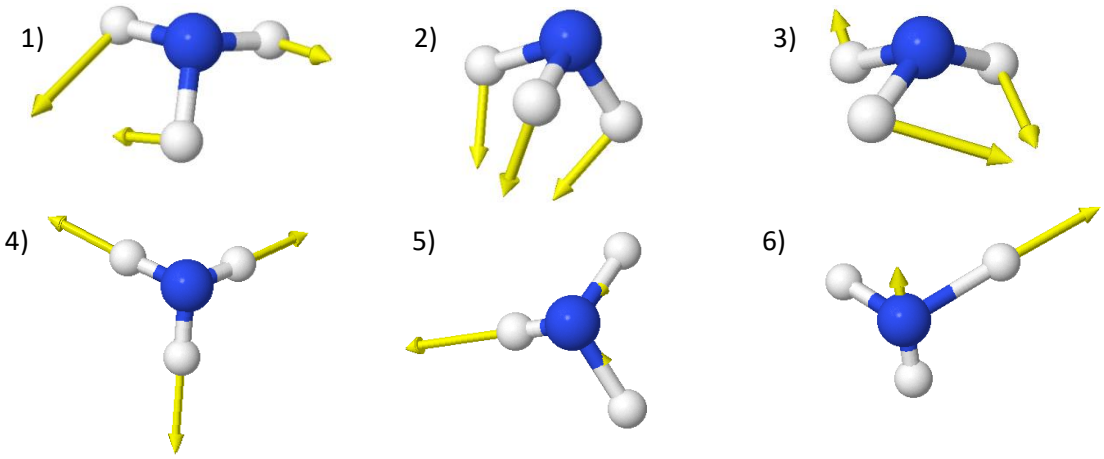

Figure 1.7: Six different bending and stretching vibrational modes of ammonia molecule25. The second mode (v2) comprises the strongest absorption lines occurring at ~960 cm-1.

There are several possible ro-vibrational transitions in the ~950 cm^{-1} area corresponding to v_2 band. The potential energy curve between the nitrogen atom and the plane of hydrogen atoms leads to two minima (and one barrier). This is against a linear molecule which its potential curve has one minimum point. The two minima points correspond to the equilibrium position of the nitrogen atom on either side of the hydrogen atom planes. The existence of the barrier results in a doubling of vibrational energy levels (known as symmetric and antisymmetric states). Thus, there are two vibrational ground levels: 0(a) , 0(s) and two excited levels: 1(a) , 1(s). One of the strong absorptions occurs through the Q branch transition $(0(\mathrm{s}) \rightarrow 1(\mathrm{a}),\ \Delta J = \Delta K = 0,\ J = K = 3)$ at 967.34 cm^{-1} (corresponding to 10.337 μm) which is the wavelength of the light source used in this study[23].

1.4.3 Absorption spectra

Absorption spectroscopy is based on Beer-Lambert law that describes light intensity attenuation during passing through a sample (gas, liquid, or solid). As it was mentioned in previous section, if molecular composition of the sample is polar and the energy of the incident photons is matched

with the energy needed for a specific transition, some photons of the electromagnetic wave are absorbed by the sample. The number of the vanished photons is quantified by Beer-Lambert law. According to this law, the light intensity before and after the sample obey the equation below:

$$I(\nu)=I_0\, e^{-\alpha(\nu)l} \tag{1.8}$$

In this equation I_0 and I (in W) are the light intensity before and after the gas sample, α (in cm^{-1}) is the absorption coefficient which is a characteristic of the sample (e.g. the polarity of the molecules in the sample) and proportional to target molecule concentration, l (in cm) is sample length, and ν (in Hz) is the frequency of the light. Note that frequency in unit of Hz can simply be converted to wavenumber in cm^{-1} and wavelength in μm using the following equations:

$$\nu[cm^{-1}] = \nu[Hz] / c \tag{1.9}$$

$$\lambda[\mu m] = 10^4\, c/\, \nu\, [Hz] \tag{1.10}$$

Where c is the speed of light in the unit of cm/s.

Equation 1.10 shows that if the gas sample does not have any absorption at the wavenumber/frequency ν (i.e. the photons energy does not match with any allowed transition), the light intensity does not change when passing through the sample. In other words, the strength of a sample to absorb light is specified by absorption coefficient (α) which itself depends on few parameters:

$$\alpha(\nu, \nu_0) = \frac{CPN_A}{RT} \times S(\nu_0) \times \varphi(P, \nu, \nu_0) \tag{1.11}$$

Where:

C = Concentration of sample (mixing ratio)

P = Pressure [atm]
N_A = Avogadro's number [molecule/mole]
R = Gas constant [J/mol.K]
T = Temperature [K]
$S(v_0)$ = Line strength at wavenumber v_0 [cm/molecule]
$\varphi(P, T, v, v_0)$ = Absorption profile [cm]

In equation above C is a unitless parameters and can be written as ppm (ppb) which is part per million (billion) by volume; i.e. volume of target species per 10^6 (10^9) volumes of ambient air.

The lineshape function $\varphi(P, T, v, v_0)$ reflects the relative variation from the central wavenumber (v_0) in the absorption coefficient. This variation with wavenumber is caused by broadening mechanisms (mostly due to pressure and temperature) in the medium. The concept behind lineshape is that the absorption in a molecule is not "sharp" and it does not happen for a single light beam wavenumber. Rather, there is a range of wavenumbers at which the absorption occurs. Although the absorption is maximized at wavenumber v_0, there are still non-zero absorptions at wavenumbers nearby v_0. The width of the feature Δv, is defined by the width at half the maximum value (the full at half maximum, or, FWHM).

The integral of φ over wavenumber (v) is defined to have no dimensions and since the unit of wavenumber is cm^{-1}, then φ should be in unit of cm.

Broadening of an absorption feature occurs due to phenomena in the sample that perturb the transition's energy levels or the way in which individual atoms and molecules interact with light. If all molecules in the medium are affected in the same way, the broadening is said to be homogeneous. However, if there are some groups of molecules which are affected differently from others, the broadening is said to be inhomogeneous. Two broadening mechanisms that occur in

absorption spectroscopy are collisional broadening (homogenous) and Doppler broadening (inhomogeneous).

Collisional broadening

The frequent collisions between molecules in a gas distorts their energy levels. The wavenumber uncertainty due to collisional effects, Δv_C, is the line-shape's halfwidth (FWHM). This uncertainty directly depends on the gas pressure. For the target species *j*, Δv_C is often modelled as the product of the system pressure and sum of the mole fraction for each perturbing species *i* multiplied with its process-dependent collisional broadening coefficient $2\gamma_{ij}$:

$$\Delta v_C = P \sum_i C_i \gamma_{ij} \tag{1.12}$$

In this equation C_j is the concentration of the species whose lineshape is being studies and $C_{i\neq j}$ are the concentrations of all other species. Therefore, for example $2\gamma_{NO-NO}$ is the broadening coefficient for collisions between NO molecules (self-broadening) and γ_{NO-NO_2} is the coefficient due to NO and NO_2 collisions. Even though, in most cases only two coefficients are enough to be considered: 1) coefficients due to self-broadening and 2) coefficients due to air broadening. The air broadening is the mass averaged O_2 and N_2 coefficients. However, in trace gas measurements in which the species being studied have the concentrations in order of ppb, one can neglect the self-broadening term. The values of γ_{i-air} need to be determined experimentally.

The line-shape of a collisional broadening has the Lorentzian form (equation 1.16). The coefficient of $1/2\pi$ makes the integral over frequency equal to 1 ($\int_{-\infty}^{+\infty} \varphi \, dv = 1$).

$$\varphi_C(P,T,v,v_0) = \frac{1}{2\pi}\frac{\Delta v_C}{(v-v_0)^2 + (\frac{\Delta v_C}{2})^2} \tag{1.13}$$

Doppler broadening

The velocity of a molecule relative to the propagation of the light beam shifts the frequency at which the absorption happens. This effect is called Doppler shift. In any temperature higher than 0 *K*, all molecules of a gas sample are in constant and random motion. The distribution of the random velocities is described by Maxwell velocity distribution function. A class of velocities can be made by considering each group of molecules with velocities in a specific range. Each velocity class has its own Doppler shift. The Maxwellian distribution function specifies what portion of molecules are in each class. The broadening due to Doppler effect is inhomogeneous since different molecules (with different velocities) are classified into different classes. The lineshape function with Maxwellian function has a Gaussian form:

$$\varphi_D(P,T,v,v_0) = \frac{2}{\Delta v_D}\sqrt{\frac{\ln 2}{\pi}}e^{-4\ln 2\,(\frac{v-v_0}{\Delta v_D})^2} \tag{1.14}$$

Line-shape's halfwidth of doppler broadening is the following:

$$\Delta v_D = v_0 \times 7.1623 \times 10^{-7}\sqrt{\frac{T}{M}} \tag{1.15}$$

Where *T* and *M* are temperature and molecular weight in K and gr/mole, respectively.

If the Lorentzian linewidth is much bigger than the Gaussian linewidth ($\Delta v_C \gg \Delta v_D$), the Gaussian component can be ignored. Such approximation is applicable for cases at which the sample is in high pressures ($P \geq$ ambient pressure). For those cases that both Doppler and collisional are

significant and neither can be neglected the overall lineshape is the combination of the two. This combination (called Voigt function) is defined as the convolution of the Doppler and collisional broadening[21].

Once the lineshape of a molecule (φ), the environmental parameters (T, P), the concentration (C), and the line-strength (S) at a certain frequency (v_0) is known, the absorption coefficient of the molecule can be determined. The function that describes the variation of absorption coefficient versus frequency is called the molecule spectra. Figure 1.8 shows the absorption profile of different species at the wavenumber range of 1924.75 cm^{-1} – 1927.50 cm^{-1}.

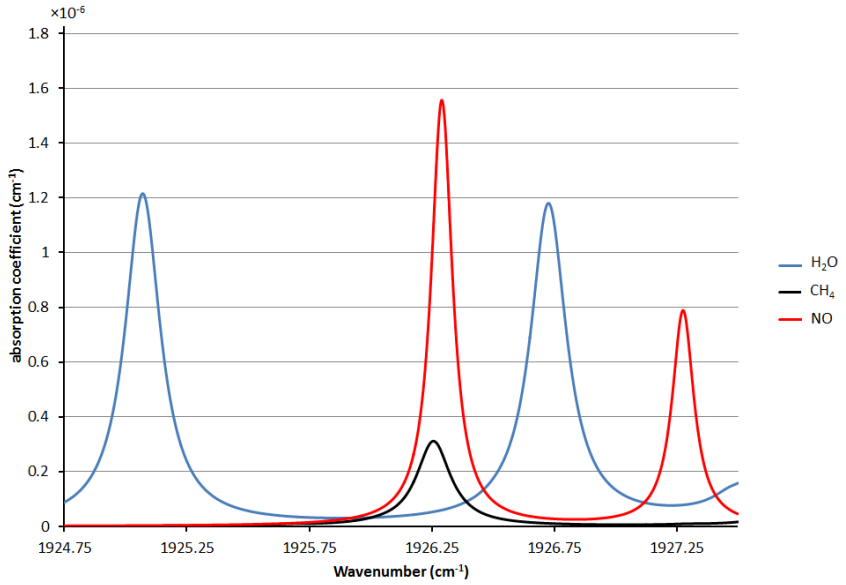

Figure 1.8: Absorption profile of few species at the wavelength range of 5.188 µm - 5.195 µm. [CH_4]=390 ppm, [NO]=200 ppb, HR=10% ([H_2O]=2600 ppm).

Chapter 2: Absorption spectroscopy

In this chapter, the basic devices in absorption spectroscopy based systems and basic physical concepts behind such sensors are provided. Next, the strategies to increase the sensitivity of the sensors as well as the previous studies on ammonia measurements using optical sensors are discussed.

2.1 Optical devices used in absorption spectroscopy

2.1.1 Lasers

The strongest absorption features of most of interesting gases occur in NIR-MIR spectral region (1 μm -15 μm) which are based on their rotational-vibrational modes[26]. A semiconductor tunable diode laser (TDL) is a good candidate as the light source for an absorption spectroscopy based system. The typical frequency linewidth of such lasers is 5 MHz and the beam can be assumed monochromatic in absorption spectroscopy since FWHM of a typical absorption profile is 15 GHz. Also, the size (~ cm^3) and the weight (<100 gr) of these lasers make them very attractive in designing absorption based gas analyzers.

With respect to theory of their operation, diode lasers (DL) and light emitting diodes have some elements in common. The major difference is that, in a DL the major emitting process is stimulated emission while in an LED, the spontaneous emission overcomes. Essentially, an LED is a "sandwich" in which the "bread" is made by P type (with too many holes) and N type (with too many electrons) semiconductor materials. As the LED is powered (positive terminal of the battery connected to P and negative terminal of the battery connected to N), electrons flow across the P-N junction and combine with holes on the other side, and give out the extra energy in the form

of photons. In a laser diode, different materials are used as the semiconductor layers to make the photons with a certain and suitable energy. These photons interact with more incoming electrons, helping to produce more photons with the same wavelength and phase (stimulated emission). However, the stimulated emission occurs at much higher current, typically 10 times greater than a normal LED. Figure 2.1 compares the optical power of LED and LD. The spontaneous emission based light power out of the LED increases steadily as the diode current increases. In a laser diode, the optical power in low input currents is low and purely due to spontaneous emission. However, there is a threshold current at which the stimulated emission begins and for currents above that the optical power grows dramatically. For both LED and LD, there is an upper limit for input driven current in to the diode such that higher currents more than that will destroy the module.

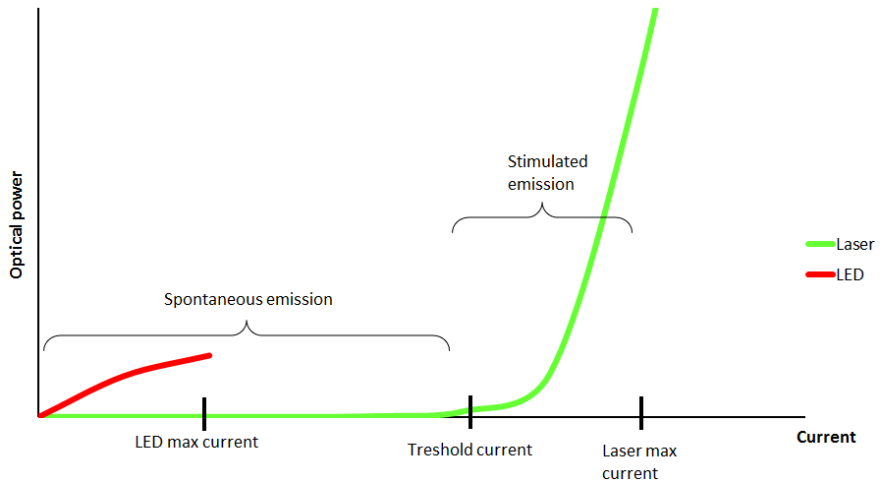

Figure 2.1: The comparison of LI curves of Laser diode and LED.

In a laser diode when the driven input current increases (decreases), both the laser optical power and laser wavelength increase (decrease) simultaneously. In absorption spectroscopy, having a laser with stabilized wavelength (frequency) is crucial since the laser wavelength should cover the absorption profile of the target species. Therefore, the current through the laser diode must be carefully regulated and controlled. Also, laser diode parameters are highly dependent on the

junction temperature. Higher temperature leads to higher threshold current, lower optical power, and lower wavelength. For this reason, highly stable temperature control is desirable. In a typical absorption spectroscopy based system, the temperature of the laser is kept constant while the input current is scanned over a certain range (which leads to wavelength scanning) to cover the whole broadened absorption feature of the target species[27,28].

2.1.2 Optical Detectors

Another crucial component in absorption spectroscopy technique is the detector by which the light intensity is detected. The most common optical detectors working in NIR-MIR region are photodiodes. A photodiode is a semiconductor device that converts light into an electrical current. The magnitude of the generated current depends on the optical power of the incident photons on the active area of the detector. Essentially, a photodiode is a PN junction . When a photon with adequate energy hits the junction, it creates an electron-hole pair. A photo-current is produced while the holes move toward the anode and electrons move toward the cathode.

One of the important features of a photodiode is its responsivity. The responsivity at a specific light wavelength is the ratio of the generated photocurrent to incident light power, expressed in A/W. The spectral responsivity is a graph of responsivity values at various wavelengths. Another aspect of a photodiode which should be considered is the response time defined as the time that takes for the generated photocurrent to appear. The bandwidth of the photodiode is proportional to the inverse of the response time and it is typically expressed in MHz. The signal to noise ratio is another important feature of a photodiode. The noise equivalent power (*NEP*) of a detector is defined as the optical power at which the produced photo-current equals the amplitude of the noise current. Since the amplitude of the noise is proportional to square root of the noise

bandwidth, it is expressed in the unit of $A/Hz^{1/2}$ instead of A. Having the definition of noise current and responsivity, the *NEP* can be termed as the equation below:

$$NEP[W/Hz^{1/2}] = \frac{I_{noise}}{R} \quad (2.1)$$

Where R[A/W] and I_{noise}[$A/Hz^{1/2}$] are the responsivity and noise current of the photodiode, respectively. The detectivity (D) of a photodiode is defined as the inverse of the *NEP*.

$$D=1/NEP \quad (2.2)$$

A more general parameter that can be used to compare the performance of different systems independent of photodiode area and bandwidth is specific detectivity (D^*). It is defined as the detectivity multiplied by the square root of the area of the photodetector, for a 1 Hz bandwidth.

$$D^*[cmHz^{1/2}/W]=DA^{1/2}=\frac{R\sqrt{A}}{I_{noise}} \quad (2.3)$$

A higher detectivity value indicates a low-noise device[29].

2.2. Direct absorption spectroscopy

2.2.1- The application of Beer-Lambert law

In absorption spectroscopy, gaseous sample concentration is quantified using the Beer-Lambert law (equation 1.10). A light beam is passed through the sample and if the frequency of the light matches the absorption profile of the target species, the beam intensity decreases after the gas sample. Beam intensity reduction is measured and this reduction could be converted to sample concentration.

Direct absorption spectroscopy (DAS) is the simplest technique among different absorption based methods. In this technique, the laser wavelength is tuned by tuning the driven current into the diode laser. The typical waveforms by which the laser current is modulated are sawtooth and triangle waves with the frequency range of 10–100 Hz. Depending on the laser characteristics, the DC component and amplitude of the input current should be adjusted such that the scanned wavelength covers the absorption profile of the target molecule. The beam intensity after the sample (I) during each scan period is acquired for all covered wavelengths using an optical detector. The detector converts the optical power of the laser into a voltage signal which can be measured by an oscilloscope or a fast data acquisition (DAQ) system. Figure 2.2 shows a schematic of a typical DAS system. The measured fractional transmission (I/I_0) of the incident beam obeys the Beer-Lambert law:

$$I(v)/ I_0(v)= e^{-\alpha(v)l} \tag{2.4}$$

A useful parameter for describing the beam intensity reduction is fractional absorbance which is defined as below:

$$\frac{\Delta I}{I_0} = \frac{I_0 - I}{I_0} = 1 - e^{-\alpha(v)l} \tag{2.5}$$

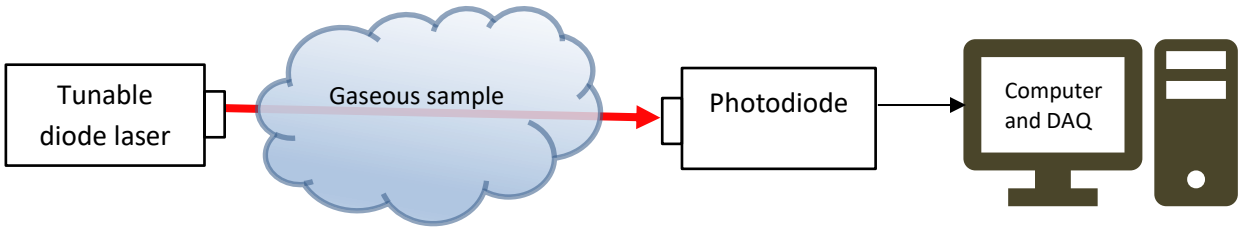

Figure 2.2: A schematic of a DAS based system. The light beam intensity after the absorption via the sample is acquired by a photodetector and the output of the detector is analyzed by the DAQ system.

In the optically thin conditions ($\alpha l \ll 1$) the fractional absorbance can be expressed as:

$$\frac{\Delta I}{I_0} \cong 1 - (1 - \alpha l) = \alpha l \tag{2.6}$$

Optical thin condition is true for most atmospheric trace species detection which have low concentrations in order of ppb.

There are few ways by which the beam intensity in absence of absorption (I_0) can be determined. If the measurement region is kept in low pressure (~0.1 atm), the FWHM of the absorption feature is narrow enough so that the frequency (wavelength) scanning of the laser covers some areas at which there is no absorption. By fitting a linear (or polynomial) function to the two ends of the spectra, the I_0 can be determined. In figure 2.3, the dashed red line is calculated I_0 by fitting a linear function on the two tails of the absorption feature. Note that when the wavelength of a diode laser is tuned, its intensity is simultaneously tuned. The optical power variation of the laser at some extent has the same form of the wavelength modulation.

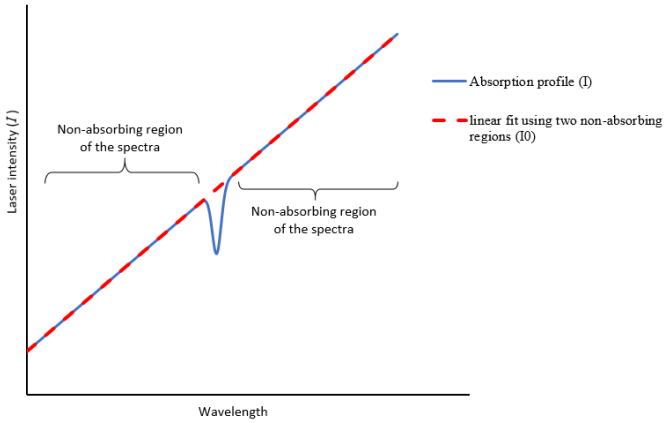

Figure 2.3: This graph shows one period of the wavelength scanning. The blue curve is the light intensity after the absorption (I) which is acquired experimentally. The dashed red line is the initial laser power (I_0) which is determined by fitting a linear function on the two non-absorbing tails.

This method can be used only if the pressure is low enough compared to the scanning range of the laser and the target molecule absorption feature does not have any interference with other species.

Another way for obtaining I_0 is purging the measurement region or flowing a high purity species that does not have any absorption in the laser wavelength region. The acquired laser power with such a purge (flow) can be saved as I_0 and will be used when the absorbing species appear in the system.

If the initial laser power (I_0), the environmental parameters (T,P), target species characteristics (S), and the path length of the sample (l) are known, the concentration (C) of the species can be determined using the Beer-Lambert law as the following:

$$\alpha(v) = \frac{CPN_A}{RT} \times S(v_0) \times \varphi(T, P, v, v_0) = \tag{2.7}$$

$$-\frac{\ln\frac{I(v)}{I_0(v)}}{l}$$

$$\rightarrow \frac{CPN_A}{RT} \times S(v_0) \times \int_{-\infty}^{+\infty} \varphi(T, P, v, v_0)\, dv = \tag{2.8}$$

$$-\frac{1}{l}\int_{-\infty}^{+\infty} \ln\frac{I(v)}{I_0(v)}\, dv$$

$$\rightarrow C = -\frac{RT}{lS(v_0)PN_A}\int_{-\infty}^{+\infty} \ln\frac{I(v)}{I_0(v)}\, dv \tag{2.9}$$

In these equations, C is mixing ratio which is unitless and can be written as parts per million (ppm) by multiplying by 10^6. The species density ($\mu g/m^3$) can also be determined by obtained mixing ratio using the following equation in which M [gr/m^3] is the molecular weight of the species.

$$C[\mu g/m^3] = 10^6 \frac{MP}{RT} C[\text{ppb}] \tag{2.10}$$

2.2.2- The limitations of DAS and strategies to improve the sensitivity

Most atmospheric species have low concentrations in order of ppm, ppb (or even ppt). For example, the ambient concentration of ammonia (NH_3) is only few ppb. The simulated absorption profile of ammonia at the wavelength of 10.33 μm for such a low concentration with ambient pressure and temperature shows the absorption coefficient of ~10^{-7}cm^{-1}. For a typical distance of 50 cm between the laser and detector in a DAS system, the fractional transmission and fractional absorbance can be determined (equations 2.4 and 2.5):

$$I/I_0 = e^{-50\times10^{-7}} = 0.999995 \tag{2.11}$$

$$\frac{\Delta I}{I_0} = 5 \times 10^{-6} \tag{2.12}$$

The nominal values for the responsivity and noise of a detection system (detector+amplifier) in the MIR region are R=10^3 V/W and N=10^{-3} V (these values are dependent on few parameters such as the material of detector and bandwidth of the amplifier). Using equation 2.15, the detector voltage drop (ΔV) due to ambient ammonia absorption can be determined as $\Delta V = V_0 \times 5 \times 10^{-6}$. Assuming a typical laser power of 10 mW, the detector output without sample (V_0) would be 10 mW × 10^3 V/W=10 V. With these nominal numbers, the voltage drop can be determined as $\Delta V = 5 \times 10^{-5}$ V $= 50$ μV which is much smaller than the intrinsic detector noise ($\Delta V \ll N$). In other words, such a small signal drop (which is due to low ammonia concentration) cannot be detected since the ratio of signal to noise is less than one (S/N<1) and the signal is "lost" in the noise system. The detector is not the only source of noise in a DAS system. The other sources such as laser controllers and DAQ system will add more noise in the acquired signals. Although averaging multiple periods of laser scanning decreases the noise contribution, a typical DAS system with the

laser-detector separation of tens of centimeter cannot be used for the measurements of trace gaseous species (such as ammonia) in the atmosphere.

To improve the sensitivity of an absorption spectroscopy based sensor, the signal to noise ratio in low concentrations should increase. This can be performed either by increasing the signal or decreasing the noise in the system.

Equation 2.5 shows that the voltage drop due to absorption is directly proportional to the path-length between the laser and the detector. Therefore, one way to increase the signal (voltage drop due to absorption) is lengthening the laser-detector distance. Increasing the physical distance between the laser and the detector up to tens of meters is doable[30]. A suitable combination of various optical equipment (lenses and mirrors) should be used to avoid the beam divergence in the far distances. However, such long pathlengths cannot be applied to applications at which low spatial resolutions are needed. Alternatively, an optical cavity, comprised of two opposed concave mirrors to fold the beam in a small volume can be used. While the mirrors distance can be shortened to only few tens of centimeters, folding the beam by multiple reflections from mirrors lead to a remarkable increase in the effective optical path length (up to ~10 km)[31,32]. Such a design makes the beam travel through a small and constant volume while the effective path-length is high enough for low concentrations measurements.

Noise reduction is another strategy to increase the signal to noise ratio. In this approach, the laser beam is modulated and then the detector output is demodulated using a lock-in amplifier (a noise rejection device).

2.3 The history of ammonia detection with optical based sensors

Different optical absorption techniques based on ammonia absorption in the near-infrared (800 nm to 2.5 μm) and mid-infrared (2.5 μm to 14 μm) spectral regions have been developed including direct absorption spectroscopy (DAS)[33], amplitude modulated photo-acoustic spectroscopy (AM-PAS)[34], integrated cavity output spectroscopy (ICOS)[35], infrared laser differential absorption spectroscopy (ILDAS)[36], and cavity ring-down spectroscopy (CRDS)[37]. The reported sensitivities in these studies are shown in table 2.1.

Table 2.1: The sensitivity obtained by different optical techniques.

	DAS	AM-PAS	ICOS	ILDAS	CRDS
Sensitivity	50 ppt (1s)	3.4 ppb (1s)	90 ppt (1s)	230 ppt (1s)	50 ppb (20 s)

The measurement of atmospheric ammonia is critical and challenging. There are several reasons behind this challenge: 1) ammonia is a trace species with typical background concentration of few ppb, 2) its concentration levels vary widely, 3) it is a "sticky" species[38] meaning that it reacts with many of the surfaces it makes contact. The latest one becomes a problem when the atmosphere to be tested is being sampled rather than tested directly. Specific strategies are needed to conquer this problem and minimize the adsorption effects. In fact, all (optical and non-optical) techniques mentioned above are sampling techniques in which ambient air is flowed in to a closed-path cell and measurement is based on the sampled air. These techniques can suffer from adsorption leading to memory effects, high response time, and decreased accuracy and precision. The sampling issues can be particularly problematic during field measurements with rapidly changing atmospheric conditions. Shortening the tubes by which air is flowed inside the cell, using specific kind of materials for inlet (teflon), and heating and keeping the tubes and cell in high temperatures (~40 C) are some strategies that can help for minimizing adsorption effects [35,39]. Indeed, in closed-path

absorption spectroscopy a vacuum pump is needed to keep the pressure inside the sample cell low and consistent. Opposed to closed-path techniques, an absorption spectrometer with open-path configuration can eliminate sampling issues since there is no need for sampling the ambient air and it flows freely across the probe laser beam. Removing the inlet can also be enabling for compact and low power designs because bulky, heavy, and power-hungry flow systems and vacuum pumps are removed. Recent studies have examined open-path optical sensors for ammonia detection.

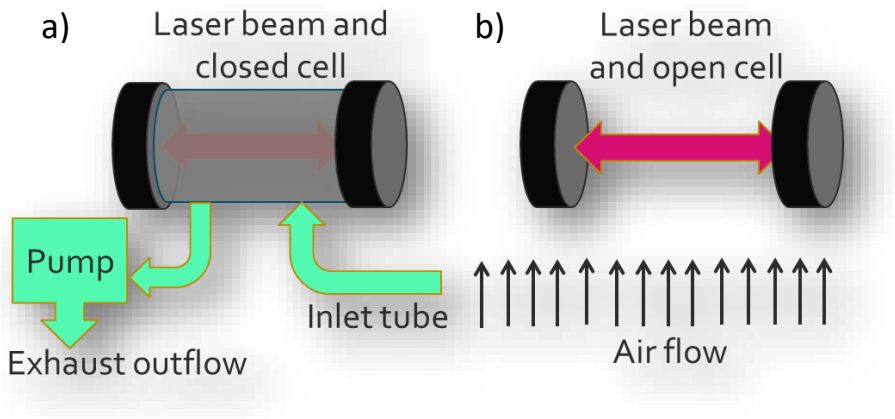

Figure 2.4: The comparison of (a) closed-path and (b) open-path configurations in an absorption spectroscopy based system.

Some of these methods attain their sensitivity by exploiting long path lengths. Open-path Fourier transform infrared (FTIR) spectroscopy has been demonstrated with precision of several ppb with a path of 96 m[30]. Volten et al.[40] and Mount et al.[41] employed differential optical absorption spectroscopy in the mid-ultraviolet region (~200-230 nm) obtaining sensitivities of 0.2 ppb in 5 minutes over 100 m path length, and few ppb in 1 second over 60 m path length, respectively. Direct absorption spectroscopy with long optical path has also been utilized by McManus et al. with mid-infrared (MIR) quantum cascades lasers (QCLs) with precision of 1.4 ppm-m at 20 Hz [33]. While applications like fence-line monitoring benefit from long physical path lengths, it is often

desirable to have more compact sensors that provide point measurements with spatial resolution <~1 m. Using multi-pass cells is one of the approaches by which optical paths of few tens of meters can be obtained. WMS with a multi-pass cell in open-path configuration has been used by Miller et al.[42] for ammonia detection with sensitivity of 0.15 ppb at 10 Hz and a large dynamic response spanning concentrations from sub-ppb to several ppm. Another alternative for obtaining long effective path lengths (≥1km) is using optical cavities[43]. Open-path cavity-enhanced absorption spectroscopy was shown by Peeters et al.[44] with a 1.5 μm laser yielding a detection limit of 100 ppb in 1 second; a level that is marginal for measurement of atmospheric ammonia. Another optical cavity based method is CRDS, a widely used technique that yields high sensitivity based on long effective path lengths and immunity to laser power fluctuations (since decay rates are measured) [43]. In addition to being highly sensitive, the method is attractive since it is directly quantitative and insensitive to laser power variations. He et al. have recently demonstrated an open-path CRDS configuration with a near-infrared (NIR) diode laser (1.531 μm) yielding precision of ~11 ppb for ammonia in nitrogen[45].

In this research, the focus is developing two compact and light weight CRDS and WMS based sensors for detection of ammonia emitted from agricultural sites. In order to improve the sensitivity of WMS based sensor, it is integrated with a Herriot multipass cell. Both sensors are in open-path configuration and the sample gas (ambient air) flows directly through the cavities. In both sensors, a quantum cascade laser (QCL) is utilized to cover the strongest absorption feature of ammonia located in mid-infrared (MIR) spectral region (10.33 μm). The CRDS and WMS based sensors have shown the sensitivity of ~1.5 ppb (at 1 second) and ~4 ppb (at 1 second), respectively. The CRDS based sensor has shown the capability of open-path cavity ringdown spectroscopy for high sensitive measurements in MIR spectral region. It is the first demonstration of an open-path CRDS

based sensor working in mid-infrared MIR, to our knowledge. However, the currently available instruments needed for a CRDS system in the MIR region are bulky and power hungry. Such instruments make the detection system undesirable for applications where compact (<4 kg, <20 L) and low power (<30 W) sensors are needed. Aerial measurements using unmanned aerial systems (sUAS) is one of the applications that needs such light weight and low power sensors. Opposed to CRDS, WMS does not need complicated and bulky instruments and its physical simplicity makes it a good choice for UAS based measurements. The WMS-Herriot cell based sensor is light weight (~4 kg) and consumes ~25 W electrical power. It has been used for terrestrial (using a vehicle) and aerial (using a UAS) ammonia measurements around different sources of ammonia including traffic congestion (combustion) and feedlots (cattle).

Chapter 3: Development of Open-Path CRDS sensor

In this chapter, the Gaussian beam and theory of CRDS technique are discussed as well as the performance of the developed open-path CRDS sensor for ammonia detection.

3.1 – Gaussian beam and optical cavities

A laser beam is an electromagnetic radiation with perpendicular electric and magnetic fields. The wavelength (frequency) of the electrical field specifies the beam spectral region between ultraviolet (<300 nm) and far infrared (>15 μm). Regardless of the beam wavelength, the behavior of the electrical and magnetic components of the radiation is governed by wave equation which itself is derived by Maxwell's equations.

A solution for wave equation can be expressed as the following form which describes the beam (electric field) profile in *x*-*y* plane at different spots on z axis.

$$E(x,y,z,t) = E_0 \frac{w_0}{w(z)} e^{-\frac{x^2+y^2}{w^2(z)}} e^{-i\frac{2\pi k(x^2+y^2)}{2R(z)}} e^{-i(2\pi kz+\tan^{-1}(z/z_R)-\omega t)} \quad (3.1)$$

Where:

E_0: electric field amplitude at the origin at time t=0,

k: beam wavenumber (the inverse of the wavelength)

w: beam spot size (the radius at which the field amplitude falls to 1/e of its axial value)

w_0: beam waist (minimum beam spot size)

ω: beam frequency

R: beam curvature (the surface at which all points have the same phase)

z_R: Rayleigh range (the region that the beam is considered collimated)

$$z_R = \frac{\pi {w_0}^2}{\lambda} \tag{3.2}$$

$$w = w_0 \sqrt{1 + (\frac{z}{z_R})^2} \tag{3.3}$$

$$R = z(1 + (\frac{z_R}{z})^2) \tag{3.4}$$

The wave equation solution is obtained by few preliminary guesses:

1- Although the beam is considered collimated for a finite distance on *z* axis, we observe that beam expands as it propagates.

2- The amplitude of the laser beam is finite. The nominal laser beam diameter is ~few millimeters and the amplitude of the solution should have a maximum at *x*=*y*=0 and then decrease for points away from *z* axis. The beam spot size is defined as the distance at which the amplitude of the electric field drops to 1/e of its maximum value (E_0).

The first assumption is met by equation 3.4 that demonstrates the beam spot size expands as it travels. Based on this equation, the Rayleigh range (z_R) is the distance at which the beam spot size is expanded by a factor of $\sqrt{2}$ and the beam is called "collimated" in this region. As a numerical example, in order to have a 2 m collimated beam using a laser with 10 μm wavelength, one should make a beam waist of $w_0 = \sqrt{1 \times 10\ \mu m/\pi} = 1.78$ mm using a lens with proper focal length.

The second assumption is satisfied by the Gaussian term ($e^{-\frac{x^2+y^2}{w^2(z)}}$) which shows the amplitude reduction in the *x*-*y* plane relative to *z* axis.

Another important aspect related to a gaussian beam is its wavefronts and the radius of curvature (*R*). The wavefront is defined as the surface that contains all points of the wave that carry the same

phase. Since the beam expands during the propagation then its wavefront must have a spherical shape (opposed to a plane wave which has planar wavefront). This spherical wavefront is described by phase term $e^{-i\frac{2\pi k(x^2+y^2)}{2R(z)}}$. The beam radius of curvature is governed by equation 3.5. Figure 3.1 shows the beam spot size and beam curvature at different spots on *z* axis. Obviously, the values of *R* for both near and far field distances are infinity: $\lim_{\substack{z\to\infty \\ z\to 0}} R = \infty$.

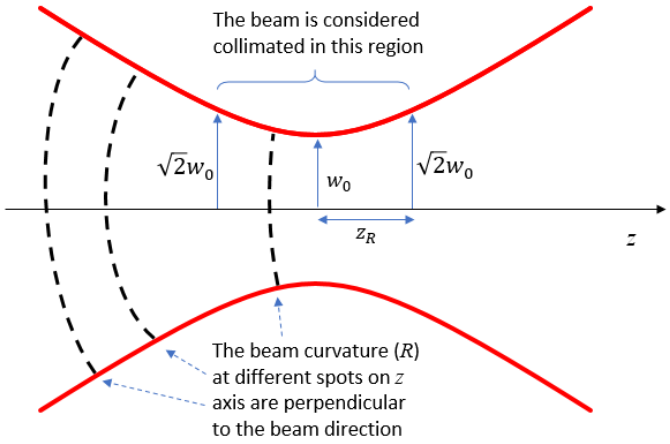

Fig 3.1: The variation of beam spot size (solid red) on z axis and the beam curvature (dashed black).

Equation 3.4 describes the beam expand for an ideal laser beam. In real lasers, the beam characteristics deviate from ideal case and the equation 3.4 should be replaced by the following:

$$w = w_0\sqrt{1 + M^2(\frac{z}{z_R})^2} \tag{3.5}$$

M^2 is the quality factor of the laser. Obviously, for an ideal beam this parameter is equal to one. However, for most commercial lasers $M^2 > 1$.

The intensity of an electromagnetic wave (the optical power per unit area) is proportional to absolute magnitude of the electric filed and is expressed as the following gaussian form:

$$I = I_0 e^{-2\frac{x^2+y^2}{w^2(z)}} \tag{3.6}$$

Where I_0 is the beam intensity on the source.

Equation 3.2 is the simplest solution of the wave equation but not the only one. In fact, there are infinite number of solutions that can satisfy the wave equation. The general solution can be expressed as the Hermit-Gaussian form:

$$E_{lm}(x,y,z,t) =$$
$$E_0 \frac{w_0}{w(z)} H_l(\frac{\sqrt{2}x}{w(z)}) H_m(\frac{\sqrt{2}y}{w(z)}) e^{-\frac{x^2+y^2}{w^2(z)}} e^{-i\frac{2\pi k(x^2+y^2)}{2R(z)}} e^{-i(2\pi kz+\tan^{-1}(z/z_R)-\omega t)} \tag{3.7}$$

Where H_l and H_m are the l^{th} and m^{th} order of Hermite polynomials. The Hermit-Gaussian modes are designated TEM_{lm} (which stands for Transverse Electro Magnetic). The gaussian solution in equation 3.2 can be displayed as the fundamental modes TEM_{00}. Different TEM_{lm} modes have different spatial distributions. The fundamental mode is a pure gaussian beam with one peak while higher order modes (l,m>0) have several peaks[46].

The light output of a laser is due to the interaction of the stimulated based photons with the laser cavity. For most applications having the fundamental mode TEM_{00} out of the laser is desired. Therefore, designing an appropriate optical cavity to have the TEM_{00} is crucial. Indeed, external optical cavities are used in absorption spectroscopy to enhance the detection sensitivity. The optical cavity is an arrangement of optical components by which light interaction with matter is enhanced. A common optical component used to design a cavity is a pair of high reflective (e.g. %99.99) opposing concave mirrors. When a laser beam hits the first mirror, a small portion of the optical power is injected in to the cavity (since the reflectivity of the mirrors is not %100). The electromagnetic field inside the cavity becomes excited (and increases in amplitude) at some

specific wavelengths (equation 2.12). The distribution of electric field out of an optical cavity is characterized by equation 3.9; however, one can match the beam to the fundamental mode of an optical cavity such that the beam transmitted through the exit mirror has the fundamental mode TEM_{00} (assuming that the beam itself is a TEM_{00} gaussian beam with M^2~1). For example, in the case of a cavity constructed by two opposing concave mirrors, if the beam curvature on two mirrors matches the mirrors curvature, the exiting beam from the cavity will be in the TEM_{00} mode. Matching the mirror and beam curvatures can be performed by using a combination of two thin lenses[47]. A good mode-matching requires both mathematic calculations (including ray tracing) and careful alignment.

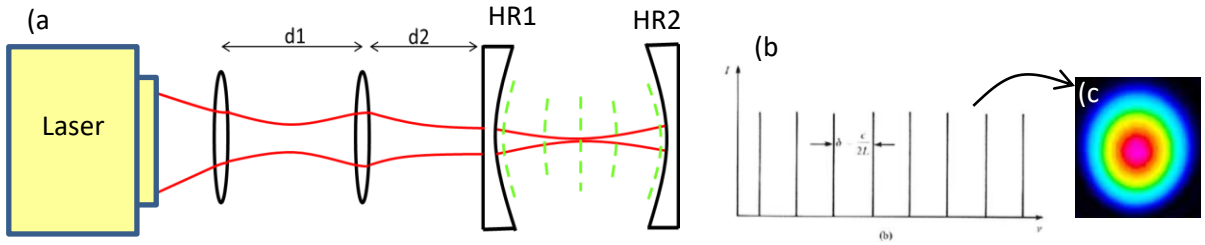

Figure 3.2: a) The combination of two lenses is used to match the curvature of the beam (dashed green line) and mirrors. d_1 and d_2 are calculated based on the lenses focal lengths, mirrors curvatures, and mirrors distance. b) With scanning the laser wavelength, only those which satisfy the resonance condition (separated by *FSR*) will exit the cavity. c) The TEM_{00} modes (pure gaussian) out of the cavity.

Two important parameters in optical cavities are free spectral range (*FSR*) and cavity finesse ($\mathcal{F}$). *FSR* is the frequency spacing between successive longitudinal modes which is the reciprocal of the round trip time: $FSR[Hz]=c/2l=1/t_r$, where $2l$ is the cavity roundtrip length and c is speed of light. A common figure of merit of a cavity is $\mathcal{F}$ which is the ratio of *FSR* over the full width at half maximum of the cavity resonances ($\Delta\nu_c$).

$$\mathcal{F} = \frac{FSR}{\Delta\nu_c} = \pi\frac{\sqrt{R}}{1-R} \tag{3.8}$$

The width of the cavity resonances is a function of mirror's reflectivity. The higher the reflectivity of the mirrors, the narrower the cavity resonances and the higher the cavity finesse. It can be sown that the effective enhanced absorption length is proportional to cavity finesse. For example two mirrors with reflectivity of %99.99 will result the finesse of ~30,000 and 10^4 passes which means with a physical distance between two mirrors of 50 cm, the effective path length will be 5 km[43].

3.2 – Theory of CRDS

CRDS is an absorption spectroscopy measurement technique, which can be performed with pulsed or continuous light sources and has much higher sensitivity than that in conventional direct absorption spectroscopy. It provides extremely high-sensitivity measurements by employing an optical cavity to enhance the optical path length. The first application of CRDS goes back to 1981 when it was used for high precision measurements of mirror reflectivity by measuring the phase shift of a continuous wave (cw) laser exiting the cavity[48]. Later, in 1984 Anderson et al. advised a technique by which the photon life time in the cavity was measured by switching off the laser and monitoring the decay of light intensity at the detector over time [49]. The first application of CRDS in spectroscopic measurement was shown with a pulsed laser in 1988[50]. In 1997 cw-CRDS was used for spectroscopic measurements[51]. It has also recently been used to measure optical properties of aerosols[52]. It is currently one of the well-known techniques in atmospheric monitoring, combustion diagnostics, and plasma diagnostics. In this technique lifetime of the photons inside an optical cavity is measured rather than optical intensity leaking out of the cavity and this makes the measurements immune to laser power fluctuations. Furthermore, the technique is self-referencing (i.e. it does not require external calibration).

The basic idea of CRDS is placing the absorbing sample between two high reflectivity mirrors of an optical cavity. A laser beam (pulsed or continues) is coupled into an optical cavity where it is reflected back and forth many times. At the same time, a detector placed behind the cavity monitors the optical power leakage out of the rear mirror (since the reflectivity of the mirrors is not 100%). After trapping sufficient light within the cavity, the optical power is switched off quickly and intensity of light transmitted through the exit mirror will decay exponentially [53]:

$$I(t,v) = I_0(v)e^{-t/\tau(v)} \tag{3.9}$$

Where $\tau(v)$, known as ring-down, is the time at which the optical intensity drops to *1/e* of the initial value. Since different cavity modes lead to different ring-down values, in order to minimize the variation ring-down, it is crucial to match the beam with the cavity and excite only fundamental TEM_{00} modes. Ring-downs can be extracted by performing an exponential fit to the measured signal by detector. For a given physical properties of the cavity (i.e. mirrors separation distance and their reflectivity) the ring-down time is merely a function of absorption coefficient inside the cavity (which itself is a function of laser frequency):

$$\tau(v) = \frac{L}{c[1-R+\alpha(v)L]} \tag{3.10}$$

Where *c*, *R*, *L*, and *α(v)* are speed of light, mirror reflectivity, cavity length, and absorption coefficient of the gas sample, respectively. It is assumed that the whole space between mirrors has been uniformly filled by the sample. Empty ringdown time ($\tau_0(v) = \frac{L}{c(1-R)}$) can be measured in absence of target molecule absorption when *α(v)=0* (e. g. non-absorbing medium or detuning the laser from absorption feature). Using τ_0 (as a fixed parameter) and acquired $\tau(v)$, the sample absorption can be determined by the following equation.

$$\alpha(v) = \frac{l}{c}\left(\frac{1}{\tau_0} - \frac{1}{\tau(v)}\right) \tag{3.11}$$

If the laser wavelength is tuned over the entire absorption feature of the target molecule, species concentration can be obtained by $\int \alpha(v)\mathrm{d}v$ and the known spectroscopic parameters of absorption feature (equation 2.9).

Another alternative to measure the concentration would be to fit the inverse of acquired ringdowns to a Voigt profile. One of the free parameters calculated by the fitting algorithm is proportional to gas concentration. Again, using known spectroscopic parameters and environmental conditions (pressure and temperature), gas concentration is determined. The latter method is appropriate for open-path configuration because in high pressure (e. g. ambient pressure) most of the species features have overlapping interference from neighboring features. Interference causes the "empty ringdown time" vary with adjacent species concentration and thus τ_0 is no longer a fixed value.

Figure 3.3 shows a schematic of a typical CRDS setup. The free spectral range of a cavity with mirrors separation of 50 cm is 300 MHz (0.01 cm^{-1}) and the typical FWHM of cavity resonances (for R~99.99%) is ~10 kHz.

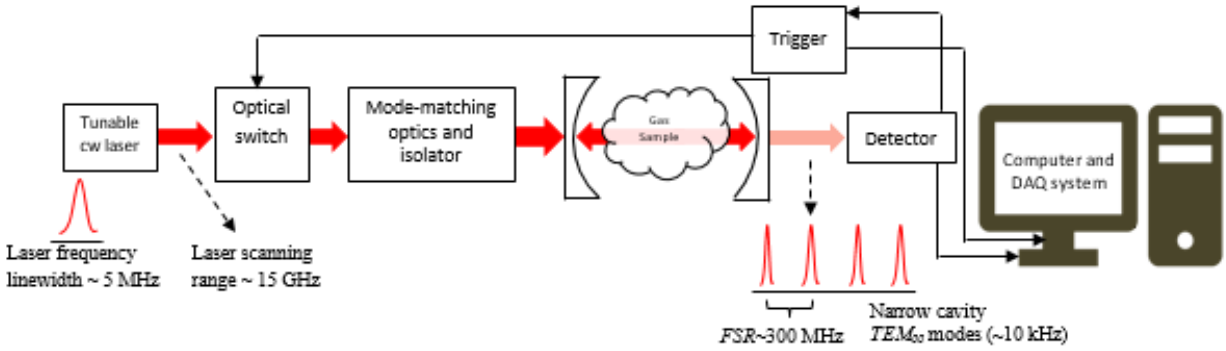

Figure 3.3: Schematic of a typical CRDS setup.

Such narrow cavity resonances and high *FSR*, enables a diode laser (with frequency bandwidth of few MHz) to excite single longitudinal modes of the optical cavity by modulation of the laser frequency. A nominal frequency scanning range to cover absorption feature is 15 GHz which results ~50 data points (15 GHz/300 MHz) at each scan.

The minimum detectable absorption of a CRDS system depends on the uncertainty in measurement of ring-down time in absence of absorption[54].

$$\alpha_{min} = \frac{(1-R)}{l}\frac{\Delta\tau}{\tau} \tag{3.12}$$

Based on this equation, having higher reflectivity mirrors provides more resolution by decreasing the numerator and at the same time increasing the denominator.

Optical switch and isolator

In CRDS having a fast optical switch is crucial to extinguish the laser beam once enough optical power is built up inside the cavity. Acousto-optic modulators (AOM) allow the intensity of light to be controlled and modulated at high rates (>10 MHz)[55].

In an acousto-optic modulator, sound waves (usually at radio-frequency) are used to diffract the light beam. A piezoelectric transducer is attached to an optical transparent material (crystal) and an oscillating electric signal drives the transducer to vibrate which creates the acoustic waves in the optical material. These vibrations cause refractive index wave which acts as sinusoidal grating in the crystal. The interaction of the incoming laser beam with the periodic index modulation causes the light scattering in different directions (modes). Depending on the optical and acoustic wavelengths, there is a certain angle between the optical and acoustic propagations at which the

first order scattered light has the maximum optical power. The angle between the zeroth order beam (the non-scattered portion of the beam) and first order is defined by the equation:

$$\theta = \frac{\lambda}{\Lambda} \tag{3.13}$$

Where λ and Λ are the optical and acoustic wavelengths.

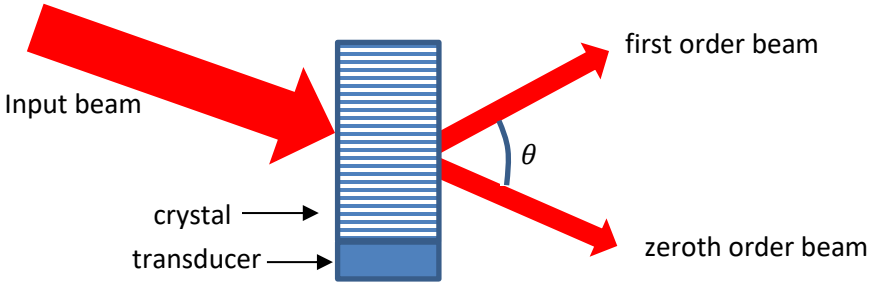

Figure 3.4: Acoustic optical modulator.

In CRDS the first order beam out of the AOM is directed into the optical cavity. Once one of the TEM_{00} modes of the cavity is detected by the optical detector, the RF input of the AOM is switched off and therefore, for a short period of time (<500 μs) no light is injected into the cavity. During the AOM extinction time, the optical power leaked out of the cavity is acquired by the detector and a DAQ system measures the ringdown time.

Another crucial component in a CRDS system is the optical isolator to block the reflected beam from the first cavity mirror from going back into the laser. Such reflections make noticeable instabilities in the laser. An optical isolator can be composed of a polarizer and a quarter waveplate (QWP). The output of the polarizer is a horizontal linear polarized beam that passes though the QWP. The QWP changes the linear to the right circularly polarization (Figure 3.5).

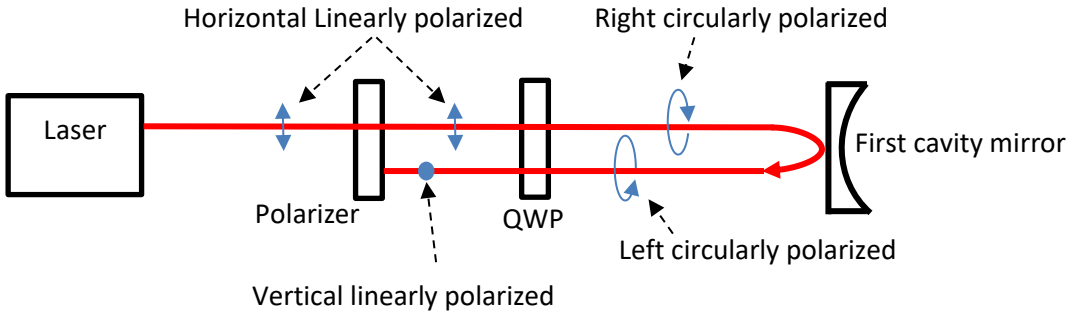

Figure 3.5: A combination of a polarizer and a quarter waveplate in series can be used as an optical isolator. The beam polarization at each location is shown in blue.

The beam reflected from the first mirror has the same circular polarization but with 180 degrees phase change which makes it left circularly. When the reflected left circularly polarized beam passes through the QWP, its polarization changes to vertical linear which is blocked by the polarizer.

3.3 - Development of CRDS sensor

3.3.1 - Wavelength selection and laser characterization

As it was mentioned, in absorption spectroscopy, finding a strong absorption feature of the target molecule is crucial. Most molecules have their strongest fundamental ro-vibrational absorption bands in the MIR region. Figure 3.6 shows the absorption lines of ammonia in different wavelengths. As it was mentioned in section 1.3.2, the strongest absorptions appear at the 10 μm region (ν_2 band) which are >100 times stronger than NIR lines (~1.55 μm). Spectral interferences from other molecules must also be considered, particularly for atmospheric pressure (open-path) configurations where linewidths are considerably wider than for low pressure operation (~0.1 atm) typical of closed-path configurations.

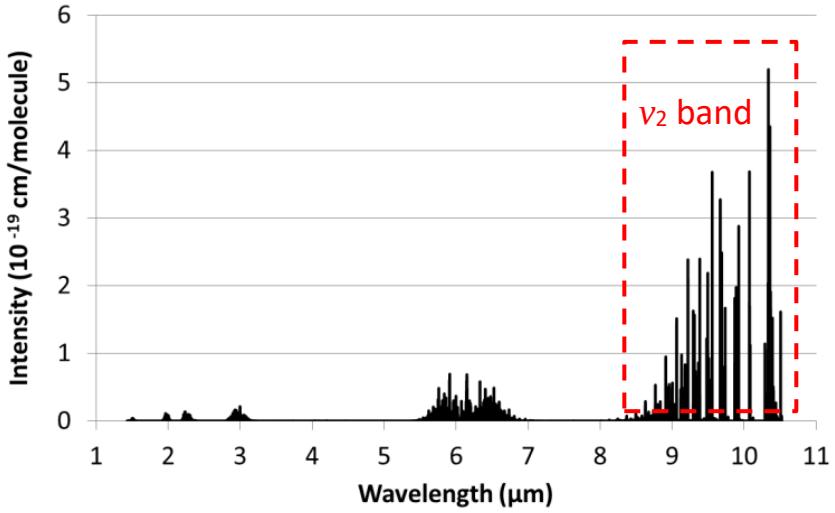

Figure 3.6: Absorption lines of Ammonia in NIR and MIR regions.

Water absorption lines are particularly challenging in this regard. Even weak absorption cross-sections (as much as a factor of 10^{-10} weaker than ammonia) can make interference with ammonia bands. At ambient pressure and temperature, ammonia has two well isolated features located at 9.06 and 10.33 µm (each composed of multiple individual absorption lines) suitable for our sensor. In this study, the stronger feature at 10.33 µm (967.35 cm^{-1}) has been chosen which has also been used by other researchers[24 33,36] The strongest individual line (ν_2, Q branch, $(J = 3, K = 3) \rightarrow (J = 3, K = 3)$) contributing to this feature has linestrength of 5.2×10^{-19} *cm/molecule* and is positioned at 10.337 µm (967.347 cm^{-1}). Figure 3.7 shows a simulated absorption spectrum for 100 ppb concentration of ammonia at typical Colorado ambient conditions as well as the neighboring water and carbon dioxide features. The spectrum was determined with HITRAN parameters[26] for line locations, strengths, and pressure broadening. No other HITRAN species have absorption in this region for typical ambient concentrations.

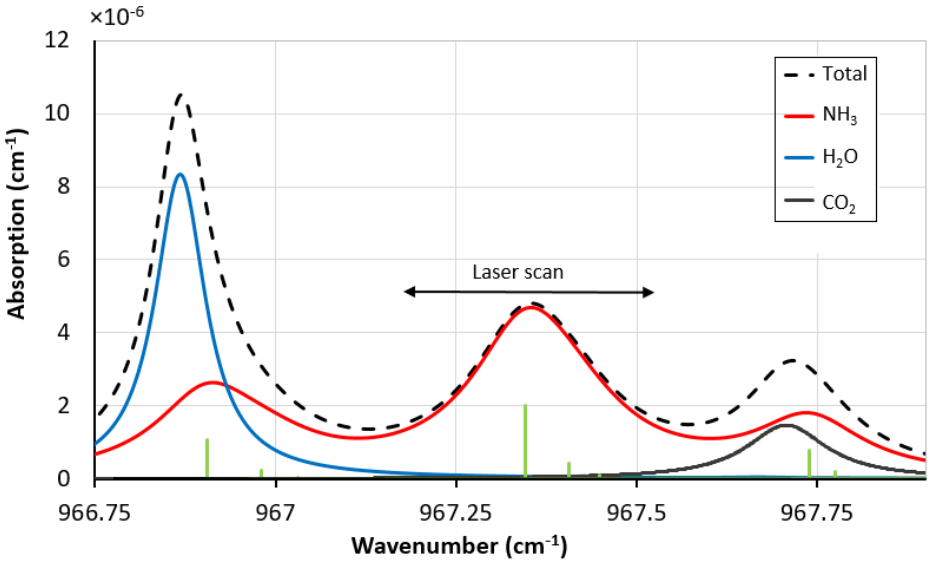

Figure 3.7: Simulated absorption spectrum in the vicinity of the ammonia absorption line. Simulated conditions are: P = 0.85 atm, T = 298 K, [NH_3] =100 ppb, [CO_2]=400 ppm, [H_2O]=0.013 (50% Relative Humidity). The laser scan range is shown with an arrow. For ammonia, the contributing absorption lines are shown as green sticks.

One of the light sources in MIR spectral region is lead salt lasers. However, they need to be operated at cryogenic temperatures (typically below -73°C). They produce only low power levels (~1 mW) and their wall-plug efficiency (the ratio of the input electrical power and output optical power) is very low ~%0.01. The advent of Quantum Cascade Lasers (QCL) has provided greater access to MIR region with compact sources that work in room temperature and do not require cryogenic cooling[56]. In this study, we have used a single-mode cw thermoelectric-cooled distributed feedback (DFB) QCL with a tuning range of 10.325 µm (968.50 cm^{-1}) to 10.345 µm (966.65 cm^{-1}). The spectral linewidth is a few MHz, and the maximum output optical power is ~60 mW.

QCL is a semiconductor laser and its wavelength is set by the diode temperature and the current that is driven in to it. The threshold current at which our laser starts emitting is ~250 mA. In order to set the needed current and temperature for our target wavelength, a low pressure 20 cm long

cell with high ammonia concentration (~1000 ppm) is used as a reference cell. In low pressure, the absorption lines are narrower and it is straightforward to distinguish the target line among others which have interference with other species in low concentrations and high (ambient) pressure.

The relative laser frequency during scanning is obtained by fitting a second-order polynomial to a Fabry-Perot Germanium etalon (with *FSR*=3 GHz) transmission peaks. Etalon is an interferometer which consists of two partially reflective parallel surfaces. When a light beam strikes each reflective surface, a portion of that penetrates and passes through it and the rest is reflected. This process happens multiple times such that the net beam intensity after the second reflective surface gets an interference form.

If the beam perpendicularly strikes the surfaces, it can be shown that the beam transmission after the second surface obeys the following equation[46]:

$$I = I_0 \frac{1}{1+\frac{4R}{(1-R)^2}(\sin(\frac{2\pi nd}{\lambda}))^2} \tag{3.14}$$

Where R, I_0, d, n, and λ are surface reflectivity, incident light power, surfaces distance, refractive index of the material, and light wavelength, respectively. The total transmission is maximum when the following condition below is.

$$\begin{cases} \lambda = 2nd/m \\ \quad or \\ v = mc/2nd \end{cases}, \ m = 0, \pm 1, \pm 2, ... \tag{3.15}$$

Where v and c are the light frequency and speed. The frequency spacing between two consecutive peaks of transmitted optical intensity is called free spectral range (*FSR*) and can be determined as the following:

$$FSR[Hz] = \Delta v = \frac{c(m+1)}{2nd} - \frac{c(m)}{2nd} = \frac{c}{2nd} \tag{3.16}$$

Free spectral range can be expressed in wavenumber: $FSR[\mathrm{cm}^{-1}] = 1/2nd$. Equation (2.13) shows that for an etalon with certain values of *d* and *n*, the frequency spacing is a constant number and independent of the absolute laser frequency. Therefore, the number of peaks in the optical transmission of an etalon can be used for determining the relative frequency range that the laser covers. For example, if three peaks are detected, the scanning range is somewhere between 2*FSR* and 3*FSR*. The more precise relative frequency calibration is obtained by fitting a second-order (or third order) polynomial to etalon transmission peaks.

Figure 3.8 shows a comparison between experimental (using etalon and low pressure cell) and simulation (using HITRAN dataset[26]) of absorption ammonia features in low pressure (~0.1 atm).

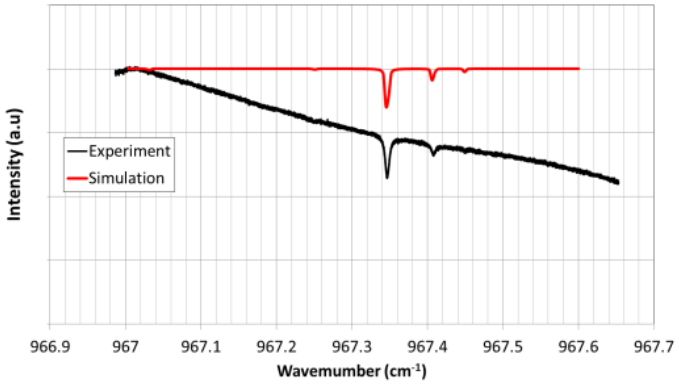

Figure 3.8: Simulated and experimental ammonia absorption feature in low pressure**.** In experimental graph: DC current=344 mA, AC amplitude=50 mA, Temperature=30 ˚C.

In this experiment, the low-pressure cell is mounted between the laser and an optical detector. The laser current is tuned using a low noise laser diode driver (Wavelength electronics, QCL500) while the laser temperature is stabilized at 30˚C by a thermoelectric temperature controller (Wavelength

electronics, PTC5k). The applied laser current is a combination of two DC and AC signals with 344 mA and 50 mA amplitudes, respectively.

This experiment shows that applying 344 mA DC current in to the diode when its temperature is 30°C makes the laser wavelength of 10.337 μm (967.35 cm^{-1}). An AC signal with 20 mA amplitude is sufficient to cover target ammonia feature at ambient pressure which is ~0.4 cm^{-1} (12 GHz) wide. The laser scan range is shown with an arrow in figure 3.8.

3.3.2 - Experimental

3.3.2.1 - CRDS setup

Figure 3.9 shows a schematic of the setup of the open-path CRDS sensor. The laser beam emitted from QCL is condensed and collimated by the optical telescope constructed by two plano-convex germanium lenses for passage through an AOM (IntraAction Corp, AGM-402A21.20). The angle between the main beam and first diffracted beam in our setup is ~2.2 degree (this deviation is not shown in figure 3.9). The AOM is nominally powered on, with its 1st-order diffractive beam directed in to the cavity. After the AOM, a polarizer (Thorlabs WP25H-Z) and quarter-wave plate (Alphalas Corp PO-TWP-L4-25-FIR) are used in series to provide optical isolation against beams reflected back from the cavity toward the laser. Two plano-convex germanium lenses are used to spatially mode match the beam to TEM_{00} modes of the cavity [47].

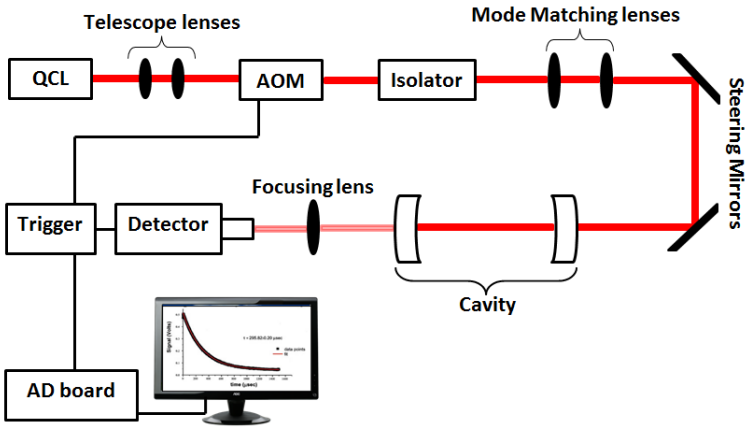

Figure 3.9: Schematic of open-path CRDS setup.

The optical cavity itself is 50 cm in length and formed from two plano-concave high reflectivity (HR) dielectric mirrors (II-VI Inc.) with reflectivity of R=%99.95 and radius of curvature of 1 m. The light exiting the output cavity mirror is focused by a germanium lens on a Mercury Cadmium Telluride optical detector (VIGO PVMI-2TE-10.6) placed 20 cm from the rear mirror. The detector responsivity is ~10^3 V/W and it is configured with a high bandwidth 50 MHz integrated preamplifier. An additional inline amplifier (Phillips Scientific 6950) provides a gain of 10. A custom trigger circuit monitors the detector signal and when a preset threshold is exceeded, corresponding to the laser frequency overlapping a TEM_{00} cavity mode, the trigger circuit quickly switches off the AOM voltage to extinguish light injection to the cavity and allow for a ring-down decay. The combination of trigger circuit and AOM allows light extinction in ~120 ns once the cavity resonance is detected. This method of spectrally scanning the laser across the cavity, with no active locking or cavity modulation, provides relatively high optical sensitivity in a simple configuration [57,58]. After the trigger circuit fires, the ring-down decay is recorded with a high speed data acquisition (DAQ) card (Adlink PCIe-9842). High acoustic power driven into the AOM generates ~200 W heat which needs to be dissipated by a water cooling system to keep the AOM in the room temperature range. Figure 3.10 shows the open-path CRDS sensor.

High speed DAQ card digitizes the ring-down signal at a rate of 10^8 samples/s. Each individual ring-down signal is fitted with an exponential decay (plus baseline) to find the ring-down time, τ. The ring-down fitting is performed by a custom LabVIEW program using a Levenberg-Marquardt nonlinear least squares algorithm. The individual ring-down times, $\tau(\nu)$, are converted to optical absorption (loss) as $k(\nu)=1/c\tau(\nu)$, where c is the light speed. For each ring-down decay (or optical absorption) the relative laser frequency is found based on fitting a second-order polynomial to etalon transmission peaks. Fitting coefficients have been found to be stable over at least several months.

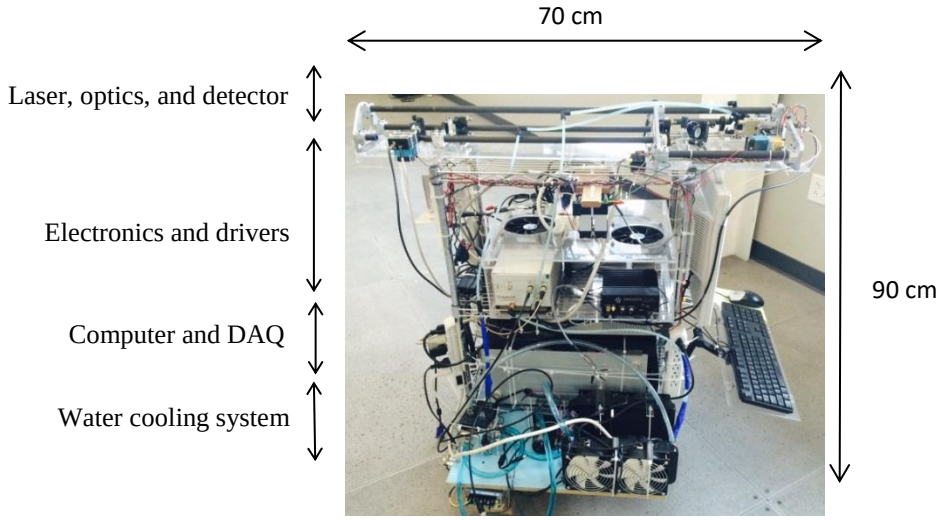

Figure 3.10: The developed open-path CRDS based ammonia sensor.

3.3.2.2– Cavity alignment

The success of a sensitive and reliable gas spectrum measurement in a CRDS experiment depends crucially on a correct alignment of the mirrors forming the cavity. In order to exciting just the fundamental TEM_{00} modes of the cavity, two plano-convex germanium lenses with 50 mm and 75 mm focal lengths were used. The position of these lenses are calculated based on series of equation obtained from ABCD theory and the fact that beam curvature on the curved side of the mirrors

should match the mirror curvature[46,47]. The radius of curvature of the mirrors is 1 m. It was chosen to roughly minimize the needed mode-match distances. For these curvatures, the cavity is stable for lengths up to 1 m (and also between 2 and 3 m). The basic assumption in calculating the mode-matching lenses positions is that the laser light itself is a TEM_{00} beam with M^2~1. The M^2=1.1 has been measured for our QCL.

In order to get a stable cavity by two mirrors, both of them have to be perpendicularly oriented to the laser beam (and that is why in CRDS an optical isolator is needed). Since working with a visible light remarkably reduces the complexity of mirror alignment, a He-Ne laser with a red beam (632.8 nm) is precisely overlapped on the main MIR beam. Using a flip mirror, we can use either the main beam or visible light to inject in to the cavity. The high reflectivity mirrors are made of Zinc Selenide (ZnSe) which is transparent in visible spectra. Also, the coating on the mirrors does not have any absorption in visible light such that mirrors pass the He-Ne beam. The mirrors orientation can change finely by two nubs. First the rear mirror (close to detector) is aligned such that while the visible light is hitting the center of curved side of the mirror, its orientation is varied until no reflected beam from the mirror surface is seen. The same procedure is repeated for the front mirror (close to laser). If the beam is precisely on the mirror centers and the lenses are located in their precalculated positions, the TEM_{00} will be the only modes excited by the laser beam. Figure 3.12 shows a typical signal acquired form TEM_{00} modes.

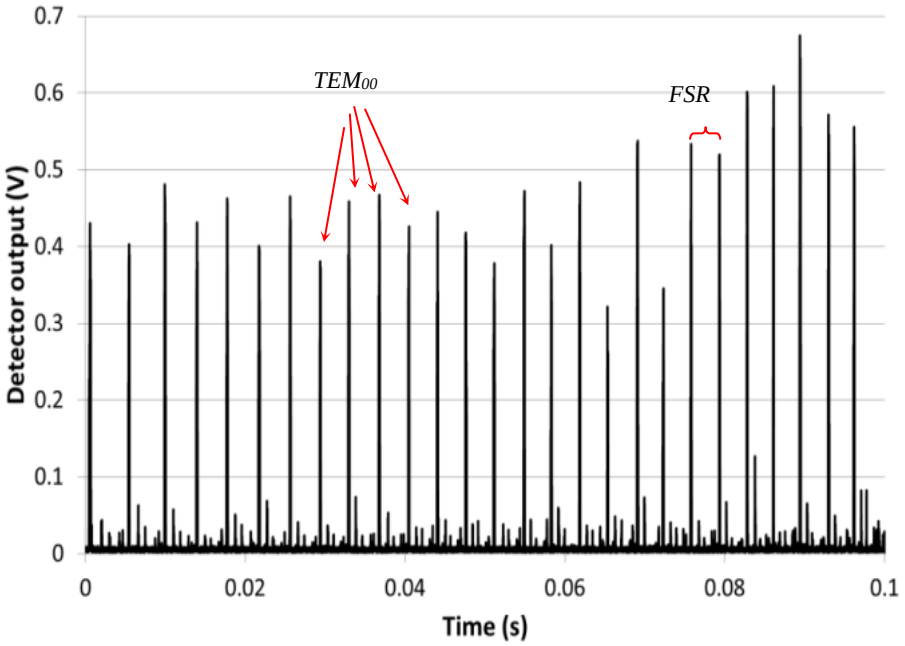

Figure 3.11: Recorded cavity mode spectra by tuning the laser wavelength by about 0.4 cm^{-1} (12 GHz) with a frequency of 10 Hz.

3.3.2.3– Mirror reflectivity measurements

In order to measure mirrors reflectivity, ring-downs are measured in a closed path configuration. Pure nitrogen with high flow rate is flowing into the cavity to avoid any absorption which leads to ringdown variations. The analysis of the ringdown event is based on a Levenberg-Marquardt nonlinear least squares algorithm. Figure 3.12 shows the ringdown data and fitted exponential decay.

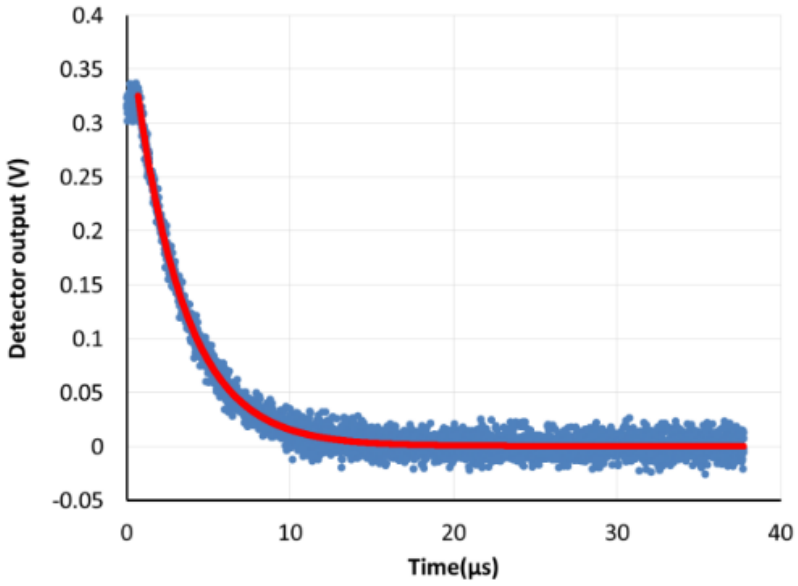

Figure 3.12: A typical ring-down measurement. Red curve is the exponential fit. Blue dots are detector output.

The measured ringdown in this configuration is 3.3 μs. Assuming no absorption inside the cell, mirror reflectivity can be obtained via $R=1-l/c\tau$ =0.9995 for a cavity length of 50 cm. Although typical mirror reflectivity in near infrared spectra for a CRDS setup is 0.9999 (corresponding to τ ~17 μs for 50 cm of cavity length), reflectivity in the MIR has not yet been developed to such high levels. Different materials and layer designs are used in the various spectral regions with challenges including the need to minimize absorption in the layers. To our knowledge, the mirror reflectivity measured in this study is the highest reported in the 9-11 μm region. Past research at 8.5 μm has shown R=0.9995[59] while other published work in the 9-11 μm region has shown, for example, R=0.998 at 10.9 μm[60] , R=0.9992 at 9.67 μm[35], and R=0.998 at 10.6 μm[37] (Note that Rayleigh scattering loss should also be subtracted but it is negligible relative to mirror loss for the present conditions).

3.3.2.4 – Ammonia measurements and sensor sensitivity

By tuning the laser wavelength over the ammonia spectra, ringdown measurements can be converted to absorption:

$$\alpha(v) = \frac{1}{c\,\tau(v)} - \frac{1-R}{l} = \frac{1}{c\,\tau(v)} + b \tag{3.17}$$

Ammonia concentrations are determined by fitting the measured absorption (loss) spectrum with a synthetic spectrum. For the elevated pressures of interest (~1 atm), the Voigt profiles are well approximated by simple Lorentzian profiles. (The difference between Lorentzian and Voigt profiles for the conditions of Figure 3.8 is $<10^{-10}$ cm^{-1}, which is well below the detection limit of the sensor.) To fully capture the spectral shape in the targeted region, six absorption lines of ammonia, one absorption line of carbon dioxide, and one absorption line of water are included in synthetic spectrum:

$$\alpha(v) = b + \sum_{\mathrm{j}=1}^{3} N_j \sum_{\mathrm{i}} \varphi_{Lor}\left(v, v_{0i,j}, \Delta v_{i,j}\right) S_{i,j} \tag{3.18}$$

where b is the cavity baseline loss (in of cm^{-1}, nominally equal to (1-R)/l, where R is the mirror reflectivity and l is the cavity length, and assumed to be constant over the measurement region), j is an index for summing over species, N_j is the number density of molecules of species j (in molecule/cm^3), i is an index for summing over lines for a given species, φ_{Lor} is a Lorentzian lineshapes (in cm) with center frequency $v_{0i,j}$ (in cm^{-1}) and width $\Delta v_{i,j}$ (in cm^{-1}), and $S_{i,j}$ is the linestrength (in cm/molecule) for species j and line i. The fit has 5 free parameters which are the baseline offset, frequency offset (since we measure only relative laser frequency in the experiment), and ammonia, water, and carbon dioxide densities. The fidelity of the fitting approach has been confirmed by simulating all lines in the region and then retrieving the starting ammonia

concentration by fitting with equation 3.17 (fitted densities for water and carbon dioxide are not precise since we only scan the wings of those features, but their inclusion is needed to accurately determine ammonia density). The ammonia density is finally converted to concentration (mixing ratio) using the ambient pressure and temperature via the ideal gas law: $C=N_{NH3}RT/PN_A$ where R, T, P, N_A are gas constant, temperature, pressure, and Avogadro's number respectively.

Absorption spectra have been collected with CRDS sensor at various locations and conditions. Figure 3.13 shows a typical loss (absorption) spectrum recorded by the open-path CRDS sensor in our laboratory. The data corresponds to 1 second of integration time and the resulting ammonia concentration is 18 ppb. The spectrum shows the ability to measure relatively low concentrations, including ambient levels of ~20 ppb (far from sources) and seeing increases due to ammonia emitted from human skin when one's hand is placed near the cavity[61]. In recent work using open-path NIR CRDS, aerosol induced loss (ring-down time) fluctuations have been observed[62]; however such fluctuations typically have optical extinction of ~10^{-9} cm^{-1} and are not seen here given the poorer optical sensitivity of this sensor, due primarily to the lower R mirrors[63,64].

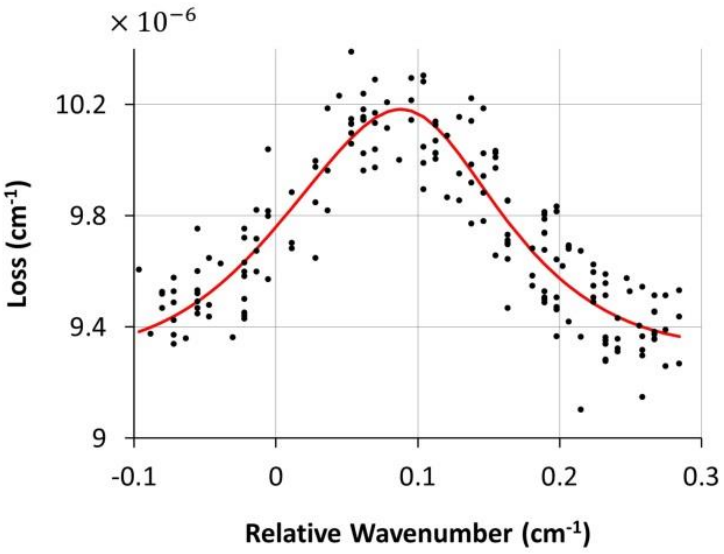

Figure 3.13: Example of CRDS absorption spectrum for 1 s integration time. The red line is a fit with the synthetic spectrum (equation 3.17) yielding [NH_3]=18 ppb.

For a given CRDS setup, the noise and uncertainty in ringdown measurements determines the sensitivity of the system. For statistically independent Gaussian distributed signals, averaging over time can reduce the noise since the variance of ensemble decreases as 1/*t*. However, the ensemble variance will not vanish if one averages the measurements for infinite amount of time. Eventually, the system drift will dominate and averaging will increase the variance. Allan variance method determines the maximum (optimized) time for collecting and averaging data [65]. Allan variance studies were performed to examine the instrument precision and effect of varying the integration times between concentration fits. The left of Figure 3.14 shows an Allan variance study with raw data of open-path ringdown times obtained by scanning the laser frequency over a narrow (spectrally flat) region at 967.15 cm^{-1}. The measurements were made in open laboratory air in Fort Collins, Colorado. The Allan variances are computed using the modified method outlined by Huang and Lehmann[66]. The minimum of Allan variance is 0.009 μs which occurs at an integration time of ~2–4 s, with the decreasing portion of the curve having a best-fit slope of −0.41. The

baseline ring-down time for our experiment is ~3.3 μs resulting in a sensitivity of $k = 4 \times 10^{-8}\text{cm}^{-1}$ (in 1 second)[54] which is equivalent to ammonia concentration sensitivity of ~0.8 ppb in 1 s (based on the peak value of the targeted absorption feature, i.e. figure 3.8). A similar Allan variance study was performed for closed-path operation and we find minimum of ~0.002 μs at time ~10 s, with a slope of −0.45 (in the decreasing portion) as expected for white noise[65]. The different slope for open-path along with higher variance values is thought to be primarily due to true changes in ambient ammonia and water concentration in the room (note that an ammonia concentration change in 2 ppb corresponds to a change in ring-down time of ~0.01 μs at the laser frequency used). It is possible that atmospheric turbulence-induced beam steering also contributes. Open-path variance studies at controlled conditions are difficult, and these issues require further investigation, but the reported sensitivity of ~1 ppb is very satisfactory for our application. Note that if the true open-path Allan variation (in the absence of actual ammonia variations) was the same as for closed path, then the concentration sensitivity would be considerably better than what we report.

The right of Figure 3.14 shows similar open-path Allan variance study, with raw data, for ammonia concentration recorded in the same laboratory. The mean ammonia concentration over the measurement was 20.8 ppb and again the true ammonia fluctuations can impact the data. Our final reported concentration sensitivities are from these studies which yield ~0.6 ppb (1-σ), or equivalently 1.2 ppb (2-σ), for 3-s measurement duration—these values are quite consistent with those inferred from ring-down times above. As with other reported Allan variance studies for concentration[58,67], the resulting curve does not follow a simple behavior of monotonic decrease to a single minimum. Allan variance study of concentration for closed path was also performed and is generally similar but with about three times the lower variance values for a given time.

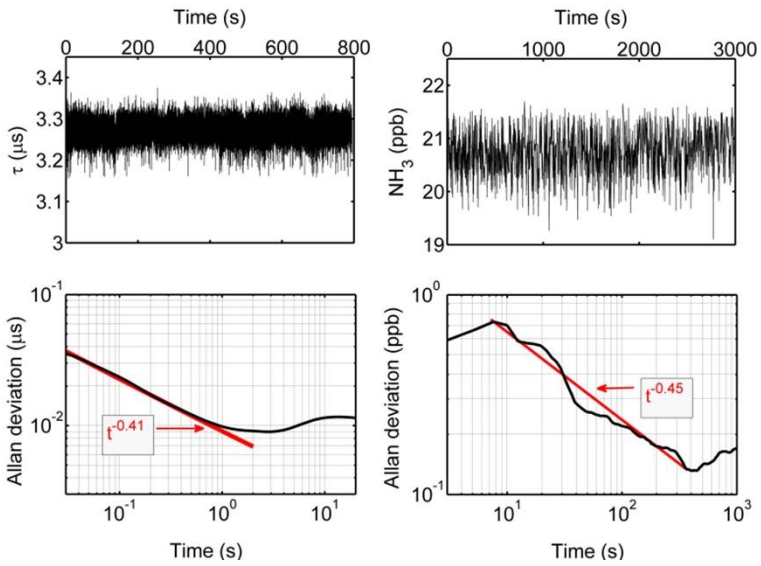

Figure 3.14: Allan variance studies of ring-down time variation (left) and concentration (right) for open-path CRDS. Top panels show raw data with bottom panels showing Allan variance studies. For the ringdown time studies, the laser is scanned over a flat region around 967.15 cm^{-1}.

3.3.2.5 – Ammonia validation data

Sensor accuracy was tested by applying known concentrations of ammonia in a closed-path configuration at atmospheric pressure and room temperature. Zero-air and ammonia gas from two reference cylinders were mixed and passed through a 50 cm Teflon sample line into a stainless-steel flow cell that formed the optical cavity. Figure 3.15 shows the results of comparison between expected and measured concentrations. Each plotted point is a 5 minute average (corresponding to the average of ~300 concentration fit measurements). The concentrations were sequentially decreased, and at each new concentration we waited 10 minutes for the recorded concentration to stabilize due to adsorption effects. No special measures were taken to heat the sample lines or cells as is sometimes done in closed-path instruments [35]. The error bars for expected concentration are due to combining 2% uncertainty in the reference cylinder mixture concentration and 4% of full scale uncertainty of the flow meters. The error bars on measured concentration are taken as the standard deviation of individual concentration measurements and are negligibly small on the

displayed scale. The measurements are in good agreement with a linear fit yielding a slope of 0.989 and R^2=0.999. The very small discrepancy observed at 50 ppb expected concentration may be due to adsorption and memory effects from the inlet and sampling lines.

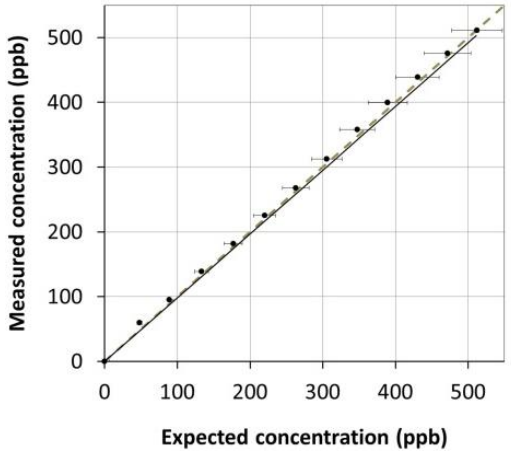

Figure 3.15: Comparison between measured and expected NH_3 concentrations for measurements from reference gas cylinders taken in a closed-path configuration. The dashed line shows the 1:1 trend line and the solid line shows the linear fit.

We have performed an initial field study using the open-path sensor at a cattle feedlot at the Colorado State University Agricultural Research Development and Education Center (ARDEC, 40˚65́ N, 104˚99́ W) in northern Colorado with a cattle population of ~400 head.

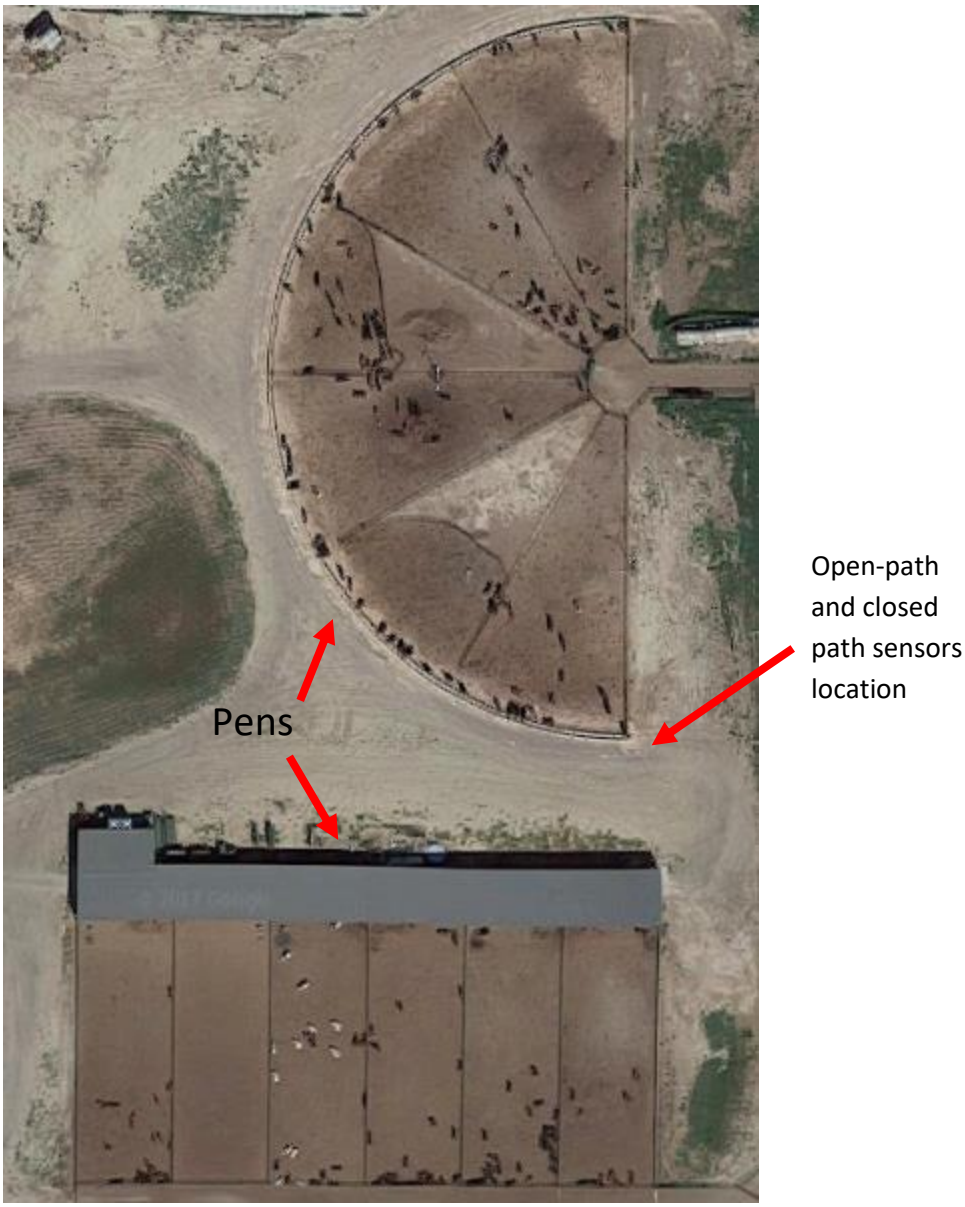

Figure 3.16: The aerial view of the location of two sensors nearby cattle at ARDEC, northern Colorado.

The sensor was tested during different days in February 2016 for several hours each day. During these tests we did not employ any measures to maintain mirror cleanliness but, over the relatively short durations of these tests, no measurable reduction of the ring-down time was observed. Future configurations will employ a purge-enclosure around each mirror to protect the mirrors. The open-path sensor was validated against a co-located commercial closed-path CRDS ammonia sensor

(Picarro Inc. G2103). The sampling inlet of the commercial sensor was approximately 40 cm from the open-path cavity. Figure 3.17 shows data collected from both sensors where data from both was adjusted to 3 second time steps with adjacent averaging.

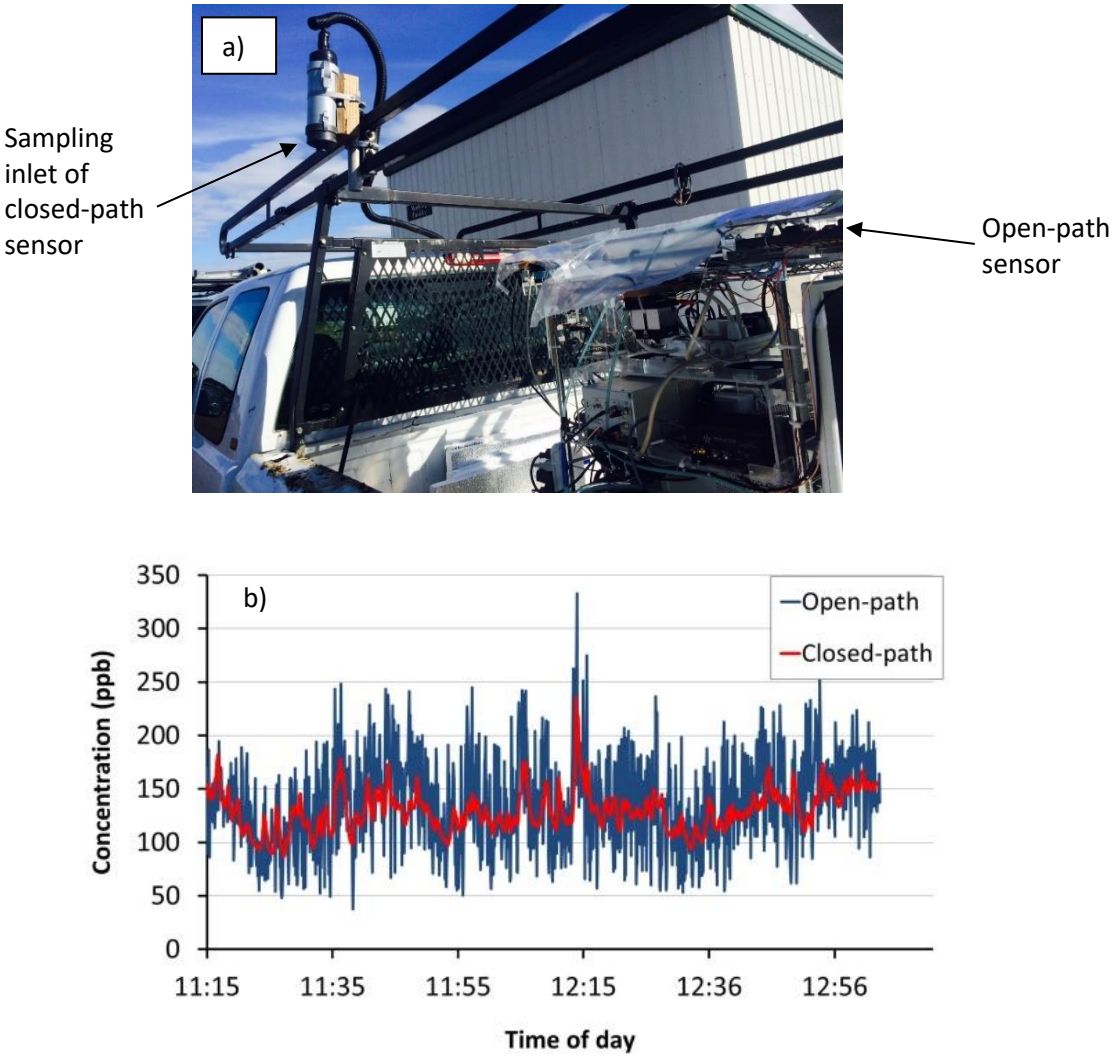

Figure 3.17: a) Co-located open-path and closed-path sensors at a feedlot b) Comparison between NH_3 concentrations recorded by two CRDS sensors.

Figure 3.18 shows the correlation between ammonia concentrations recorded by the open-path and commercial closed-path CRDS sensors for 2 hours of data collection. Both datasets were averaged to 5 minute time steps. At this time resolution, the measurements are in good agreement with a

linear fit yielding a slope of 0.990 with intercept of 1.7 ppb (R^2=0.92). A similar comparison of ammonia plume measurements between open-path laser absorption and a commercial closed-path CRDS analyzer has been reported by Sun et al.[68]. As is the case in our data comparison (Figure 3.17), the open-path analyzer tended to capture more dynamic behavior, i.e. higher and lower readings as concentrations are changing, while the closed-path analyzer showed a flatter response (even when the data were averaged to give matching time steps). Future studies should examine open-path CRDS measurements for different atmospheric (particle) conditions, ideally also via comparison with other open-path sensors.

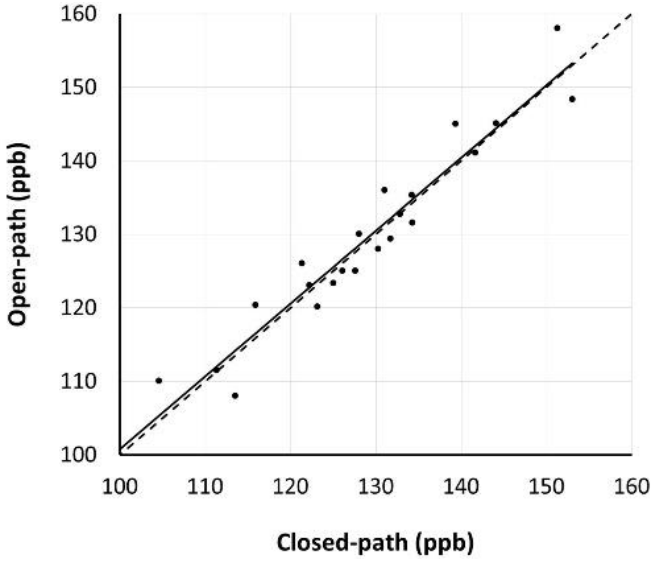

Figure 3.18: Correlation between NH_3 concentrations recorded at a feedlot by open-path and commercial closed-path CRDS sensors. Both datasets were averaged to 5 minutes. The dashed line shows the 1:1 trend line.

Chapter 4: Development of Open-Path WMS sensor

As it was mentioned earlier, the electro-optical setup of WMS technique is more simple than CRDS and this makes it a good option for aerial measurements using UAS. In this chapter, first the WMS technique is discussed. Next, the design of a multipass cell to enhance the detection sensitivity is presented. Finally, the development and performance of the compact open-path sensor is described.

4.1 - WMS technique

WMS was first introduced by Cameron et al in 1987[69]. However, they just emphasized on theoretical description with little experimental results for sample detection. In 2001, Kluczynski et al. described WMS in terms of a new formalism based on Fourier series[70]. Since that time several studies have shown the application of WMS for atmospheric species detection[42,71,72].

The optical setup for a WMS based sensor is the same as for a direct absorption spectroscopy based one: a beam of a tunable monochromatic laser is sent through a gas sample and the transmitted intensity is measured with a detector. However, the difference between these techniques is how the laser is tuned over the absorption feature and how the acquired data is analyzed by the detector.

4.1.1 – Phase Sensitive Detection and Lock-in Amplifiers

Lock-in amplifier is one of the basic components in a WMS system. Generally, it is used to detect signals in noisy environments. The lock-in amplifier is basically a multiplier and a lowpass filter at the output. The target signal is modulated at a certain frequency and then multiplied by a reference wave. Finally, the multiplication is passed through the lowpass filter.

Consider a modulated signal as $V_{sig}\sin(\omega t+\varphi_{sig})$, i.e. the amplitude of V_{sig} at frequency $\omega/2\pi$ and phase φ_{sig}. If the frequency of the reference wavefunction is chosen as the same signal frequency ($V_{ref}\sin(\omega t+\varphi_{ref})$), the multiplication of the signal and the reference will have the following form:

$$V_{sig}V_{ref}\sin(\omega t+\varphi_{sig})\sin(\omega t+\varphi_{ref})=$$
$$\frac{V_{sig}V_{ref}}{2}\left[\cos(\varphi_{sig}-\varphi_{ref})-\cos(2\omega t+\varphi_{ref}+\varphi_{sig})\right] \quad (4.1)$$

The time independent term (first term in the second line) is the output of the lock-in amplifier and is obtained by passing the multiplication through the low-pass filter.

$$V_{LIF}=\frac{1}{\tau}\int_0^{\tau}\frac{V_{sig}V_{ref}}{2}\left[\cos(\varphi_{sig}-\varphi_{ref})-\cos(2\omega t+\varphi_{ref}+\varphi_{sig})\right]\mathrm{d}t=$$
$$\frac{V_{sig}V_{ref}}{2}\cos(\varphi_{sig}-\varphi_{ref})+\frac{V_{sig}V_{ref}}{2}\frac{1}{\tau}\int_0^{\tau}\cos(2\omega t+\varphi_{ref}+\varphi_{sig})\ \mathrm{d}t=$$
$$\frac{V_{sig}V_{ref}}{2}\cos(\varphi_{sig}-\varphi_{ref}) \quad (4.2)$$

Where $1/\tau$ is the bandwidth (BW) of the lowpass filter and should satisfy the condition $BW \ll \omega$ to vanish the second term in second line of equation (4.2). The time independent term (DC component) of this equation is output of the lock-in amplifier. Note that, if the frequencies of the signal and the reference are different, both terms in the second line of equation 4.2 will be time dependent with no DC component. Thus, the output of the lock-in will be zero. This is useful in a noisy environment including several frequencies since the lock-in will be sensitive only to those components that have the same frequency of the reference wave.

Although the equation 4.2 is a DC value, it is dependent on the phase difference between the main and reference signals ($\varphi_{sig} - \varphi_{ref}$). This makes the results not practical if the phase difference is unknown. One way to make the results independent of the phase difference is the phase-insensitive approach. This can be conducted by passing the signal in parallel through two lock-in amplifiers. One lock-in multiplies the signal by a sine wave (and we call it the *Y* component of the signal) while the other one multiplies by a cosine wave (and we call it the *X* component of the signal).

$$\begin{cases} V_{ref}^{Y} \sin(\omega t + \varphi_{ref}) \\ V_{ref}^{X} \cos(\omega t + \varphi_{ref}) \end{cases} \tag{4.3}$$

The output of the two lock-ins are expressed:

$$\begin{cases} DC^{Y} = \frac{1}{2} V_{sig} V_{ref} \cos(\varphi_{sig} - \varphi_{ref}) \\ DC^{X} = -\frac{1}{2} V_{sig} V_{ref} \sin(\varphi_{sig} - \varphi_{ref}) \end{cases} \tag{4.4}$$

Based on the trigonometric identity $\sin^2(\theta) + \cos^2(\theta) = 1$, the root-sum-square of the *X* and *Y* components becomes independent of the phase difference:

$$R = \sqrt{(DC^{Y})^2 + (DC^{X})^2} = \frac{V_{sig} V_{ref}}{2} \tag{4.5}$$

Therefore, using two parallel lock-ins makes the results independent of the phase difference and just by knowing the amplitude of the reference waves, the main signal can be measured ($V_{sig} = 2R/V_{ref}$)[73].

4.1.2 – Theory of WMS

The basic method involves a similar idea to direct absorption spectroscopy. As it was discussed earlier, in a DAS system, the laser wavelength is linearly tuned over the absorption feature of the target species with the typical scanning rate of 1-100 Hz. One of the drawbacks of this simple technique is that its sensitivity is limited by low frequency noise in the signal, which originates mainly from the laser and detector noise. Also, in open-path configuration with atmospheric pressure, the absorption features are not isolated and determining the background signal (the detector signal without absorption) is challenging[72,74].

WMS can reach higher sensitivity while the optical setup is as simple as DAS (i.e. opposed to CRDS, devices such as AOM and optical isolators are not needed). It has been increasingly applied for measurements in harsh environments due to its improved sensitivity and noise-rejection capabilities over direct absorption. In a WMS system, the laser wavelength is tuned with a high frequency such that the flicker (1/f) noise in the system is reduced. The noise rejection mechanism provides better sensitivity. WMS is also a "derivative" technique which is sensitive to spectral absorption shape or curvature rather than absolute absorption levels. This is particularly helpful for measurements in atmospheric pressure with non-isolated absorption features. Another advantage of WMS is its independence from the background signal. The most challenging drawback of WMS is the complex math and data analysis for concentration measurement[72].

In WMS, while the laser wavelength is slowly linearly (1-100 Hz) tuned over the absorption feature, it is also modulated rapidly at high frequency which is typically 10 kHz. (i.e. the current/frequency modulation is the superposition of two slow sawtooth and fast sinusoidal

waves). Both slow and fast modulations can be performed by varying the injection current into the laser which takes the following form:

$$i[\text{mA}] = i_0 + i_S S(ft) + i_F \sin(2\pi F t) \tag{4.6}$$

Where i_0 is the DC current and $S(ft)$ represents the slow sawtooth signal with frequency f and amplitude i_S. In fact, the first two terms (DC+sawtooth) are the same used in a DAS system and the third term is added in a WMS system. The parameters i_F and F are the amplitude and frequency of the sinusoidal current modulation, respectively. The sinusoidal frequency should be much higher than slow scan frequency (1-100 Hz) and much lower than width of target absorption feature (~15 GHz).

The input injection current into a diode laser leads to the laser frequency (wavenumber) variation. For one sawtooth period ($0 \leq t \leq 1/f$), the laser frequency variation takes the form below[75]:

$$v[\text{cm}^{-1}] = v_0 + \eta_S i_S f t + \eta_F i_F \sin(2\pi F t + \emptyset) \tag{4.7}$$

Where η_S and η_F are the slow and fast frequency scanning rates (cm^{-1}/mA). The parameter $\emptyset$ is the phase difference between the current and frequency variations. In diode lasers, increasing the injected current causes a decrease in the laser frequency. The phase difference $\emptyset$ (which is $\sim\pi$) represents such a decrease (increase) when the current increases (decreases)[76]. In WMS, measuring the exact values of $\emptyset$ and η_F are crucial and they need to be characterized for each laser. Figure 4.1 shows a schematic of how the laser current is tuned over the absorption feature. In one slow scan, the high-frequency wavelength modulation causes the laser to scan back-and-forth over part of the absorption feature twice per modulation cycle (since it is sinusoidal). The shape of transmitted laser intensity is affected by the sample absorption.

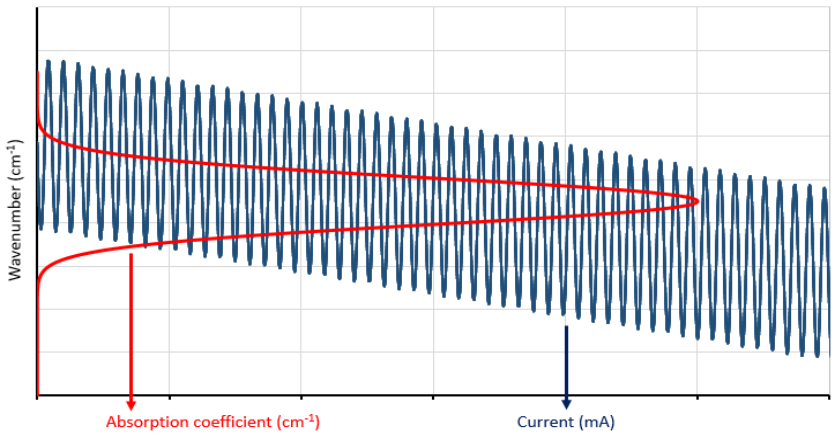

Figure 4.1: Schematic of the laser current tuning (blue) over absorption profile (red) in one period of the slow scanning (sawtooth).

The interaction between rapidly modulating wavelength and nonlinear absorption feature (Beer-Lambert law) gives rise to harmonic components in the detector signal. Different harmonics of modulation frequency (nF , $n = 1,2,3, \ldots$) are then isolated with lock-in amplifiers. Figure 4.2 shows a schematic of a WMS based system[72].

Figure 4.2: Schematic of a typical WMS system

The detector output signal is passed to several lock-in amplifiers to isolate the harmonics of interest (each lock-in can be used for one harmonic). The lock-in amplifier multiplies the detector signal by a reference sinusoid at the desired frequency ($1F$ or $2F$). The low pass filter then extracts the DC component of the multiplication (Detector signal × Reference) and eliminates all components outside of the filter bandwidth.

The fractional transmission (I/I_0) of the sample obeys the Beer-Lambert law and with the sinusoidal term, it can be expressed in Fourier series[72,77]:

$$\frac{I_0}{I} = e^{-\alpha(v_0 + a\cos(\omega t))l} = \sum_{k=0}^{\infty} H_k(a, v_0)\cos(k\omega t) \tag{4.8}$$

Where, $\omega = 2\pi F$, v_0 is the laser frequency without modulation and the coefficient $a = \eta_f i_f$ is defined as the modulation depth. The functions $H_k(a, v_0)$ are given by:

$$H_k(v_0, a) = \frac{1}{(1 + \delta_{0,k})\pi} \int_{-\pi}^{\pi} e^{-\alpha(v_0 + a\cos(\theta))l} \cos(k\theta)\, \mathrm{d}\theta \tag{4.9}$$

Where $\delta_{0,k}$ is the Khronecker delta.

Considering the synchronous intensity and wavelength modulation, the laser transmitted intensity can be written as:

$$I(t) = I_0(t)e^{-\alpha(v_0 + a\cos(\omega t))l} = \overline{I_0}(1 + i\cos(\omega t + \varphi)) \times \sum_{k=0}^{\infty} H_k(a, v_0)\cos(k\omega t) \tag{4.10}$$

In equation above, $\overline{I_0}$ is the laser intensity in absence of absorption and without modulation and $I(t)$ is the incident light intensity on the detector active area. The lock-in amplifier multiplies the detector output with either a sin or cos function as the reference with the harmonic frequency of interest. If the reference signal is a sin wave, the n^{th} harmonic output of the lock-in amplifier is the DC component of $I(t) \times \sin(n\omega t)$. For such a case with a sin reference signal, the DC term can be obtained as below:

$$X_{nF} = \frac{1}{2} G\overline{I_0} \left[H_n + \frac{1}{2}(H_{n+1} + (1 + \delta_{1n})H_{|n-1|})i\cos(\varphi) \right] \tag{4.11}$$

Where, G is the detector gain.

If the reference signal is a cos, then the lock-in output will be:

$$Y_{nF} = \frac{1}{2} G \bar{I_0} \left[\frac{1}{2} (H_{n+1} - (1 + \delta_{1n}) H_{|n-1|}) i \sin(\varphi) \right] \quad (4.12)$$

In case of having two parallel lock-ins, the root-sum-square of *X* and *Y* components is used to cancel the phase shift between the detector signal and lock-ins (section 4.1.1)[72,77].

$$R_{nF} = \sqrt{X_{nF}^2 + Y_{nF}^2} \quad (4.13)$$

Among different harmonics, the second one (R_{2F}) has the strongest dependency on spectral parameters and gas properties. The sample concentration is calculated by comparing the acquired data from the lock-in with spectral simulation. However, different harmonics, including second one, are dependent on the electro-optical gain of the detector too (and not only the gas properties). Such a dependency is an important drawback of WMS technique since it requires measurement calibration with a known gas mixture to infer absolute concentration. One method to cancel the effect of detector gain and laser intensity variation is normalizing the second harmonic (R_{2F}) to the first harmonic (R_{1F}) since the intensity modulation is the strongest component of R_{1F}. Figure 4.3 shows a schematic of the modulated laser beam as well as the second and first harmonics and their ratio. The $1F$ normalization accounts for the perturbations in laser intensity present in harsh environments (e.g. being directly exposed to the sun, the variation of temperature and pressure especially for open-path sensors, and the presence of dust and particles in the measurement region). Also, the $1F$ normalization method makes WMS a calibration free techniques since the $2F/1F$ signal can be directly compared to the simulated model without the laser intensity variations.

There are two major sources of background signal which can cause non-zero $2F$ signal in absence of absorption including the etalon and nonlinear intensity modulation effects. The etalon effect is caused by constructive/destructive interference arising from parallel surfaces in the optical path. This effect should be avoided because it is strongly affected by temperature variation (which is very common in harsh environments) and make the background $2F$ signal unstable. The effect of nonlinear intensity can be subtracted from the WMS signal. Otherwise, the relationship between $2F$ signal and sample concentration is not linear. In order to remove background from $\left(\frac{2F}{1F}\right)$ signal, the measured $2F$ and background must be normalized to $1F$ signal and then vector subtracted[72]:

$$\left(\frac{2F}{1F}\right)_{bg\ subtracted} = \sqrt{\left[\left(\frac{X_{2F}}{R_{1F}}\right)_{data+bg} - \left(\frac{X_{2F}}{R_{1F}}\right)_{bg}\right]^2 + \left[\left(\frac{Y_{2F}}{R_{1F}}\right)_{data+bg} - \left(\frac{Y_{2F}}{R_{1F}}\right)_{bg}\right]^2} \qquad (4.14)$$

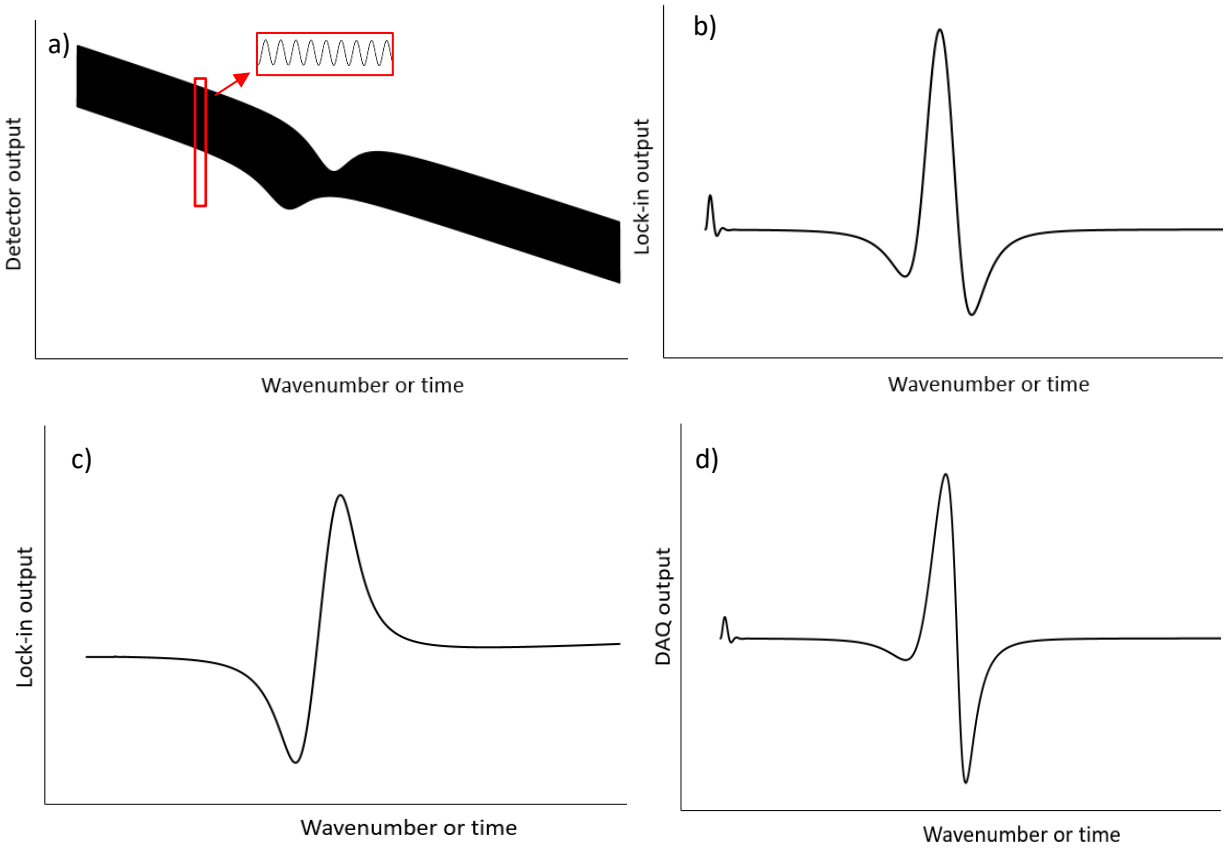

Figure 4.3: Schematic of WMS signals. a) The absorption dip in a WMS system with fast and slow modulations (detector output). b) Second harmonic of absorption, X_{2F} (lock-in output). c) First harmonic of absorption, X_{1F} (lock-in output). d) The ratio of second and first harmonics, X_{2F}/X_{1F} (DAQ output).

4.1.3 – Numerical WMS model

In order to infer the sample concentration, it is important to have a simulated model of the first and second harmonics. One way to simulate the R_{2F} and R_{1F} signals is analytic derivations from the Fourier series (equation 4.8), however such derivations demands several complicated integrals which makes the method computationally expensive[75,78]. Alternatively, a numerical model can be developed to simulate the lock-in amplifier signal outputs. In this research, the latter method has been used. To simulate the lock-in output, several parameters in equations 4.6 and 4.7 should be empirically measured. The frequency variation due to injection current need to be characterized. This characterization includes determining the slow and fast tuning rates (η_S, η_F) as well as the

phase difference between current (intensity) and frequency variations (∅). As discussed in section 2.2.2, the combination of an etalon (with certain values of *n* and *d*) and a reference cell can be used for laser characterization. In low modulation frequencies, the phase shift ∅ is equal to π [76]. However, in higher ranges (~kHz) it is not exactly π and can increase with modulation frequency. Also, the tuning rate of the laser depends on the frequency modulation. So, for each specific frequency modulation the phase shift and tuning rate should be measured.

Equation 2.11 describes the beam intensity after passing through an etalon.

$$I = I_0 \frac{1}{1 + \frac{4R}{(1-R)^2}(\sin(\frac{2\pi n d}{\lambda}))^2} \tag{2.11}$$

When the laser frequency (wavelength) and intensity are tuned by the fast current modulation with frequency F and amplitude i_F, the etalon transmission will be expressed as below:

$$I = \frac{I_0 + I_F \cos(2\pi F t)}{1 + \frac{4R}{(1-R)^2}\left[\sin\left(2n\pi d \times (v_0 + v_F \cos(2\pi F t + \emptyset))\right)\right]^2} =$$

$$\frac{I_0 + I_F \cos(2\pi F t)}{1 + \mathcal{F}\left[\sin\left(\frac{\pi}{FSR} v_F \cos(2\pi F t + \emptyset) + \xi\right)\right]^2} \tag{4.15}$$

Where $\mathcal{F} = \frac{4R}{(1-R)^2}$, $FSR = \frac{1}{2nd}$, and $\xi = 2n\pi d v_0$.

The unknown variables $v_F (= \eta_F i_F)$ and ∅ can be determined by fitting the etalon transmission with the function above while they are considered as free parameters. The amplitude of the $2F$ signal depends on the parameter v_F (laser frequency modulation amplitude). Studies have shown the $2F$ signal has a peak when $v_F/\Delta v = 2.2$, where Δv is half width at half maximum (HWHM) of the target absorption feature.

The other parameters such as $\mathcal{F}$ and ξ are directly measurable; however, they can be considered as free parameters too. The laser intensity (I_0 , I_F) in absence of the etalon can be quantified by fitting a sinusoidal function to the detector output when the laser is modulated.

To have a reliable WMS simulation, the relationship between optical power and injection current should be known too. This can be provided by the laser vendor or directly measured. The laser optical power and injection current are in-phase variables and they can be expressed as a function of each other. As the first order of approximation this relationship can be written as:

$$I(i) = ai + b \tag{4.16}$$

Where I (in mW) and i (in mA) are optical power and injection current, respectively. The coefficients a and b can be easily retrieved by linearly fitting the laser current and power. Having the laser output power, the detector output signal can be modeled as:

$$D(t) = GI(t)e^{-\alpha\left(N\times S\times\varphi\left(v(t)\right)\right)l} \tag{4.17}$$

here N and S are the number density and linestrength of target species, respectively. G is the detector gain and it does not need to be known since in $2F/1F$ analysis, it will be cancelled.

The lock-in amplifiers can be modeled by combination of four sine and cosine waves as the reference signals (two for first X-Y harmonic and two for second X-Y harmonic) and four low pass filters:

$$\begin{cases} \sin(1\times 2\pi Ft + \Theta) \\ \cos(1\times 2\pi Ft + \Theta) \\ \sin(2\times 2\pi Ft + \Theta) \\ \cos(2\times 2\pi Ft + \Theta) \end{cases} \tag{4.18}$$

The DC component equivalent to the X and Y component of n^{th} harmonic is simulated by multiplication of detector signal and the references which pass through the lock-in amplifiers.

The underlying assumption for this numerical simulation is that all time varying signals satisfy the Nyquist sampling theorem, i.e. the time spacing Δt should be $< {}^{1}/_{2F}$[75].

Figure 4.4 shows an example of simulated WMS signals of ammonia, water and carbon dioxide at 10.33 µm wavelength range.

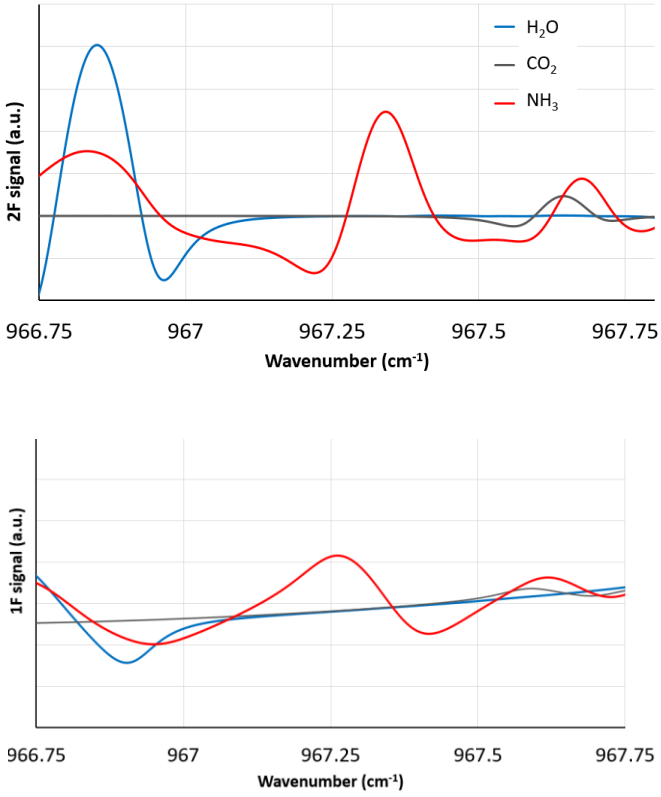

Figure 4.4: The X component of $2F$ and $1F$ signals of ammonia, water and carbon dioxide. (F= 10 kHz, $v_F = 0.1\ \mathrm{cm}^{-1}$, $\emptyset = \pi$)

4.2 – Optical multipass cell

The sensitivity of WMS is not enough to measure most trace species. A long optical path between the laser and the detector is needed to improve the detection sensitivity. Multipass cells can provide a small and constant sample volume with long optical path. The long path is provided after multiple beam reflections from two[31,79] (or three[80]) opposing concave mirrors. Depending on the mirrors curvatures (focal lengths), several configurations have been utilized to design a multipass cell. Herriot cell is one of the most simple and stable cells among others. It is constructed by two spherical mirrors having the same radius of curvature. One of the mirrors has a hole by which the laser beam enters the cavity and after multiple reflections it exits with a different slope. The number of reflections and distribution of their spots depend on mirrors characteristics (focal length, distance separation, diameter), entrance ray slope, the position of the hole, and the beam diameter.

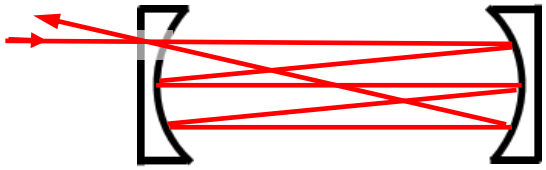

Figure 4.5: Schematic of a Herriot cell. The beam enters the cavity via the first mirror and exit from the same mirror with a different slope.

Ray optics can be used for describing the behavior of the beam during these reflections. In the cartesian coordinates, if we assume the mirrors centers are on z axis, we are interested in the intersection points (x_n , y_n) which are the coordinates of n^{th} reflection spot on the mirrors. These components can be expressed as:

$$\begin{cases} x_n = x_0\cos(n\theta) + \sqrt{\dfrac{d}{4f-d}}(x_0 + 2fx_0')\sin(n\theta) \\ y_n = y_0\cos(n\theta) + \sqrt{\dfrac{d}{4f-d}}(y_0 + 2fy_0')\sin(n\theta) \end{cases} \quad (4.18)$$

$$\theta = \cos^{-1}(1 - \frac{d}{2f}) \quad (4.19)$$

Where:

x_0 and y_0= *x* and *y* coordinates of the hole on the first mirror
x_0' and y_0'= the slope of the beam in the *x* and *y* directions
d= mirrors separation
f= mirrors focal length

In equation 4.18, it is clear that the mirrors separation is restricted to the range $0 < d < 4f$. However, the practical range for d is $0 < d < 2f$ since for $2f < d < 4f$, after few reflections the beam will diverge and finally will be clipped by the hole (since it will be bigger than the hole diameter)[81]. In this equation, the even and odd values of *n* correspond to the first and second mirrors, respectively. In general, the intersection points (x_n , y_n) lie on an ellipse. In special conditions, the elliptical pattern can be a circle:

$$x_0^2 = \frac{d}{4f-d}(y_0 + 2fy_0')^2 \quad (4.20)$$

Figure 4.6 shows the (x_n , y_n) points on the *x*-*y* plane for the case where they lie on a circle. The angle between the point (x_n , y_n) and its neighbor (x_{n+1} , y_{n+1}) on the other mirror is θ. This means the angle between two neighbor points on one mirror is 2θ (figure 4.6).

There are special conditions at which after multiple reflections the beam returns to the entrance hole and finally exit the cavity; i.e. $(x_0 , y_0)= (x_{2m} , y_{2m})$ where m is the number of reflection spots on the second mirror. Such a condition can be expressed by the following equation:

$$2m\theta = 2q\pi \quad , \quad q = 1,2,3, \ldots \tag{4.21}$$

The validity of re-entrant condition can be shown by substituting the equation 4.21 in equation 4.18: $(x_0 , y_0)= (x_{2m} , y_{2m})$.

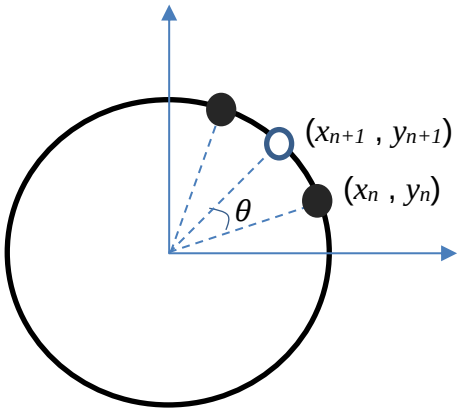

Figure 4.6: The projection of intersection points (x_n , y_n) when they lie on a circle. Black and white circles represent the beam spots on two mirrors.

The restricting factors on the number of spots are the beam, hole, and mirror diameters. In order to avoid overlapped spots and clipping the beam by the hole, the following equation must be satisfied:

$$m \leq \frac{2\pi R}{D} \tag{4.22}$$

Where R is the radial distance between the hole and the mirror centers and D is the hole diameter. Once the maximum number of spots is specified, the exact value of d/f can be calculated to make q $(= m\theta/\pi)$ an integer number such that the d value is as high as possible and the equation 4.19 is satisfied.

4.3 - Development of WMS sensor

4.3.1 - Laser characterization

The light source of the WMS sensor is the same one used in the CRDS system which covers the ammonia absorption feature at the wavelength of 10.33 μm. The laser temperature and DC+sawtooth injection current used in the WMS based sensor is the same as for the CRDS based system described in section 3.3. In order to characterize the laser beam when it is modulated with the fast frequency, the method discussed in section 4.1.3 has been used.

The laser current is tuned using a laser diode driver (Wavelength electronics, FL500) while the laser temperature is stabilized by a thermoelectric temperature controller (Meetstetter, TEC-1091). The laser beam travels through the germanium etalon with *FSR*=3 GHz. The etalon output beam is detected by the photodiode and the signal from the detector is acquired by a fast DAQ card (PCI-6351). The laser temperature and DC currents are set on 30° C and 344 mA.

Figure 4.7 shows an example of mathematical fitting of detector signal using equation 4.15 in one period of modulation. The frequency and amplitude of injection current is F=10 kHz and i_F = 12 mA. The total injection current is:

$$i[mA] = 344 + 12\cos(2\pi \times 10^4 \times t) \tag{4.23}$$

The parameters I_0 and I_F are determined by fitting the detector signal in absence of the etalon.

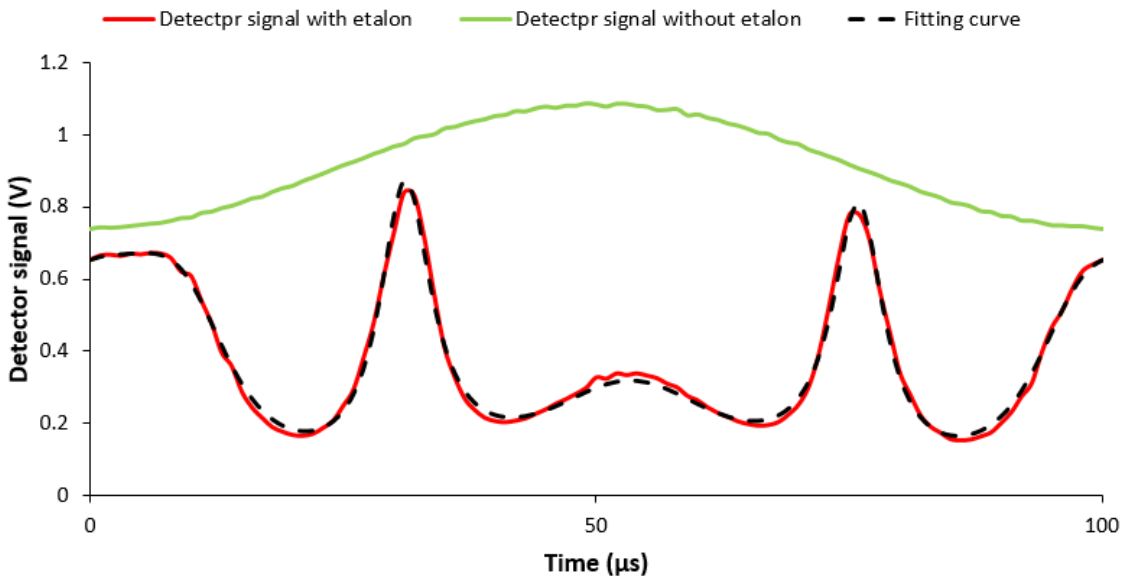

Figure 4.7: QCL characterization: experimental detector signal and the fitting curve for 10 kHz modulation frequency and 12 mA amplitude frequency.

The parameters $(\emptyset, v_F)$ retrieved by fitting are $\emptyset = 1.08\pi$ and $v_F = 0.09\ \text{cm}^{-1}$ ($\eta_F = \frac{0.09\ \text{cm}^{-1}}{12\ \text{mA}} = 0.0075\ \frac{\text{cm}^{-1}}{\text{mA}}$). It has been observed that at a fixed modulation frequency (10 kHz) the QCL tuning rate does not change in the amplitude range of 10 mA – 20 mA and the laser frequency modulation amplitude (v_F) could be determined by: $i[\text{mA}] \times 0.0075\ \frac{\text{cm}^{-1}}{\text{mA}}$. Thus, the amplitude current modulation of 20 mA is equivalent to 0.15 cm^{-1} which provides the highest peak of $2F$ signal.

4.3.2 – Experimental

4.3.2.1 – WMS setup

Figure 4.8 shows a schematic of the setup of the open-path WMS sensor. The laser beam emitted from QCL is directed in to a Herriot multipass cell using two steer mirrors. The beam size on the laser head is ~3.5 mm and it is focused to ~1.5 mm in 30 cm which happens inside the cavity. The light beam bounces back and forth inside the cavity and after 28 reflections from each mirror and travelling 19.88 m, leaves the cell.

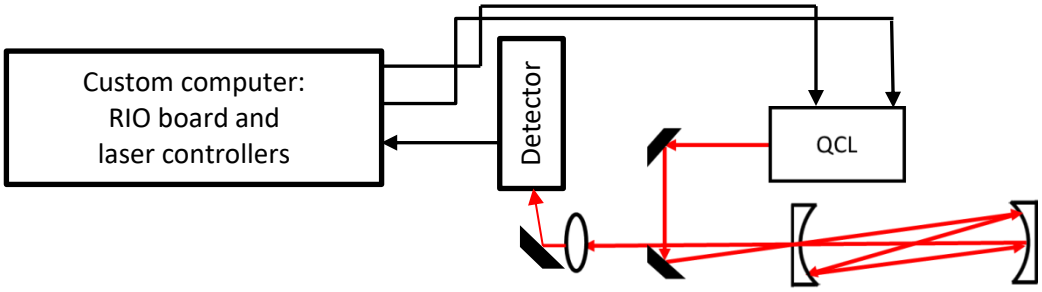

Figure 4.8: Schematic of the developed open-path WMS sensor setup. The beam is directed into the Herriot cell using two steer mirrors. The exit beam is focused by a lens on the detector active area. Digital lock-in amplifiers are used to extract the first and second harmonics.

The exiting beam is focused by a germanium lens on the optical detector (VIGO PVM-2TE-10.6) placed 3 cm from the lens. A custom electronics RIO based computer (NI) has been designed and built to control and power the electro-optic components (controllers, detector, …), as well as to acquire, analyze, and save data. The overall size and weight of the computer board are $30 \times 10 \times 5$ cm^3 and ~2 kg. It can be powered by the any input voltage in the range of 12 V to 30 V. The computer consumes ~25 W of power and a Lithium ion battery (5000 mAh, ~14 V, ~0.5 kg) can power it for ~2.5 hours. The detector data is acquired by the computer which digitizes the detector signal at a rate of 200 kHz. The laser temperature is stabilized on 30°C and the injection-current is modulated with a sine function at F= 10 kHz superposed on a linear scan with f= 100

Hz. After averaging acquired data of four cycles of slow modulation, it is simultaneously multiplied by four reference wavefunctions (equations 4.18). The multiplications of detector signal and references are passed through four identical digital low-pass filters with the bandwidth of 1 kHz. The output of low-pass filters provide the $1F$ and $2F$ signals. The ammonia concentration is inferred by comparing the measured and simulated $2F/1F$ signals at 5 Hz. The custom computer saves concentration with the absolute time stamp. Two sensors (Honeywell, PX2AM1XX001BAAAX and OMEGA, RTD-806) measure the ambient temperature and pressure. The computer includes a GPS to record the geographical position of the sensor including latitude, longitude, and altitude (which is vital for aerial measurements). The measured concentration, ambient pressure and temperature, and GPS data are saved by the computer board. The computer board is connected to the sensor through two cables. A cable is used to acquire data from the detector (white one in figure 4.9) and another one which itself has ten inner wires, powers the laser and detector (the black one in figure 4.9).

Figure 4.9 shows the developed open-path WMS sensor. In order to minimize the weight and thermal expansion effects, most mounts and physical structures are made from carbon-fiber. The overall weight and size of the sensor (excluding the custom computer) are ~2 kg and $60 \times 20 \times 15$ cm^3.

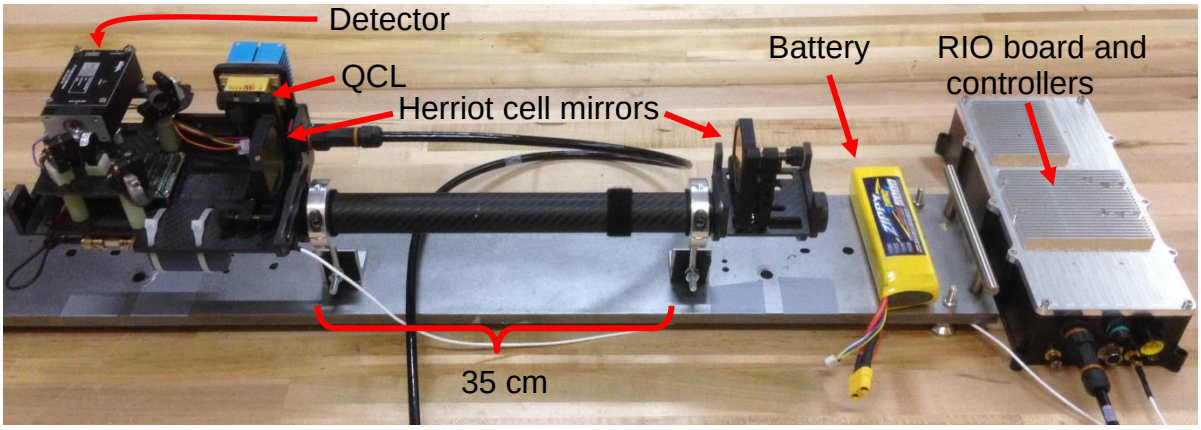

Figure 4.9: The developed open-path WMS sensor.

4.3.2.2– Cavity alignment

The optical cavity is formed from two 2'' diameter plano-concave mirrors (Thorlabs, CM508-200EH4-M02 and CM508-200-M02) with focal length of 20 *cm*. The first mirror has a 4 *mm* diameter hole located at 20 *mm* away from the mirror center. With these dimensions, the maximum number of spots on each mirror is $|40\pi/4| = 31$.

The first mirror is oriented such that the position of the hole meets the equation 4.20 and the spots on both mirrors lie on a circle with diameter of 20 *mm* (hole and mirror centers distance). A cavity length of 35.5 *cm* is chosen to satisfy the equation 4.21 such that the numbers *m* and *q* are integers: $m = 28\,, q = 13$. In these conditions, the total path-length that beam travels inside the cavity is 19.88 m. Since $d < 2f$, the beam inside the cavity is always collimated. The diverging exiting beam is focused by the lens.

Similar to CRDS sensor alignment, working with a visible light remarkably reduces the complexity of mirror alignment. A He-Ne laser with a red beam is precisely overlapped on the main MIR beam. Using a flip mirror, we can use either the main beam or visible light to inject in to the cavity.

Figure 4.10 illustrates the calculated position of the spots on second mirror as well as the experimental results using the visible light.

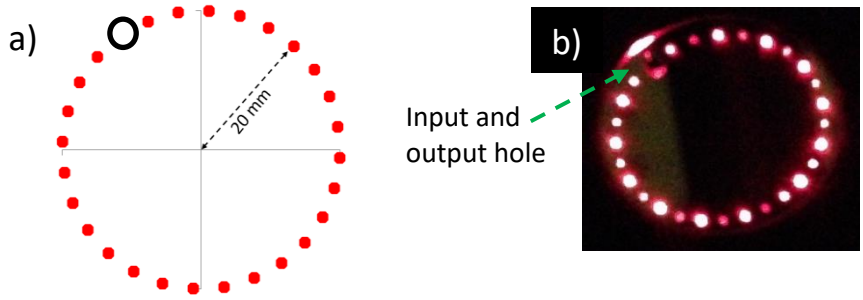

Figure 4.10: Twenty seven beam spots and the mirror hole on the front mirror of the Herriot multipass cell. a) The simulation, b) The experimental using a red beam.

4.3.2.3- Ammonia concentration measurements

The ammonia concentration is retrieved by comparing the acquired $2F/1F$ signal with the simulation spectra. The simulated $2F$ and $1F$ harmonics are obtained based on the procedures discussed in section 4.1.3.

The optical power of the laser is characterized by fitting several power-current pairs to a second order polynomial function. Figure 4.11 shows the measured optical power of the QCL (using Thorlabs, S302C) at different input currents as well as the fitting curve.

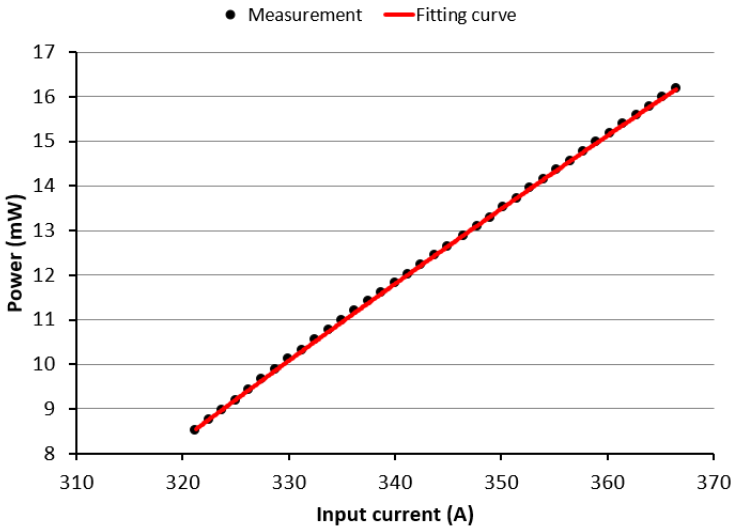

Figure 4.11: Measurement of QCL power vs injection current.

The fitting curve at figure above results the equation below:

$$P[mW] = -0.0002i[mA]^2 + 0.3037i[mA] - 68.76 \quad (4.24)$$

The injection current needed to cover the ammonia absorption feature including DC and AC components has the following form (in one sawtooth period):

$$i[\text{mA}] = 350 - 2000t + 20\sin(2\pi \times 10^4 t) \quad , \quad 0 \le t \le 0.01\ \text{s} \quad (4.25)$$

Using equations 4.24 and 4.25, the modulated optical power on the detector active area in absence of the sample can be measured and used in simulation.

With the current modulation in equation 4.25, the laser frequency characterization takes following form during the time period $0 \le t \le 0.01$ s:

$$v[cm^{-1}] = 967.14 + 37.2338t + 697.57t^2 + 0.136\sin(2\pi \times 10^4 t - 1.08\pi) \quad (4.26)$$

Figure 4.12 shows the measured laser power and frequency in one period of the slow scanning.

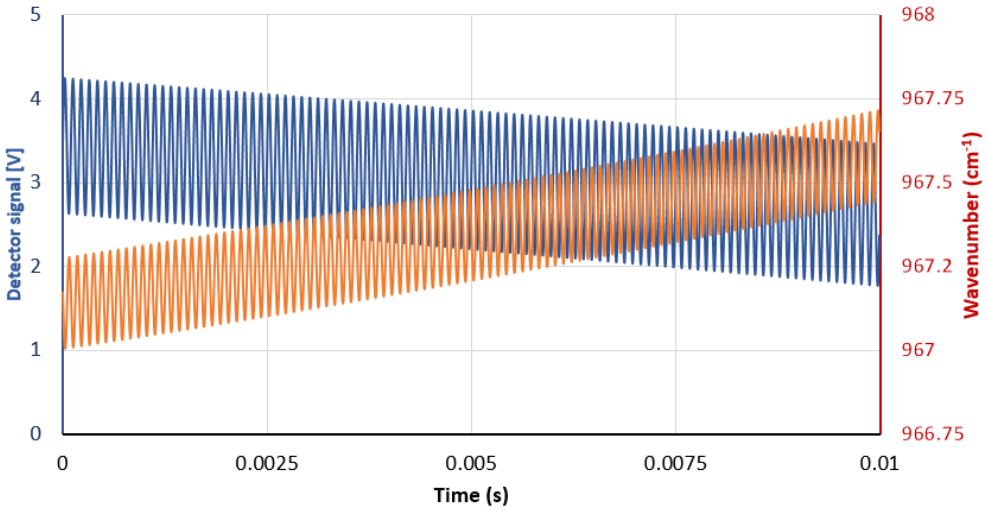

Figure 4.12: Measured QCL frequency and power response to the injection-current tuning.

Having the frequency and intensity modulation as well as the spectroscopic parameters of ammonia near 967.34 cm^{-1} (10.33 µm), the transmitted laser intensity through the multipass cell can be simulated (based on HITRAN and Beer-Lambert law). Figure 4.13 shows an example of the simulated detector output for ammonia concentration of 4 ppm.

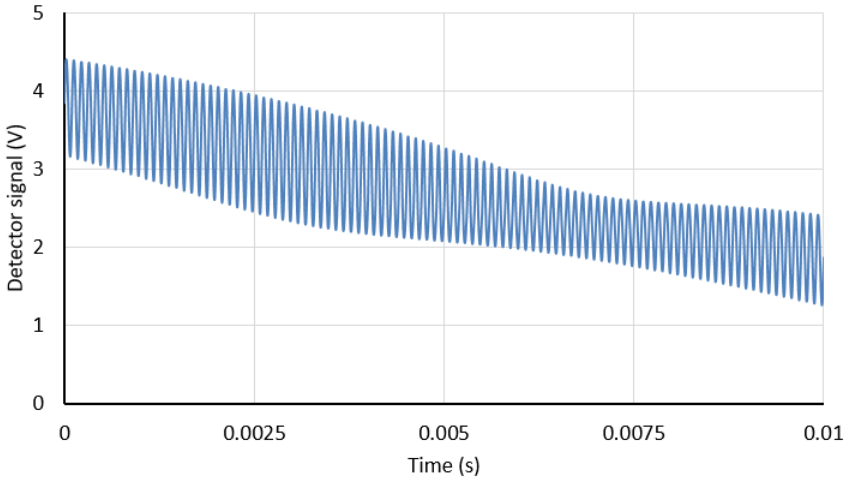

Figure 4.13: Simulated ammonia absorption for [NH_3]=4 ppm, P=0.84 atm, T=296 K.

The $2F/1F$ signal of the measured and simulated transmitted laser intensities were determined numerically by using identical digital lock-ins (bandwidth of 1 kHz) software. Figure 4.14 shows

the comparison between the simulated and measured $2F/1F$ signal with [NH_3]=150 ppb, P=0.84 atm, T=295 K, L=1988 cm.

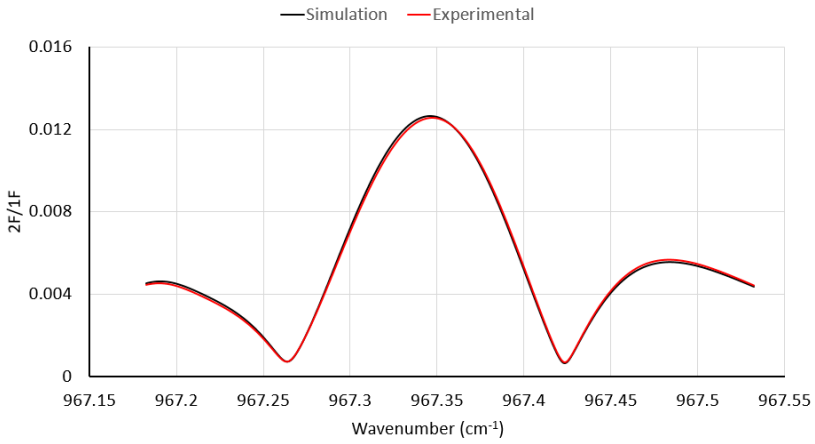

Figure 4.14: The comparison between measured and simulated $2F/1F$ signal ([NH_3]=150 ppb, P=0.84 atm, T=295 K, L=1988 cm).

In traditional WMS systems, the species concentration is retrieved by measuring the peak of $2F$ signal which is proportional to the sample absorption. An *in situ* signal calibration with known gas mixtures is needed for concentration measurement. However, this technique is practical only in systems at which the pressure and temperature of the measurement region is kept constant (e.g. with closed-path configuration). In addition to gas concentration, the WMS signals are dependent on environmental conditions: temperature and pressure. These parameters vary dramatically in the measurement region of open-path sensors and thus considering them in the concentrations retrieving is crucial.

In this study, the ammonia mole fraction is determined by a linear least-squares fit of the acquired $2F/1F$ signal to a stored simulated spectrum. In order to consider the pressure and temperature variations, one hundred $2F/1F$ spectra in various atmospheric conditions are simulated. The atmospheric pressure reported by Fort Collins Weather Station[82] during several days has shown

the ambient pressure in this area is typically in the range of $0.81\ \text{atm} \leq P \leq 0.85\ \text{atm}$. The ambient temperature at the sites during the daytime when the measurements are performed varies in the range of $0\ \text{C} < T < 20\ \text{C}$. For each pressure value of P_1=0.81 atm, P_2=0.82 atm, P_3=0.83 atm, P_4=0.84 atm, and P_5=0.85 atm, twenty spectra with the temperature values of 1 C to 20 C and [NH_3]=100 ppb have been simulated; i.e., there are five classes named as P_i (i=1,2,3,4,5) and each class has twenty spectra with different temperatures $T_{i,j}$ (j=1,2,…,20). The acquired $2F/1F$ spectrum is fitted to one of the pre-calculated spectra. The suitable simulated spectrum is chosen from the "library" of one hundred spectra, based on the measured ambient pressure and temperature. Once the pressure and temperature are measured, the LabVIEW code looks for a class with the closest pressure to the measured. Then, one of the twenty spectra in the specified class which has the closest temperature to the measured temperature is chosen for fitting. HITRAN-based simulation shows the deviation of temperature (± 1 K) and pressure (± 0.01 atm) leads to less than 0.1 ppb deviation in reported concentration. The concentration is determined using 40 ms of data, the analysis takes an additional 160 ms of computation time (digital lock-in analysis and spectrum fitting), giving a reported concentration value at a rate of 5 Hz.

A closed-path configuration at atmospheric pressure was used to examine the precision and accuracy of the sensor. Zero-air (Air- gas, 99.9996 % pure) and ammonia gas (Airgas, 10 ppm ammonia diluted in nitrogen) from two reference cylinders were mixed and passed through the optical cavity. An Allan variance study showed the sensitivity of ~4 ppb (at 1 second) which is adequate for this application. Figure 4.15 shows the results of comparison between expected and measured concentrations as well as the Allan variance graph.

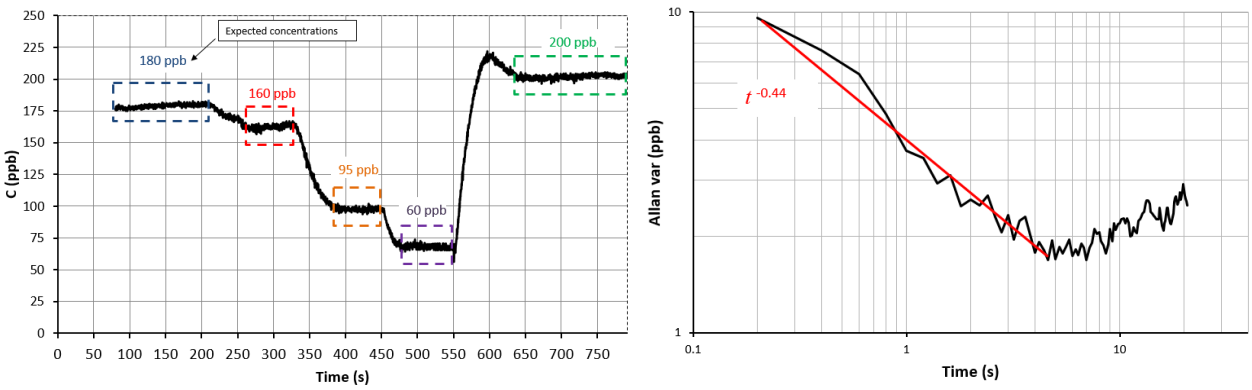

Figure 4.15: Left) Comparison between measured and expected ammonia concentrations with closed-path configuration. Right) Allan variance analysis shows the sensitivity of ~4 ppb (at 1 s).

Chapter 5: Field studies and mobile measurements

In this chapter, the sensor implementation on a truck (SUV) and UAS for mobile ground and aerial measurements are discussed. The obtained concentrations during several outdoor measurements (ground based and aerial) are shown. The ability to use the sensor (along with a methane sensor) for determination of ammonia deposition is discussed.

5.1- Mobile surface measurements

Preliminary outdoor tests were performed by ground-based measurements (using a SUV). During these measurements, the sensor was powered by the vehicle battery. A commercialized power inverter was used to convert the car battery output ~14 V (DC) to 110 V (AC). A DC power supply (12 V) was then connected to the inverter and used to power. Figure 5.1 shows a schematic of the instruments used to power the sensor on the vehicle. (In the future the sensor can be directly connected to the vehicle battery, but the current configuration is more convenient for initial research efforts.)

Figure 5.1: The sensor is powered using the car battery, a power inverter, and a DC power supply.

A custom aluminum anti-vibration mount was designed for mounting the sensor on the roof-rack cross-bars of the vehicle. As shown in Figure 5.2, the sensor is affixed to the mount using a pair of two-piece clamps which were tightly attached to the sensor bar. The electronic board was attached to the mount with 4 bolts.

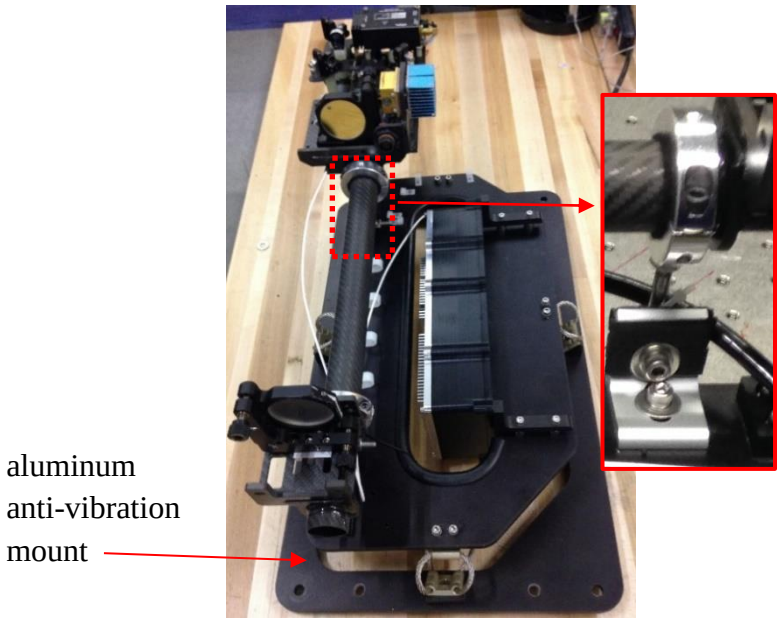

Figure 5.2: The custom mount holds the sensor and computer board. The inset shows (from a different angle) how the carbon-fiber rod is attached to the mount.

The custom mount was installed on two roof rack cross bars of the vehicle using four Square U-Bolts. Figure 5.3 shows the integration of the sensor to the vehicle (Ford, Expedition).

Figure 5.3: Installation of the ammonia sensor on an SUV.

The sensor performance was tested during different days in October and November 2017 for several hours each day. The optical alignment was not affected by the vibrations induced from the rugged road and vehicle movement. No overheating in the electro-optical devices (laser, detector, custom computer etc.) was observed. The vehicle was driven to different locations in the Fort Collins, CO area including agricultural farms, urban area, and feedlots. The measurements were performed during the vehicle movement while its geographical position (latitude and longitude) was saved by the GPS module. Figure 5.4 shows an example of the data acquired during ~1 hour of measurements. Figure 5.5 shows the concentration time series during the sampling. The increase of ammonia concentration near the major emission sources (vehicle engines and livestock) is clearly evident from the concentration data. Background ammonia levels (~5-20 ppb) were measured in the regions far away from the sources. While the SUV was moving and passing through the traffic congestion with several vehicles around, ammonia concentrations up to ~300

ppb (due to cars exhaust) were measured. The ammonia concentration increased to ~1500 ppb in the areas close to a dairy.

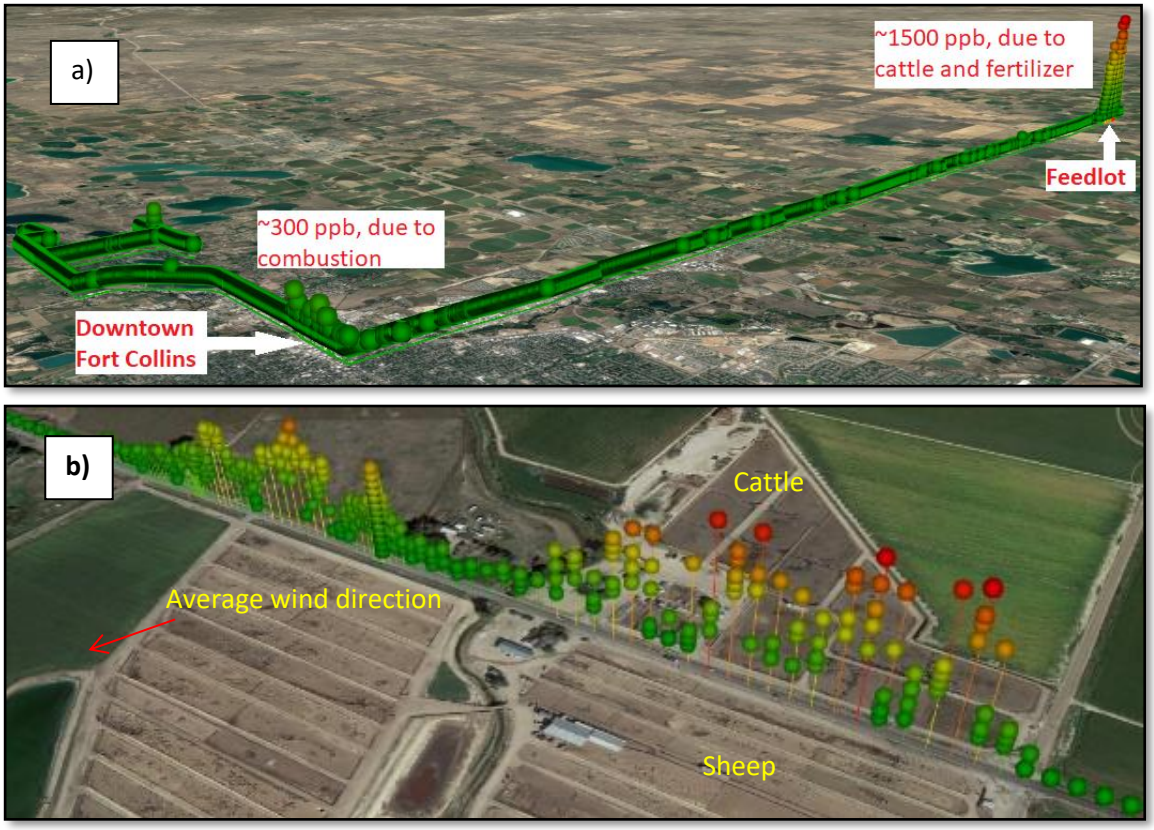

Figure 5.4: a) Concentration data imported into Google Earth. b) Zoomed-in images of the dairy. The road as well as the sheep and cattle population on both sides are seen. Multiple measurements at each point is because of repeated drives.

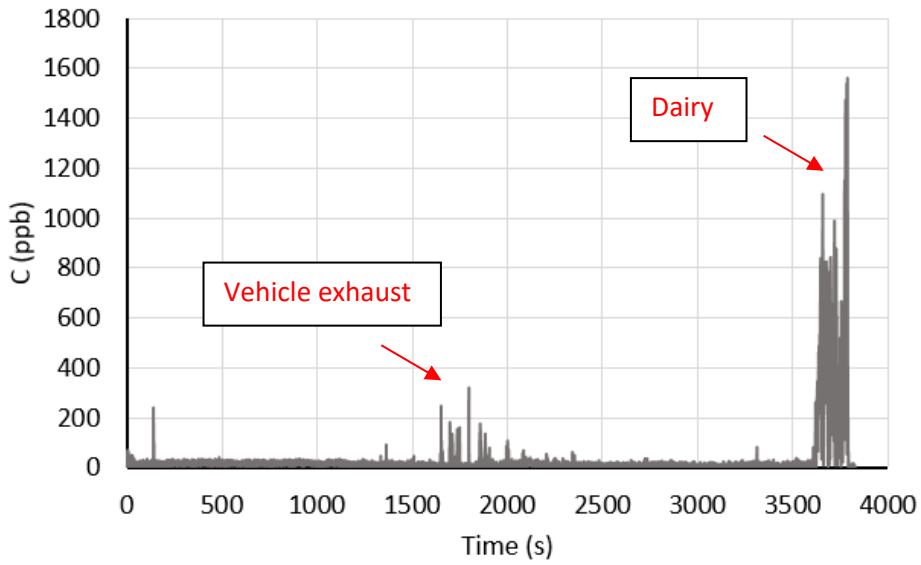

Figure 5.5: Ammonia concentration timeseries during ~1 hour measurement.

The ammonia sensor can be used to yield a measure of farm-scale NH_3 emissions. Furthermore, by integration of a methane analyzer, and using methane as a conservative tracer to normalize the ammonia dispersion, it is also possible to determine the rate of ammonia dry deposition. Such an approach will need several days of ammonia/methane measurements and applying complex atmospheric simulations which is beyond the scope of this thesis[83–85]. As a preliminary test demonstration of simultaneous ammonia-methane measurements, the ammonia sensor was integrated with a methane sensor to measure NH_3-CH_4 emissions in a feedlot. Methane was measured by an open-path CRDS based sensor developed by CSU mechanical engineer PhD candidate Laurie McHale under the supervision of Dr. Azer Yalin[62]. Figure 5.6 shows the integration of two open-path sensors on the vehicle. The methane sensor was mounted on the aluminum mount which could hold both sensor and its computer board. The ammonia sensor was installed on the roof rack bars using a stainless-steel mount. The connecting cables between the ammonia sensor and its computer board were long enough (2.1 m) that the computer was carried inside the vehicle.

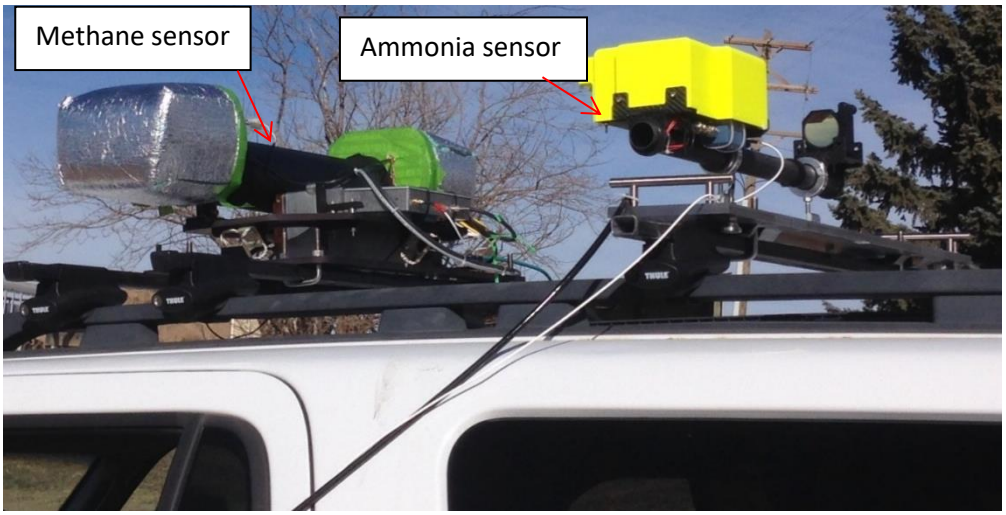

Figure 5.6: The integration of WMS and CRDS based sensors on the vehicle for simultaneous measurements of ammonia and methane respectively.

The measurements were conducted at a commercial cattle feedlot (La Luna) near Fort Collins, Colorado, (40.716238, -105.025921) with a cattle population of ~1000. A 3D sonic anemometer (Campbell Scientific, Inc., CSAT3) located at the feedlot was used for high frequency (20 Hz) wind vector measurements. Five stationary measurements, lasting ~20 minutes each, were performed at five different locations using the combination of ammonia and methane sensors. The first measurement spot was co-located with the sonic anemometer (in the dairy, close to the pens). The other measurement sites were found at different distances (generally downwind of the feedlot using the anemometer data. Figure 5.7 shows the aerial view of the feedlot and its surrounding as well as the locations of each of the measurements sites.

5.7: A map of the dairy facility and surrounding lands. The pins show the 5 individual measurements locations. Site 1 is co-located with the anemometer and is the closest site to the pens. The other spots were selected based on the wind direction measured by the anemometer.

The ammonia and methane concentrations were measured and saved at 5 Hz and 1 Hz, respectively. However, in order to synchronize two measurements, the results of ammonia measurement have been averaged to 1 Hz. Ammonia and methane concentrations measured in sites far from the dairy (2 and 3) were very close to background level ($[NH_3]$~5 ppb, $[CH_4]$~1.8 ppm), while sites 1, 4, and 5 (closer to the pens) showed higher levels. Figure 5.7 shows an example of raw concentration time series acquired from locations 2 and 4. Although the anemometer was used to select the best downwind spots, the extreme wind speed and direction variation caused dramatic concentration changes during the sampling even at sites 1, 4, and 5. As an example, figure 5.8a shows detection of a high concentration (ammonia and methane) plume at Site 4 that starts to appear at ~1:18 PM local time and lasts until ~1:25 PM. It is assumed that the true site emissions are approximately constant in time over our experiments and that the appearance and disappearance of the plume in figure 5.8a is due to wind variations that do (or do not) carry the

emission plume to the measurement location. Figure 5.8b shows lower concentrations of both ammonia and methane at site number 2 (~2 km far from the pens). Except ~2 minutes period from ~12:03 PM to ~12:05 PM, where the wind has carried a plume to the measurement site, the measured concentrations are at approximately background levels for both ammonia and methane.

The concentration decrease of ammonia at far distances from the dairy is faster than the (relative) methane concentration reduction because, during the plume transport, ammonia is affected by both dry deposition and dispersion, while methane is influenced only by dispersion. Thus, the $[NH_3]/[CH_4]$ at different spots downwind of the dairy can be used to estimate the rate of local ammonia deposition. Although such a study needs several hours and days of measurements and applying complex atmospheric models and simulations, the $[NH_3]/[CH_4]$ reduction at further distance (site 2) can be seen in figure 5.8. The average of ammonia and methane concentrations at site 4 during downwind period (1:18:00 to 1:25:00 PM) are 235 ppb and 3.95 ppm, respectively. After background subtraction (CH_4=1.8 ppm , NH_3=5 ppb) the ammonia/methane ratio is obtained as $\Delta[NH_3]/\Delta[CH_4]=0.11$. This ratio at site 2 decreases to $\Delta[NH_3]/\Delta[CH_4]=0.058$.

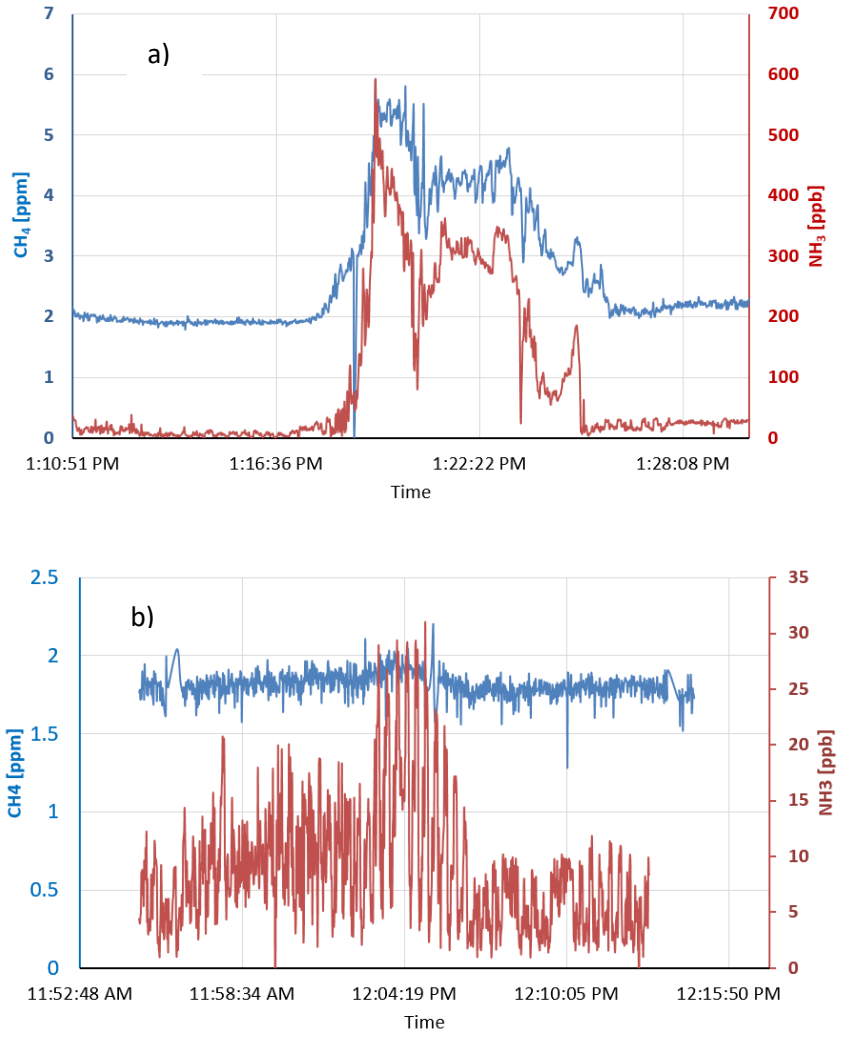

Figure 5.8: Simultaneous ammonia and methane measurements at sites 4 (a) and 2 (b).

5.2 – Aerial (UAS) Measurements

The UAS utilized for aerial NH_3-CH_4 measurements was a commercial 12 foot Senior Telemaster that has been redesigned and modified to accommodate the sensors. The physical assembly of the UAS and initial test flights were conducted by a team under the supervision of CSU emeritus professor, Dr. Fred Smith.

The overall weight of the UAS including the fuselage, batteries, two sensors, two customized computers and cables was 24.7 kg. Table 5.1 shows the weights masses of the airplane and the sensors.

Table 5.1: Masses of UAS and optical sensors

	UAS (Fuselage, Motor, Batteries)	Ammonia		Methane		Sensors battery
		Electro-optical	Computer	Electro-optical	Computer	
Weight	16.2 kg	2.1 kg	1.9 kg	2 kg	2.1 kg	0.4

The required input power of ~5000 W (~130 A at ~40 V during take-off and ~60 A at 40 V during cruise) needed to fly the UAS was provided by a combination of a 10Ah 6 cell LiPo and a 10Ah 4 cell LiPo batteries. With these batteries the airplane could fly and carry both ammonia and methane sensors for ~8 minutes. Two sensors were mounted under the UAS wings while their computer boards were placed inside the fuselage. Figure 5.9 shows mounting the ammonia sensor and its computer to the UAS. The methane sensor and it computer were mounted similarly, on the other side of the UAS. The ammonia and methane sensors consumed ~25 W and ~15 W of power, respectively. A Lithium ion battery (5000 mAh, ~14 V) could power both sensors about ~2 hours.

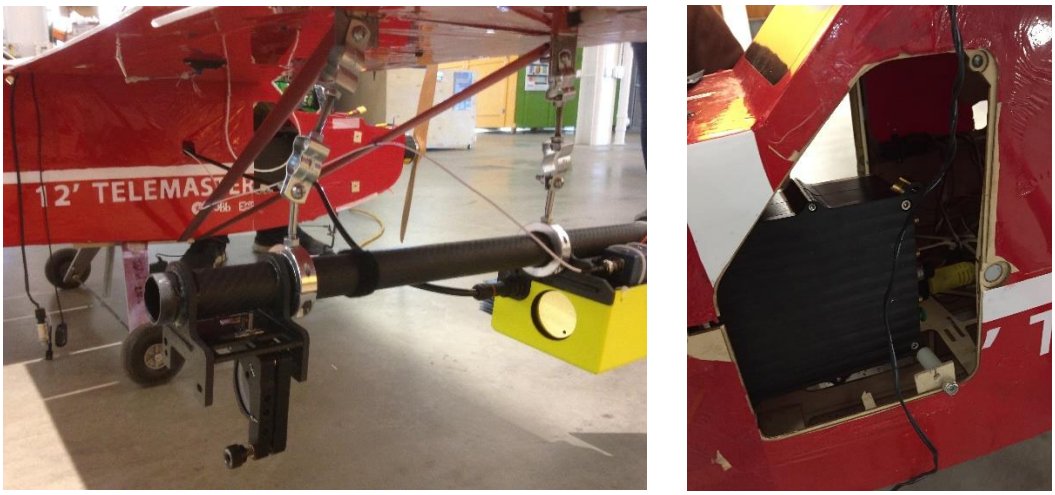

Figure 5.9) Mounting the ammonia sensor and its computer on the UAS. Left: The sensor was attached to the wing using four conduit hangers. Right: The electronic box was bolted in the fuselage

Two dummy loads with the same size, weight, and center of gravity of the ammonia and methane sensors were built for preliminary test flights. One of the major challenges was breaking the landing gear due to the extra weight during the landing. It was overcome by designing and building a custom landing gear. The drag due to the sensors was a large issue too. The sensors mounting location made a large difference in the amount of drag and specific mounting locations had to be determined to minimize the drag.

After several flights with dummy sensors, the real ammonia analyzer was flown along with the simulative methane sensor. Figure 5.10 shows ammonia sensor during the flight.

Figure 5.10: The real ammonia and dummy methane sensors on the UAS during a flight.

The flight occurred at a site which was ~1.5 km from a big feedlot. Figure 5.11 shows the ammonia concentration timeseries as well as the aerial view of the flight path, monitored and saved by the GPS, and the feedlot. In this test, we did not use a sonic anemometer for wind speed and direction measurement. A windsock was used to evaluate the wind direction. An estimation of local wind direction, shown by the windsock, during the flight is illustrated by the red arrow in figure 5.11(up). The higher concentrations (starting at 10:39:30) recorded in the northern region of the flight path is because of the ammonia plume transported from the feedlot located in the left side of the image.

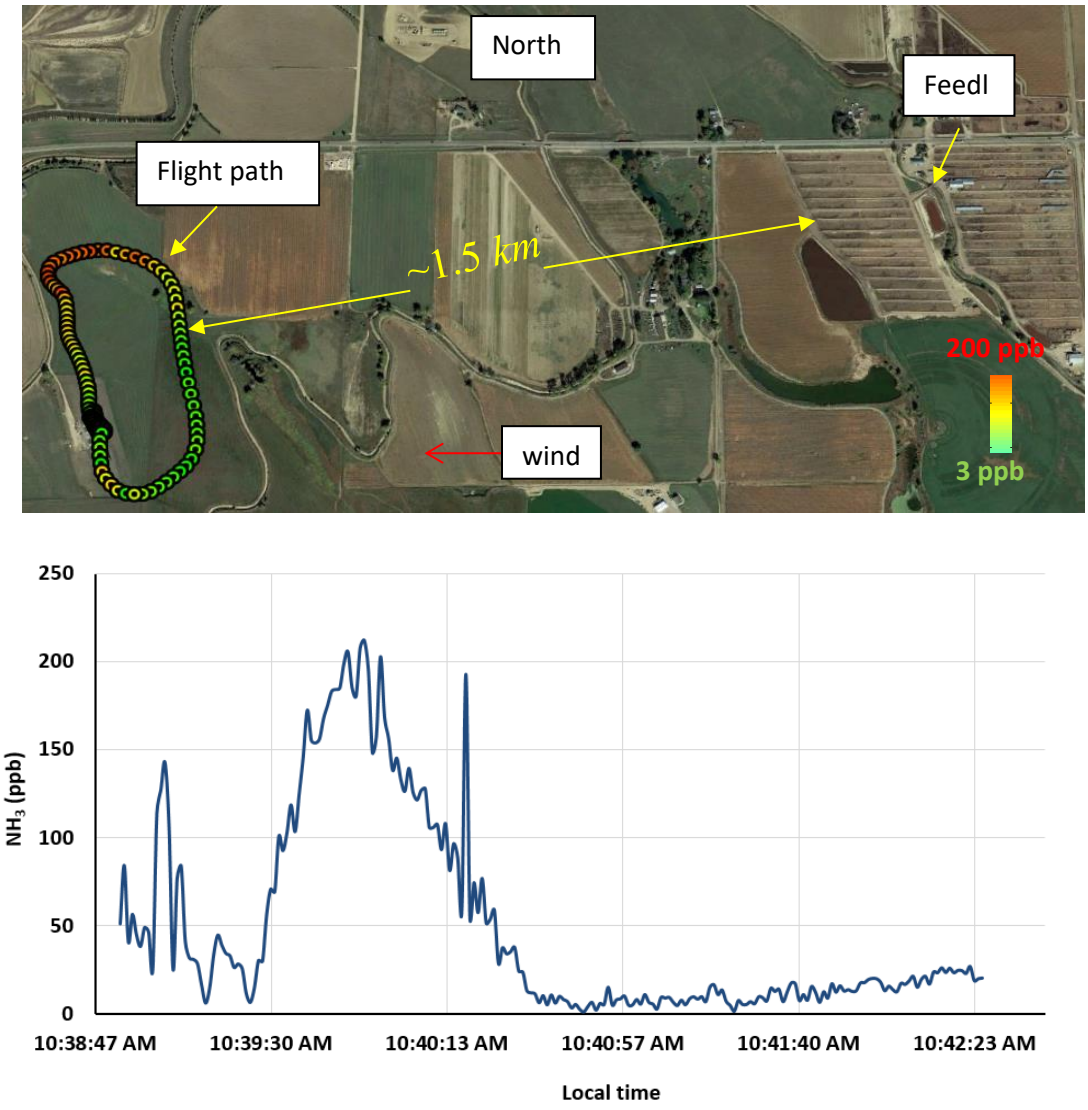

Figure 5.11: Up) The aerial view of the flight path and the feedlot. Down) The measured ammonia concentration time series.

A simultaneous aerial ammonia-methane measurement was conducted at the same site on April 15, 2018. Figure 5.12 shows the sensors during the flight and the NH_3-CH_4 concentration timeseries. As it can be seen, during the first 3 minutes of the flight the ambient concentrations of ammonia (~5 ppb) is measured. From the 4th minute the ammonia level increases up to ~20 ppb. The same pattern is shown by the methane sensor, however the average methane concentration during the flight is higher (~2.6 ppm) than the ambient (~1.8 ppm). Since the flight took place at

~1.5 km from a dairy, the measured ambient level of ammonia and elevated level of methane might be because of ammonia deposition during the plume transport.

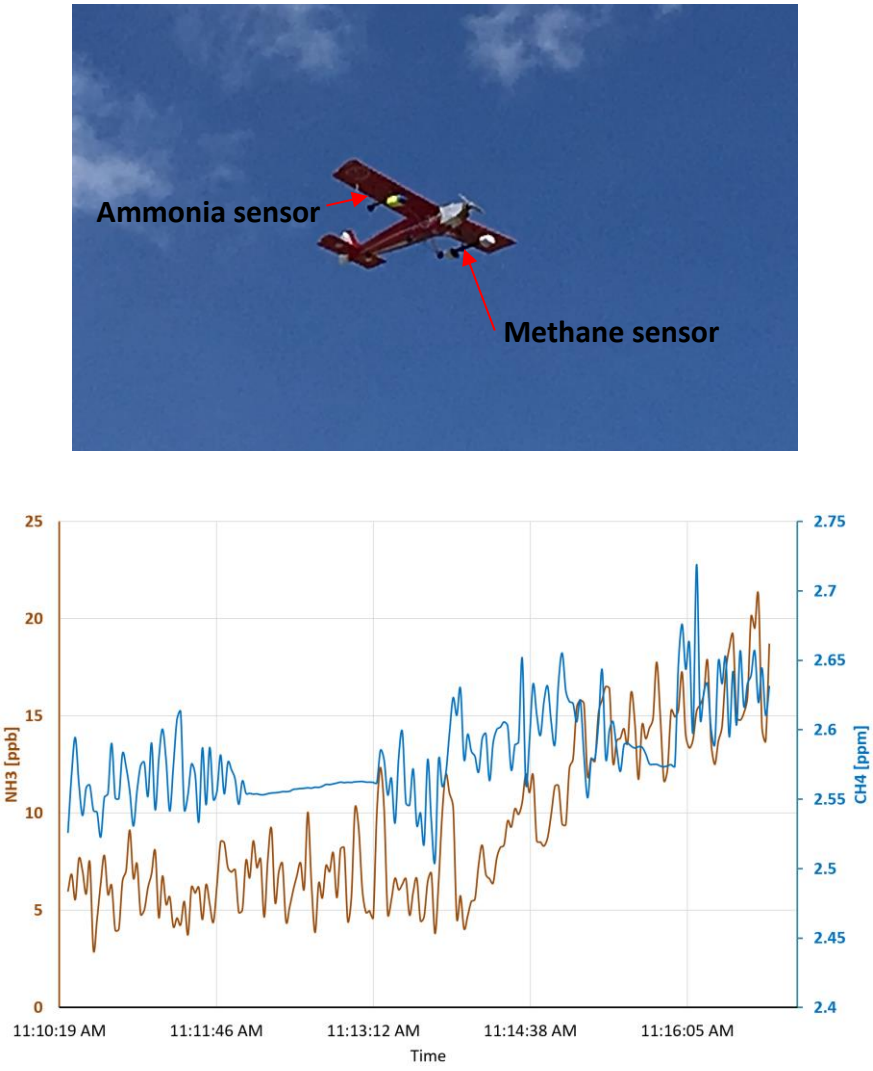

Figure 5.12: Top: Ammonia and methane sensors during the flight. Bottom: The measured ammonia-methane concentration time series.

This test flight showed the feasibility of simultaneous aerial NH_3-CH_4 measurements. In order to study the deposition rate of ammonia downwind of the CAFOs, more and longer flights with known meteorological conditions are needed.

Chapter 6: Summary and future works

6.1- Summary

The man-made pollution of the atmosphere has recently been one of the biggest concerns for life on the earth. Although most pollutant species emitted into the atmosphere are in low concentrations, their adverse effects on nature, ecosystem, and human health have been demonstrated. The low concentration of these pollutants makes them difficult to measure and monitor their emission from main sources, where traffic, agricultural operations, and industry are the most important types. Agricultural activities are the major source of ammonia emission into the atmosphere. Quantifying ammonia emission rate and its deposition nearby farms and feedlots is crucial for atmospheric chemistry studies.

Traditionally, chemical techniques are used for trace species (such as ammonia) detection. However, the analyzers based on these techniques are bulky, heavy, power hungry, and complicated and not suitable for field studies. Optical spectroscopic techniques can provide adequate sensitivity while the sensors are light-weight and compact (suitable for field studies). Also, optical based sensors can be designed with open-path configuration which is useful for detection of “sticky” molecules such as ammonia. This dissertation described the development of two open-path absorption based optical sensors for atmospheric ammonia detection. The light source of both sensors was a cw thermoelectric-cooled distributed feedback quantum cascade laser. The wavelength of the laser covers the strongest absorption feature of ammonia which occurs at 10.33 μm spectral region.

The first sensor was based on CRDS. To our knowledge, it was the first demonstration of an open-path CRDS based sensor in MIR spectral region. The mirrors with highest reflectivity (R=%99.95) reported in 9-11 μm region, were used to form the optical cavity. An effective path length of 1 km and ring-down time of ~3.3 μs were obtained with a cavity length of 50 cm. A polarizer and a quarter wave-plate in series were used as an optical isolator to block the reflected beam from the high reflectivity mirror in to the laser. An acoustic optical modulator was used to deviate the beam from the cavity while the optical power leakage out of the cavity was detected by a photodiode. A custom LabVIEW program was used for ring-down measurements as well as analyzing the data acquired from a DAQ card with high sampling rate (100 MHz). Ammonia concentrations were determined by fitting the measured ring-downs (at various wavelengths), with a synthetic Lorentzian spectrum which included multiple absorption lines of ammonia, water and carbon dioxide. Allan studies showed the sensitivity of ~1 ppb at one second which is sufficient for ammonia emission and deposition studies. The total electrical power consumption of the sensor was ~500 W power. More than 75 % of the required power was due to AOM and its driver as well as associated water cooling. The water cooling was needed since the AOM window (germanium) loses its optical transmission in high temperatures (>35° C). Also, the high-power radio frequency generated by the AOM driver for germanium vibration makes ~200 W heat which should be dissipated by water. For preliminary field studies, the sensor was developed on a portable wheeled cart ($50 \times 70 \times 90$ cm^3). The cart could be rolled or driven in the back of a pickup truck without loss of alignment. The sensor performance was tested at a feedlot located at northern Colorado during different days for several hours each day. The open-path configuration was also validated by comparison against a collocated commercial closed-path CRDS instrument and ammonia concentrations from the two instruments were in good agreement.

One of the objects of this study was development of a sensor for quantifying the vertical and horizontal profiles of ammonia concentration nearby agricultural farms. However, the currently available AOM which needs a bulky and power hungry water cooling system, made the CRDS based sensor undesirable for such an application where a more compact (~20 L, ~4 kg) and lower power (~25 W) sensor is needed.

Another ammonia sensor was developed for UAS based aerial measurements. The second sensor was based on another absorption based technique: WMS. This technique was chosen because of its simple electro-optical setup and the ability of noise rejection. The WMS sensor was integrated with a multipass cell to improve the sensor sensitivity and a custom miniaturized RIO-board based computer was built for data acquisition. The sensor (including the laser, optics, and detector) was designed with a compact configuration ($60 \times 20 \times 15$ cm^3, ~2 kg), where most of the physical structures was made from carbon-fiber to reduce the weight and increase the stability. The custom computer was in a sealed box ($30 \times 10 \times 5$ cm^3, ~2 kg) with aluminum fins as the heat sink. A custom LabVIEW program was used to design four digital lock-in amplifier in parallel (two for $1F$ signal and two for $2F$ signal) to acquire $2F/1F$ spectrum. The $2F/1F$ strategy was used to eliminate the need for sensor calibration since in this approach the acquired signal is independent of the detector gain as well as the variation in the laser intensity. The measured $2F/1F$ spectrum was compared to a stored simulated signal to infer the ammonia concentration. Multiple $2F/1F$ signals (with different ambient temperature and pressure values) were simulated to compensate the rapid variation of environmental conditions in the open-path measurement region of the sensor. The WMS signals were simulated based on the spectroscopic parameters from the HITRAN database, Beer-Lambert law, and characterizing the QCL response to the modulated injection current. The Allan study showed the sensitivity of ~4 ppb (at 1 second).

The sensor was used in a number of outdoor ground based and aerial measurements. The ground measurements were performed by the sensor integration on an SUV. The sensor performance was evaluated while the vehicle was moving around different sources of ammonia including traffic congestion (combustion) and feedlots (cattle). High concentrations of ammonia were measured near these sources (up to ~1500 ppb and ~300 ppb from feedlots and vehicles exhaust, respectively). The ammonia sensor was integrated with an open-path methane sensor for simultaneous NH_3-CH_4 ground measurements nearby a feedlot. A good correlation between ammonia and methane emission (as two main products of feedlots) was observed.

A UAS was used for aerial NH_3-CH_4 measurements. Each sensor was installed under each wing of the UAS. The initial aerial test was performed using only the ammonia sensor while a dummy load took the place of the methane sensor (to keep the UAS balanced). This flight took place in ~1.5 km distance from a big feedlot and ammonia concentrations up to ~250 ppb was measured. The next flights with both NH_3 and CH_4 sensors showed the feasibility of simultaneous aerial ammonia and methane measurements.

6.2- Future Works

Sensor improvements

The WMS ammonia sensor described in this work has demonstrated the ability to detect ammonia concentration emitted from livestock. Although the sensor has shown the capability of ammonia measurement near major sources (feedlots and vehicles), it is not fast and sensitive enough for other applications such as eddy covariance studies. The sensor capability can be improved by increasing the effective path length of the multipass cell. This can be conducted by using bigger spherical mirrors (e.g. 3” mirrors can make up to ~50 m path length). Alternatively, cylindrical

mirrors can be used to increase the mirror area on which the beam can hit without spot interferences.

The sensor sensitivity can also be improved by using a faster DAQ system. The DAQ system used in this study has provided the maximum sampling rate of 200 kHz. Such a low sampling rate restricts the modulation frequency (Nyquist theory) to ~20 kHz (with 200 kHz sampling rate and 20 kHz modulation frequency, only 10 data points are acquired in each frequency sweep). Having a higher modulation frequency reduces the flicked noise in the system which leads to a better sensor performance.

Ammonia dry deposition calculation

Quantifying the fraction of volatized ammonia from concentrated animal feeding operations (CAFOs) that is returned locally to the surface is a key factor to study how fugitive nitrogen from livestock impacts the environment. To determine the rate of local ammonia deposition, one approach would be simultaneous ammonia-methane measurements and using methane emitted from the feedlot as a conservative tracer. Methane is a nonreactive molecule and opposed to ammonia which is lost by deposition and dispersion, its change in concentration with downwind distance will be influenced by dispersion alone. Thus, by deploying the ammonia and methane sensors on a UAS and measuring the decrease in the NH_3/CH_4 ratio downwind (vertically and horizontally with the sUAS) of the CAFOs, the rate of ammonia deposition over sufficient spatial and temporal scales can be inferred. Although in this study few preliminary experiments were performed by ammonia and methane sensors, they did not provide enough data for a comprehensive study on deposition calculation. The sudden variation of atmospheric conditions at the measurement sites is one of the factors that needs to be considered during the test. High number of field measurements are needed to increase the statistical power of the analysis.

References

1. Peter Warneck. Chemistry of the Natural Atmosphere. (1999).

2. Aneja, V. Measurement and analysis of atmospheric ammonia emissions from anaerobic lagoons. *Atmos. Environ.* **35,** 1949–1958 (2001).

3. Timmer, B., Olthuis, W. & Berg, A. van den. Ammonia sensors and their applications—a review. *Sensors Actuators B Chem.* **107,** 666–677 (2005).

4. Baum, K. A. & Ham, J. M. Adaptation of a speciation sampling cartridge for measuring ammonia flux from cattle feedlots using relaxed eddy accumulation. *Atmos. Environ.* **43,** 1753–1759 (2009).

5. Aneja, V. P. *et al.* Ammonia Assessment from Agriculture : U . S . Status and Needs. *J. Environ. Qual* **37,** 515–520 (2008).

6. Aneja, V. P., Bunton, B., Walker, J. T. & Malik, B. P. Measurement and analysis of atmospheric ammonia emissions from anaerobic lagoons. *Atmos. Environ.* **35,** 1949–1958 (2001).

7. Fangmeierfl, A., Ludger, A. H., Eerden, V. Der & Hans-jijrgen, J. Effects of Atmospheric Ammonia on Vegetation, A Review. *Environ. Pollut.* **86,** (1994).

8. M.A. Sutton, D. Fowler, J. K. B. and C. M. Vegetation Atmosphere Exchange Of Ammonia: Canopy Cycling And The Impacts Of Elevated Nitrogen Inputs. *Water, Air Soil Pollut. 85* 2057–2063 (1995).

9. Pleim, J. E., Bash, J. O., Walker, J. T. & Cooter, E. J. Development and evaluation of an ammonia bidirectional fl ux parameterization for air quality models. *J. Geophys. Res. Atmos.* **118,** 3794–3806 (2013).

10. Clarisse, L., Clerbaux, C., Dentener, F., Hurtmans, D. & Coheur, P. Global ammonia distribution derived from infrared satellite observations. *Nat. Geosci.* **2,** 479–483 (2009).

11. Sutton, M. A., asman. w. a, S. J. K. dry depositioon of reduced nitrogen. *Tellus* **46b,** 255–273 (1994).

12. https://archive.is/Ptnc.

13. Sutton, M. A. dry depositioon of reduced nitrogen. *Tellus* **46b,** 255–273 (1994).

14. Barna, M. G. Rocky Mountain Atmospheric Nitrogen and Sulfur Study Report. (2009).

15. Baron, J. S. Hindcasting nitrogen deposition to determine an ecological critical load. *Ecol. Appl.* **16,** 433–439 (2006).

16. John H. Seinfeld, S. N. P. *Atmospheric Chemistry and Physics: From Air Pollution to Climate Change*. (2006).

17. Gebhart, K. A. *et al.* Back-trajectory-based source apportionment of airborne sulfur and nitrogen concentrations at Rocky Mountain National Park , Colorado , USA. *Atmos. Environ.* **45,** 621–633 (2011).

18. Benson, D. R. & Markovich, A. Techniques A Chemical Ionization Mass Spectrometer for ambient measurements of Ammonia. *Atmos. Meas. Tech* **3,** 1075–1087 (2010).

19. Fehsenfeld, F. C. *et al.* Results from an informal intercomparison of ammonia measurement techniques. *J. Geophys. Res.* **107,** 1–15 (2002).

20. https://www.daylightsolutions.com/.

21. Harris, D and Bertolucci, M. Symmetry and spectroscopy; an introduction to vibrational and electronic spectroscopy. *Oxford Univ. Press* **62,** 301 (1978).

22. https://en.wikipedia.org/wiki/Ammonia.

23. David, C. W. IR Vibration-Rotation Spectra of the Ammonia Molecule. *Journal of Chemical Education* **73,** 46–50 (1996).

24. Sur, R. *et al.* Line intensities and temperature-dependent line broadening coefficients of Q-branch transitions in the v2band of ammonia near 10.4 μm. *J. Quant. Spectrosc. Radiat. Transf.* **175,** 90–99 (2016).

25. http://www.chemtube3d.com/vibrationsNH3.htm.

26. Rothman, L. S. *et al.* The HITRAN2012 molecular spectroscopic database. *J. Quant. Spectrosc. Radiat. Transf.* **130,** 4–50 (2013).

27. Soediono, B. *Diode Lasers and Photonic Integrated Circuits*. *Wiley* **53,** (1989).

28. Williams, B. S. Terahertz quantum-cascade lasers. *Nat. Photonics* **1,** 517–525 (2007).

29. Donati, S. Photodetectors: Devices, Circuits, and Applications. *Meas. Sci. Technol.* **12,** 653 (2001).

30. Galle, B. *et al.* Measurements of ammonia emissions from spreading of manure using gradient FTIR techniques. *Atmos. Environ. 34* **34,** 4907–4915 (2000).

31. Kogelnik, H. & Kompfner, R. Off-Axis Paths in Spherical Mirror Interferometers. **3,** 523–526 (1964).

32. Shadman, S., Rose, C. & Yalin, A. P. Open-path cavity ring-down spectroscopy sensor for atmospheric ammonia. *Appl. Phys. B Lasers Opt.* **122,** 1–9 (2016).

33. Mcmanus, J. B. *et al.* Quantum cascade lasers for open and closed path measurement of

atmospheric trace gases. in *Diode Lasers and Applications in Atmospheric Sensing* 22–33 (2000).

34. Gong, L. *et al.* Atmospheric ammonia measurements in Houston , TX using an external-cavity quantum cascade laser-based sensor. *Atmos. Chem. Phys* **11,** 9721–9733 (2011).

35. Leen, J. B. *et al.* Fast In Situ Airborne Measurement of Ammonia Using a Mid-Infrared O ff -Axis ICOS Spectrometer. *Environ. Sci. Technol.* **47,** 10446–10453 (2013).

36. Ellis, R. A. *et al.* Characterizing a Quantum Cascade Tunable Infrared Laser Differential Absorption Spectrometer (QC-TILDAS) for measurements of atmospheric ammonia. *Atmos. Meas. Tech.* **3,** 397–406 (2010).

37. Manne, J., Sukhorukov, O., Jäger, W. & Tulip, J. Pulsed quantum cascade laser-based cavity ring-down spectroscopy for ammonia detection in breath. *Appl. Opt.* **45,** 9230–9237 (2006).

38. Bianchi, F., Dommen, J., Mathot, S. & Baltensperger, U. On-line determination of ammonia at low pptv mixing ratios in the CLOUD chamber. *Atmos. Meas. Tech.* **5,** 1719–1725 (2012).

39. Wysocki, G. *et al.* Pulsed quantum-cascade laser-based sensor for trace-gas detection of carbonyl sulfide. *Appl. Opt.* **43,** 6040–6046 (2004).

40. Volten, H. *et al.* Two instruments based on differential optical absorption spectroscopy (DOAS) to measure accurate ammonia concentrations in the atmosphere. *Atmos. Meas. Tech.* **5,** 413–427 (2012).

41. Mount, G. H. *et al.* Measurement of atmospheric ammonia at a dairy using differential optical absorption spectroscopy in the mid-ultraviolet. *Atmos. Environ.* **36,** 1799–1810 (2002).

42. Miller, D. J., Sun, K., Tao, L., Khan, M. a. & Zondlo, M. a. Open-path, quantum cascade-laser-based sensor for high-resolution atmospheric ammonia measurements. *Atmos. Meas. Tech.* **7,** 81–93 (2014).

43. Gagliardi, G. & Loock, H. *Cavity-Enhanced Spectroscopy and Sensing*. (Academic Express, 2014).

44. Peeters, R., Berden, G., Apituley, A. & Meijer, G. Open-path trace gas detection of ammonia based on cavity-enhanced absorption spectroscopy. *Appl. Phys. B* **236,** 231–236 (2000).

45. He, Y. *et al.* Remote open-path cavity-ringdown spectroscopic sensing of trace gases in air , based on distributed passive sensors linked by km-long optical fibers. *Opt. Express* **22,** 6752–6761 (2014).

46. Verdeyen, J. T. Laser Electronics.pdf. (2005).

47. Kogelnik, H. & Li, T. Laser Beams and Resonators. *Proc. IEEE* **54,** 1312–1329 (1966).

48. Herbelin, J. M. & Mckay, J. A. Development of laser mirrors of very high reflectivity using the cavity-attenuated phase-shift method. *Appl. Opt.* **20,** 3341–3344 (1981).

49. Anderson, D. Z., Frisch, J. C. & Masser, C. S. Mirror reflectometer based on optical cavity decay time. *Appl. Opt.* **23,** (1984).

50. Keefe, A. O. & Deacon, D. A. G. Cavity ring-down optical spectrometer for absorption measurements using pulsed laser sources. *Rev. Sci. Instrum.* **59,** (1988).

51. D. Romanini, A.A. Kachanov, N. & Sadeghi, E. S. CW cavity ring down spectroscopy. *Chem. Phys. Lett.* **264,** (1997).

52. Miles, R. E. H. *et al.* Sources of Error and Uncertainty in the Use of Cavity Ring Down Spectroscopy to Measure Aerosol Optical Properties. *Aerosol Sci. Technol. ISSN* **45,** 1360–1375 (2011).

53. Lehmann, K. K. & Romanini, D. The superposition principle and cavity ring-down spectroscopy. *J. Chem. Phys.* **105,** 10263–10277 (1996).

54. Zalicki, P., Zalicki, P., Zare, R. N. & Zare, R. N. Cavity ring-down spectroscopy for quantitative absorption measurements. *J. Chem. Phys.* **102,** 2708 (1995).

55. He, Y. & Orr, B. J. Rapidly swept, continuous-wave cavity ringdown spectroscopy with optical heterodyne detection: Single- and multi-wavelength sensing of gases. *Appl. Phys. B Lasers Opt.* **75,** 267–280 (2002).

56. Troccoli, M. *et al.* Long-Wave IR Quantum Cascade Lasers for emission in the λ = 8-12μm spectral region. *Opt. Mater. Express* **3,** 1546 (2013).

57. Dudek, J. B. *et al.* Trace moisture detection using continuous-wave cavity ring-down spectroscopy. *Anal. Chem.* **75,** 4599–4605 (2003).

58. Hagen, C. L. *et al.* Cavity ring-down spectroscopy sensor for detection of hydrogen chloride. 345–357 (2014). doi:10.5194/amt-7-345-2014

59. Paldus, B. A. *et al.* Cavity ringdown spectroscopy using mid-infrared quantum-cascade lasers. *Opt. Lett.* **25,** 666–8 (2000).

60. Centeno, R., Mandon, J., Cristescu, S. M. & Harren, F. J. M. Three mirror off axis integrated cavity output spectroscopy for the detection of ethylene using a quantum cascade laser. *Sensors Actuators, B Chem.* **203,** 311–319 (2014).

61. Schmidt, F. M. *et al.* Ammonia in breath and emitted from skin. *J. Breath Res.* **7,** 017109 (2013).

62. McHale, L. E., Hecobian, A. & Yalin, A. P. Open-path cavity ring-down spectroscopy for

trace gas measurements in ambient air. *Opt. Express* **24,** 5523 (2016).

63. Pettersson, A., Lovejoy, E. R., Brock, C. A., Brown, S. S. & Ravishankara, A. R. Measurement of aerosol optical extinction at 532 nm with pulsed cavity ring down spectroscopy. *J. Aerosol Sci.* **35,** 995–1011 (2004).

64. Peter Kopke, Michael Hess, Ingrid Schult, E. P. S. *Global Aerosol Data Set*. (1997).

65. Werle, P., M??cke, R. & Slemr, F. The limits of signal averaging in atmospheric trace-gas monitoring by tunable diode-laser absorption spectroscopy (TDLAS). *Appl. Phys. B Photophysics Laser Chem.* **57,** 131–139 (1993).

66. Huang, H. & Lehmann, K. K. K. Long-term stability in continuous wave cavity ringdown spectroscopy experiments. *Appl. Opt.* **49,** 1378–87 (2010).

67. Khan, A. *et al.* Low Power Greenhouse Gas Sensors for Unmanned Aerial Vehicles. *Remote Sens.* **4,** 1355–1368 (2012).

68. Sun, K. *et al.* Open-path eddy covariance measurements of ammonia fluxes from a beef cattle feedlot. *Agric. For. Meteorol.* **213,** 193–202 (2015).

69. DavidG. CAMERION, D. J. M. A Generalized Approach to Derivative Spectroscopy. *Appl. Spectrosc.* **41,** (1987).

70. Kluczynski, P., Gustafsson, J., Lindberg, Å. M. & Axner, O. Wavelength modulation absorption spectrometry - An extensive scrutiny of the generation of signals. *Spectrochim. Acta - Part B At. Spectrosc.* **56,** 1277–1354 (2001).

71. Moeskops, B. W. M., Cristescu, S. M. & Harren, F. J. M. Sub-part-per-billion monitoring of nitric oxide by use of wavelength modulation spectroscopy in combination with a thermoelectrically cooled , continuous-wave quantum cascade laser. *Opt. Lett.* **31,** 823–825 (2006).

72. Rieker, G. B., Jeffries, J. B. & Hanson, R. K. Calibration-free wavelength-modulation spectroscopy for measurements of gas temperature and concentration in harsh environments. *Appl. Opt.* **48,** (2009).

73. Scofield, J. H. & Diagram, B. A Frequency-Domain Description of a Lock-in Amplifier 2 . Purpose of a Lock-in amplifier 4 . Time-Domain Description. *Am. J. Phys.* **62,** 129–132 (1994).

74. Li, H., Rieker, G. B., Liu, X., Jeffries, J. B. & Hanson, R. K. large modulation depth for diode laser absorption measurements in high-pressure gases. (2006).

75. Tao, L., Sun, K., Miller, D. J., Khan, M. A. & Zondlo, M. A. Compact and portable open-path sensor for simultaneous measurements of atmospheric N2O and CO using a quantum cascade laser. *Appl. Phys. B Lasers Opt.* **110,** 213–222 (2013).

76. Tao, L., Sun, K., Miller, D. J., Khan, M. A. & Zondlo, M. a. Current and frequency modulation characteristics for continuous-wave quantum cascade lasers at 9.06 μm. *Opt. Lett.* **37,** 1358–60 (2012).

77. Sun, K., Chao, X., Sur, R., Jeffries, J. B. & Hanson, R. K. Wavelength modulation diode laser absorption spectroscopy for high-pressure gas sensing. *Appl. Phys. B Lasers Opt.* 1–12 (2012). doi:10.1007/s00340-012-5286-0

78. Sun, K. *et al.* Analysis of calibration-free wavelength-scanned wavelength modulation spectroscopy for practical gas sensing using tunable diode lasers. *Meas. Sci. Technol.* **24,** 125203 (2013).

79. Altmann, J., Baumgart, R. & Weitkamp, C. Two-mirror multipass absorption cell. *Appl. Opt.* **20,** 995–999 (1981).

80. White, J. U. Long Optical Paths of Large Aperture. *J. Opt. Soc. Am.* **32,** 285–288 (1942).

81. Silver, J. A. Simple dense-pattern optical multipass cells. *Appl. Opt.* **44,** 6545–6556 (2005).

82. https://ccc.atmos.colostate.edu/.

83. Miller, D. J. *et al.* Ammonia and methane dairy emissions in the San Joaquin Valley of California from individual feedlot to regional-scale Plumes. 9718–9738 (2014). doi:10.1002/2015JD023241.Received

84. Shen, J. *et al.* Ammonia deposition in the neighbourhood of an intensive cattle feedlot in Victoria, Australia. *Sci. Rep.* **6,** 1–9 (2016).

85. Loubet B. et al. (2009) Ammonia Deposition Near Hot Spots: Processes, Models and Monitoring Methods. In: Sutton M.A., Reis S., Baker S.M. (eds) Atmospheric Ammonia. Springer, Dordrech t. 2009 (2009).